DIGITAL ACCESS TO SCHOLARSHIP AT HARVARD
DASH.HARVARD.EDU

HARVARD LIBRARY
Office for Scholarly Communication

Impacting Neuroscience With Chemistry: HDAC Neuroimaging Enabled by [18F]-Fluorination Methodology

Citation

Strebl, Martin Georg. 2017. Impacting Neuroscience With Chemistry: HDAC Neuroimaging Enabled by [18F]-Fluorination Methodology. Doctoral dissertation, Harvard University, Graduate School of Arts & Sciences.

Permanent link

http://nrs.harvard.edu/urn-3:HUL.InstRepos:42061502

Terms of Use

This article was downloaded from Harvard University's DASH repository, and is made available under the terms and conditions applicable to Other Posted Material, as set forth at http://nrs.harvard.edu/urn-3:HUL.InstRepos:dash.current.terms-of-use#LAA

Share Your Story

The Harvard community has made this article openly available.
Please share how this access benefits you. Submit a story .

Accessibility

Impacting Neuroscience With Chemistry: HDAC Neuroimaging Enabled by [^{18}F]-Fluorination Methodology

A thesis presented

by

Martin Georg Strebl

to

The Department of Chemistry and Chemical Biology

in partial fulfillment of the requirements

for the degree of

Doctor of Philosophy

in the subject of

Chemistry and Chemical Biology

Harvard University

Cambridge, Massachusetts

June 2017

©2017 - Martin Georg Strebl

All rights reserved.

Thesis advisor

Jacob Hooker and Tobias Ritter

Author

Martin Georg Strebl

Impacting Neuroscience With Chemistry: HDAC Neuroimaging Enabled by [^{18}F]-Fluorination Methodology

Abstract

In this dissertation, innovative radiochemical methodology was leveraged to systematically advance radiotracer development. A novel organometallic radiofluorination was established, as well as two fluorinated radiotracers, [^{18}F]MGS3 and [^{18}F]Bavarostat, for imaging histone deacetylases (HDACs) in the living brain using Positron Emission Tomography (PET).

First, to overcome the practical hurdles of [^{18}F]radiofluorination, a ruthenium-mediated deoxyfluorination was developed. This innovative radiochemical transformation benefits from readily available phenols as starting materials, tolerance of moisture and ambient atmosphere, large substrate scope, and translatability to generate doses appropriate for PET imaging.

The successful development of [^{18}F]MGS3, a class I and IIb selective HDAC imaging agent, illustrated limitations of traditional radiolabeling methods. The ability of ruthenium-mediated radiofluorination to resolve these existing challenges in radiosynthesis was demonstrated with a cGMP compliant, fully automated synthetic process for human radiopharmaceutical production of [^{18}F]MGS3. The discussion concludes

with an outlook on a state-of-the-art target validation platform design for HDAC inhibitors.

To validate the prospective value of target-oriented radiolabeling methodology, the de novo development of an HDAC6 PET tracer was accomplished. [^{18}F]Bavarostat was identified as a tracer candidate from a pool of HDAC6-selective small molecules based on computational predictions and validated by biochemical assays. Ruthenium-mediated radiofluorination enabled the study of [^{18}F]Bavarostat with PET imaging in rodents and non-human primates, highlighting its translational potential for human HDAC6 neuroimaging. The timeframe of de novo development of Bavarostat in comparison to the adaptation of [^{18}F]MGS3 demonstrates the efficiency of molecule-oriented method development in radiochemistry.

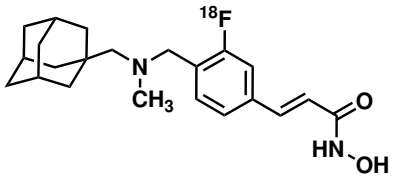

[^{18}F]MGS3

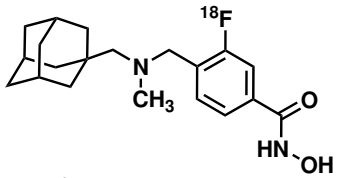

[^{18}F]Bavarostat

Contents

To Philipp and Martha, for being patient.

Citations to previously published work

Parts of this dissertation cover research reported in the following articles:

1. M. G. Strebl, C. Wang, F. A. Schroeder, M. S. Placzek, H.-Y. Wey, G. Van de Bittner, R. Neelamegam and J. Hooker, "Development of a Fluorinated Class-I HDAC Radiotracer Reveals Key Chemical Determinants of Brain Penetrance" *ACS Chem. Neurosci.*, **7**, 528-33, 2016.

2. M. H. Beyzavi[†], D. Mandal[†], M. G. Strebl[†], C. N. Neumann, E. M. D'Amato, J. Chen, J. M. Hooker and T. Ritter, "^{18}F-Deoxyfluorination of Phenols via Ru π-Complexes" *Under review,* 2017.

   [†] contributed equally

3. M. G. Strebl, T. Ritter, J. M. Hooker "HDAC6 brain mapping with [^{18}F]Bavarostat enabled by a Ru-mediated deoxyfluorination" *Manuscript in preparation.*

Acknowledgments

So schee kons Lebn sei,
Aa wenn ma's zwischendrin manchmoi vergisst,
So schee kons Lebn sei,
Kimmt immer drauf oo,
Mit welcham Maßstab dassma misst

— "So schee kons Lebn sei" by Martina Schwarzmann (2014)

First and foremost, none of this work would have been possible without my two advisors, Jacob and Tobias. Thank you Jacob for guiding me through the windy roads of research. You have gone above and beyond as an advisor and not only advanced my scientific rigor, but also my character, professionalism and enthusiasm for everything between small molecules and patients. Thanks for listening, your feedback and periodic reality checks. Thank you Tobias, for opening the doors for me here at Harvard, turning me into a real chemist and your tough love that has undoubtedly prepared me well for the ventures that await in the real world. Thank you also for your unwavering support through highs and lows of graduate school and letting me venture out to non-chemical things like tail veins and six-port valves. Thanks to Emily and David for supporting me as my committee throughout this journey. I would also like to thank all past and present members of the Hooker and Ritter labs for their patience, support and friendship. Anthony, Nicky, Heejun, Erica, Andrew, Michela, Sergio, Filippo, Jonas, Claudia, Tonya, Genevieve, Misha, Mike, Nicole, Matthias, Al, Monica, Changning, Ramesh, Baileigh, Christine, Hong, Jochen, Tom, Judit, Jane, Daniela, Kristen, Shirley, Reagan and many more... Thank you all for being wonderful!

Bong, palangga ko gid ikaw! Salamat gid kay ikaw ang pinakamaintindi, pinakapasensyoso kag mapinalangga-on nga bana. Gapasalamat gid ako kay ara ka pirme sa adlaw-adlaw, maski gapabudlay ako sa imo - nga daw pirme lang gid! Ikaw ang

pinakamaayo nga natabo sa kabuhi ko kag kung wala pa kita nakasal agda-on ta ikaw na pakaslan ako subong. Salamat gid kay ikaw ang rasun nga matawhay ang huna-huna kag pagkatawo ko, salamat sa pag-atipan kag pagpakaon kag pagpalipay sa akon. Indi mo ako mapalayo sa imo maski san-o. *Ikaw ang tanging Dreamboy ko.*

Mama, du bist immer für mi do und mir hamma ganz sche vui mitnander unternommen, eigentlich mehra wia vorher wo I no dahoam war. I konns goor ned song wie lieb dass I di hab und wie dankbar dass I dafür bin dass I a solche Stütze hob. Babba, danke dass du aa immer für mi do bist. Do brauchts ned so vui Schmaaz, aber I woas dass du nie weit weg bist. Wenn ebba so schee für mi Gitarre spielt, do woas I dass se nie wos feid. Dafür ein Vergelt's Gott! D'Oma mecht I aa loben, weil ohne sie hätt I nie glern't wie ma a sechane guade Antn kocht. D'Karl Resi mecht I bsunders hervorhebn, weil ohne de waar aus mir nie a Chemiker worden. Wenn's auf ders Welt oa guade Chemielehrerin gibt, nochad is des bestimmt d'Resi. Danke!

저의 절친인 지훈이에게 특별한 감사를 드리고 싶습니다. 제 결혼식에 참석하러 이틀이라는 짧은 시간동안 미국까지 날라온 대단한 친구에요! 너의 우정은 나한테 너무너무 소중하고 캠브리지에서 독일팀과 한국팀이 사이가 좋았던게 난 아직도 신기하지만 진짜 다행이고 행운인거 같다. 감사합니다, oide wuaschdhaut!

Thank you also to great friends and amazing colleagues that have made my life so much better over the last five years. You know who you are.

Martin Georg Strebl

May 29, 2017

Cambridge, Massachusetts

Acknowledgements of Financial Support

This dissertation wouldn't have been possible with the generous support through the Jacques-Emile Dubois Dissertation Fellowship Fund. I would like to personally thank Dr. Dubois for her continued support over the years that has given me the scientific freedom that made this work possible and hope that many generations of graduate students will enjoy her gift to science.

I would like to thank the Phelps foundation and the NIH for their support, specifically the NIH Blueprint for Neuroscience Research (T90DA022759/R90DA023427) that enabled the Advanced Multimodal Neuroimaging Training Program. This thesis was also supported by R01DA030321 and R01EB013042, as well as NIH shared instrumentation grants S10RR029495, S10RR026666, S10RR023452, 1S10RR017208-01A1, 1S10RR015728-01, S10RR017208, S10RR022976, S10RR019933 and S10RR023401. Additional funding through NIH NIGMS (GM088237) is gratefully acknowledged.

List of Abbreviations

AcOH	acetic acid
Ad	adamantyl
β-CFT	2-β-Carbomethoxy-3-β-(4-fluorophenyl)tropane
CB	cerebellum
CETSA	cellular thermal shift assay
cGMP	current good manufacturing practice
CNS	central nervous system
cod	cyclooctadiene
cp	cyclopentadienyl
CoREST	corepressor to REST (RE1 silencing transcription factor)
CT	computed tomography
CTX	cortex
Cy	cyclohexyl
DCM	dichloromethane
DLPFC	dorsolateral prefrontal cortex
DMSO	dimethyl sulfoxide
DNA	desoxyribonucleic acid

ECL	enhance chemoluminescence
ee	enantiomeric excess
EE	elution efficiency
EOB	end of bombardment
EtOH	ethanol
FAHA	6-(fluoroacetamido)-1-hexanoicanilide
FDA	Food and Drug Administration
FDG	fluorodeoxyglucose
FEFMZ	fluoroethyl flumazenil
FMZ	flumazenil
FWHM	full width at half maximum
GC	gas chromatography
HAT	histone acetyl transferase
HDAC	histone deacetylase
HDACi	histone deacetylase inhibitor
HEPES	4-(2-hydroxyethyl)-1-piperazineethanesulfonic acid
HILIC	hydrophilic interaction chromatography

HPLC	high performance liquid chromatography
HPOB	N-hydroxy-4-(2-[(2-hydroxyethyl)(phenyl)amino]-2-oxoethyl)benzamide
HRMS	high resolution mass spectrometry
HRP	horse radish peroxidase
HSP	heat shock protein
ICP	inductively coupled plasma
^{i}Pr	isopropyl
iPSC	induced pluripotent stem cell
LSD	lysine specific demethylase
MeCN	acetonitrile
MD	medial dorsal nucleus of the thalamus
MeOH	methanol
Me	methyl
MLEM	maximum likelyhood estimation method
MPO	multi parameter optimization
MPRAGE	magnetization-prepared rapid gradient-echo
MRI	magnetic resonance imaging

mRNA	messenger ribonucleic acid
MS	mass spectrometry
NAD	nicotinamide adenine dinucleotide
NHP	non-human primate
NHS	N-hydroxy succinimide
NIH	National Institute of Health
NMP	N-methyl pyrrolidone
NMR	nuclear magnetic resonance
NuRD	nucleosome remodeling deacetylase
OTs	toluenesuolfonate
PBS	phosphate buffered saline
PEG	polyethylene glycol
PET	positron emission tomography
PFP	pentafluorophenyl
ppm	parts per million
PTFE	polytetrafluoroethylene
QC	quality control

QMA	quarternary methyl ammonium
RCC	radiochemical conversion
R_f	retention factor
ROI	region of interest
SDS	sodium dodecyl sulfate
Sin	switch independent
SMA	supplementary motor area
S_NAr	nucleophilic aromatic substitution
SPE	solid phase extraction
SPECT	single photon emission computed tomography
SUV	standard uptake value
SUVR	standard uptake value ratio
TAC	time-activity curve
TBS	tris-buffered saline
TBS-T	tris-buffered saline with Tween20
tBu	tert-butyl
TFA	trifluoroacetic acid

TFAA	trifluoroacetic anhydride
TFAHA	6-(tri-fluoroacetamido)-1-hexanoicanilide
TLC	thin layer chromatography
THF	tetrahydrofuran
TMT	tandem mass tag
TOI	time of injection
TPSA	total polar surface area
UV	ultraviolet
VOI	volume of interest
VPN	ventral posterolateral nucleus of the thalamus
$\mathbf{V}_T$	volume of distribution (tissue)

Chapter 1

Introduction

1.1 From methods to molecules: Translational challenges in ^{18}F-PET tracer development

Positron emission tomography (PET) is a molecular imaging technique that uses positron emitting isotopes as contrast agents to enable the quantitative study of biochemical processes in vivo [1]. Compared to other imaging techniques like MRI or CT, it neither stands out in terms of spatial or temporal resolution. The true strength of the technique lies in its exquisite sensitivity and the ability to generate quantitative data about protein density or occupancy or the metabolic state of tissue. Particularly in combination with anatomical imaging (e.g. CT, MRI techniques like MPRAGE) powerful conclusions about the (bio)chemical state and/or function of the brain or other organs are possible. While a multitude of positron emitting isotopes has been used in PET applications, in a clinical context ^{18}F is the single most relevant nucleus.

Due to the clinical relevance of fluorodeoxyglucose(FDG)-PET, the infrastructure for ^{18}F production throughout the US is exceptionally well developed, with no location within the continental US being further than 2 h away from an ^{18}F production site [2]. The success of FDG in research and clinic results from several factors. The tracer is a fluorinated analogue of glucose and its uptake represents the relative rates of glucose metabolism in the respective tissue. The rate of glycolysis is a key variable in a multitude of pathological processes, including but not limited to the following examples: 1) the Warburg effect [3] can be exploited to detect cancerous tissues based on glucose consumption, and rate the malignancy of the tumor [4], 2) Glucose consumption in active brain tissue is higher than at rest, which can be used to detect areas of the brain that respond to specific experimental paradigms [5], 3) Inflammation causes increased glucose metabolism and FDG-PET can be used to localize inflamed tissue and judge the severity [6]. Another reason for the success of FDG-PET is the simplicity of analysis of the data. A standardized uptake value (SUV) is readily calculated from raw data using only the weight of the patient and the amount of injected activity, making interpretation of images relatively straightforward for experienced radiologists [7]. Furthermore, the chemistry to produce [^{18}F]FDG is exceptionally robust and simple, which ensures a constant supply of the tracer [8]. With a half-life of 109 min it is possible to ship doses of FDG from the production sites to remote imaging centers. Though they are not routinely used in the clinic yet, the FDA approved several PET-tracers within the last years including the plaque-detecting ^{18}F-tracers like Florbetapir and Flutemetamol [9].

Besides ^{18}F, ^{11}C is another isotope widely used to label organic small molecules. The

isotope has a 20 min half-life, which brings advantages for the tracer development workflow. The most obvious advantage lies in the nature of organic chemistry itself, with carbon being present in almost any given tracer candidate. While not every carbon atom is easily replaced by ^{11}C, a fair number of radiochemical synthons and a diverse toolbox of radiochemical reactions make ^{11}C-labeling relatively straightforward [10]. Furthermore, the relatively quick decay rates make it possible to use radiochemistry equipment and animals for preclinical imaging multiple times within a day. However, ^{11}C synthesis infrastructure is not nearly as expansive as for ^{18}F and for all practical aspects ^{18}F is preferred for established tracers.

The difficulty of ^{18}F tracer development is often rooted in the chemical limitations of fluorination, which is not nearly as versatile (yet) as ^{11}C chemistry. As another confounding factor, the choice of targets worth labeling and the design of appropriate methods are inevitably linked, yet determined by factors from largely unrelated scientific areas respectively and the real challenge in tracer design is a deep understanding of both domains, and perseverance [11] Over the last decade, ^{18}F-radiochemistry experienced a strong renewed interest from organic chemists and several novel methods to fluorinate a variety of substrates has been developed. While the development of new PET tracers has been stated the motivation for many of these efforts, the pace of tracer development has not picked up at the expected rates [12].

To clarify some of the difficulties, a case study can be helpful. Figure 1.1 illustrates a typical example of a set of molecules synthesized to identify HDAC6 selective inhibitors [13]. As usual, some of the candidates are inactive (shown in red). It is not yet fully possible to reliably predict the tracer properties of any molecule at that stage,

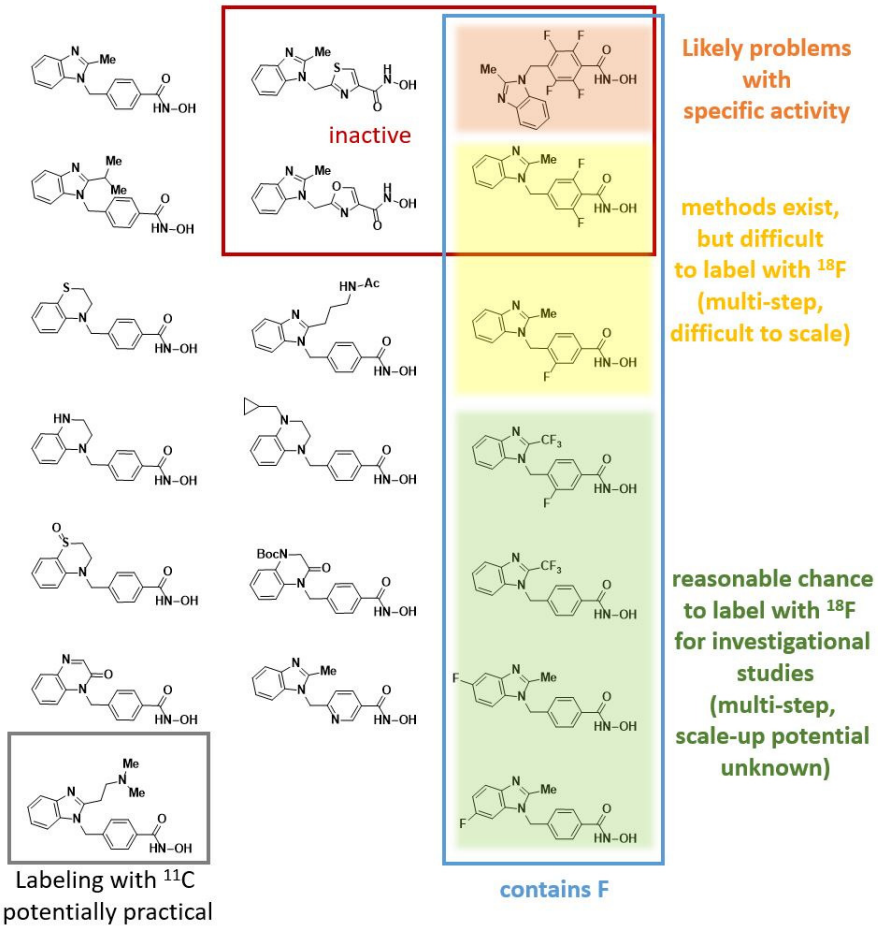

Figure 1.1: Radiotracer development based on traditional medicinal chemistry. A case study based on a traditional compound collection from the medicinal chemistry literature emphasizes the challenges for radiochemists with respect to suitable radiolabeling methodology (table adapted from Shen and coworkers [13])

but we can think about which ones are potential tracer candidates from a practical standpoint. Of the candidates not containing fluoride, only one is easily methylated with ^{11}C. Around a third of the molecules contains fluoride, which is a high percentage compared to most average medicinal chemistry reports - many not containing fluoride at all [14]. Out of 7 molecules containing fluoride, 4 offer reasonable strategies for labeling [15, 16]. Since all four molecules are structurally very similar, and likely behave very similarly *in vivo*, the chance of failure to develop a tracer based on these molecules is high. This example shows that medicinal chemistry typically is not conducted with tracer development in mind, and in order to be able to take advantage of the vast data generated by medicinal chemists, more general radiochemistry methods are necessary. While certainly innovative, many methods developed in the last years have not led to any successful PET tracers, and on the other hand many molecules that would be potentially interesting still cannot be labelled efficiently. In Figure 1.2, the disconnect between reality and optimal radiolabeling method development is schematically depicted. Molecules are chosen based on their affinity and selectivity for a target of interest in a first iteration, represented by the blue "filter". Out of any set of structures with affinity for a target of interest, only a subset will have properties suitable for tracer applications, indicated by the yellow bar. This stage can be tricky to navigate; it is very difficult to predict several crucial parameters, like blood brain barrier penetrance or non-specific binding without actual imaging experiments. This selection process can thus be accomplished either through computation, as exemplified in Chapter 4, or through experimental screening like in Chapter 3, the latter being significantly more costly, slower and dependent on already available radi-

olabeling methods. The third tier in the graphic can be understood as the practical limitations of radiosynthesis. In order to obtain a radiotracer that can be routinely employed, the radiosynthesis and purification process need to be exceptionally robust and compliant with a plethora or regulations. Currently, many of the efforts toward novel radiofluorination methods are opportunistic, based on non-radioactive fluorination methods and adapted to radiochemistry, often without consideration of practical and regulatory aspects (Figure 1.2b). Recognizing the value of the opportunistic approach to increase our fundamental knowledge about ^{18}F chemistry and providing a basis for the development of improved, modified methods, it would be much more efficient to consider the molecular targets or desirable target classes and develop radiolabeling reactions with clear scaffolds and the practical limitations of a radiopharmaceutical production environment in mind (Figure 1.2c). A similar approach has been operative in organic total synthesis, where target molecules dictated the development of new methodology for decades, as opposed to the current development in ^{18}F radiochemistry, where the availability of ^{18}F radiotracers is largely limited by opportunistically developed fluorination reactions. A big part of the challenge is the identification of compounds or compound classes worth developing general labeling methods for. Already established compound classes that are notoriously difficult to label but for which there is high interest are carbohydrates, nucleotides and molecules containing unprotected basic amines.

It was a major goal of the work towards this thesis to showcase successful target-driven radiolabeling method development and how reliable access to "tracer-like" compound classes can expedite tracer development as a consequence. Any such ap-

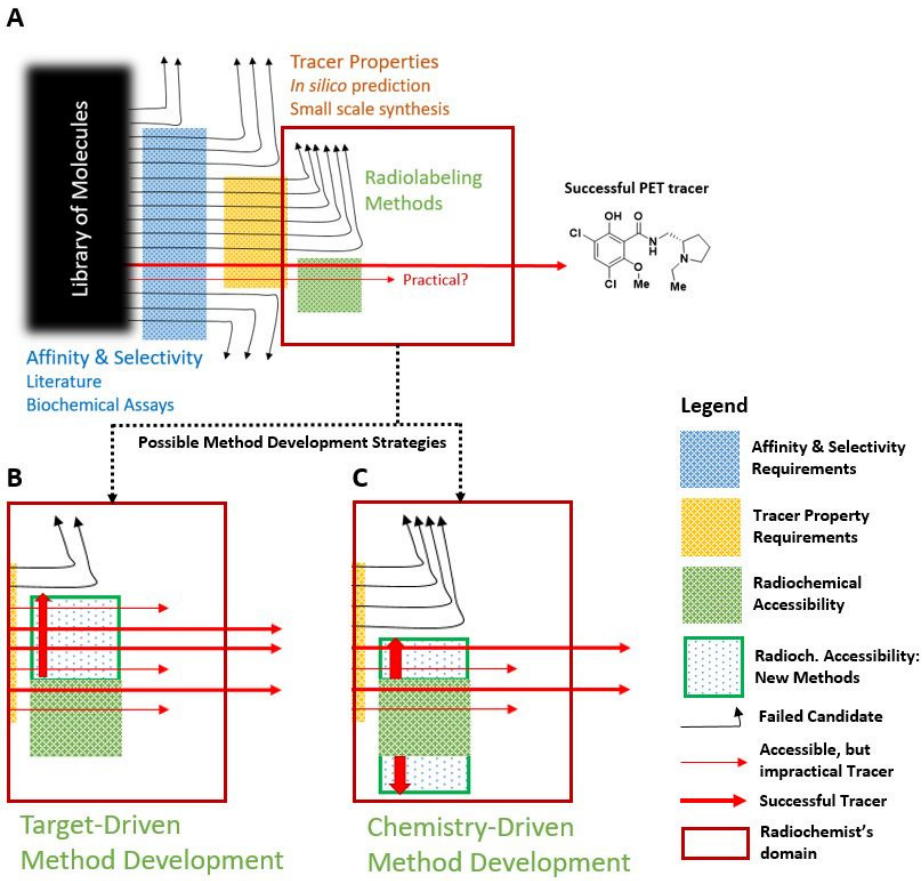

Figure 1.2: Interplay between radiolabeling methodology development and tracer development. Each arrow represents one tracer candidate. The colored blocks represent hurdles towards tracer development. A To be a successful tracer, the molecule has to show affinity and selectivity, suitable tracer properties like low non-specific binding and (practical) radiolabeling methods have to be available. B Target-driven method development can make the process more efficient than C purely chemistry-driven method development

proach is necessarily rooted in organic chemistry, which constitutes both the basis for radiofluorination methodology and medicinal chemistry. Beyond a broad mechanistic understanding of carbon-fluorine bond formation, practical experience in radiochemistry and the engineering of automated radiosynthesis, it was paramount to identify an unmet medical need that can be addressed by molecular imaging, but suffers from challenges in radiolabeling in its translation. In the following chapters, I will showcase how our understanding of epigenetic enzymes and their role in the human brain motivated the development of novel radiofluorination methodology, which in turn offers new avenues to deepen our understanding of said enzymes in the living human brain through PET imaging.

1.2 Radiosynthesis of ^{18}F radiotracers

In order to comprehend the fundamental advances presented in subsequent chapters, it is important to review the radiofluorination strategies and methodology as a context for the work to be described. A number of strategies exist to incorporate ^{18}F into PET radiotracers. On the most fundamental level, ^{18}F can be obtained in two different chemical forms, [^{18}F]F_2 and [^{18}F]fluoride [10]. The major difference is the mode of reactivity that is accessible through either form. While fluorine gas reacts through electrophilic pathways, fluoride is inherently a nucleophile, albeit a poor one. In many cases, fluorine gas is not a practical option for several reasons. The major disadvantage of fluorine gas is its diatomic nature. Production of the ^{18}F nucleus occurs on nanomolar scales, and the process requires the use of ^{19}F carrier gas. The consequences are twofold: First, only half the fluorine atoms are transferred into

the target molecule in the vast majority of reactions, fundamentally limiting the yield to 50%. Second, even minute amounts of carrier gas dilute the specific activity significantly, which prohibits the use of F_2 for tracers requiring high specific activity. In select radiochemistry facilities the synthesis of "high specific activity" fluorine gas and reagents derived thereof has been achieved [17, 18], but remains challenging to adapt and has therefore not found widespread application. While a considerable literature about radiolabeling methodology with fluorine gas exists [10], the focus will be on [^{18}F]fluoride for the rest of this thesis for these reasons.

One of the most commonly used strategies for ^{18}F-labeling is the use of prosthetic groups. Traditionally the term "prosthetic group" refers to a non-peptide group introduced to a peptide, but for the purpose of this thesis denotes the use of a small, easy-to-label moiety that can easily be associated with a more complex small molecule after introduction of a radioisotope. Classic examples are small organic molecules like fluorobenzaldehyde [24–27] or fluoroethyltosylate [21, 28], which can be radiolabeled with nucleophilic substitution chemistry and subsequently linked to the molecule of interest with well-established reactions. A more modern variant of prosthetic groups is based on elements with high affinity for fluoride in a precursor and their ability to undergo rapid and efficient fluoride adduct formation. The most prominent examples for the latter are fluorosilanes [29, 30], trifluoroborates [19, 31–44] and fluoroaluminates [45–50] (Figure 1.3a). The great advantage of prosthetic group is the practicality of radiolabeling, which is mostly based on reliable preparation of a labeling synthon, which is easily introduced into most structures. Figure 1.3b illustrates both the advantages and disadvantages of prosthetic group strategies. While the syn-

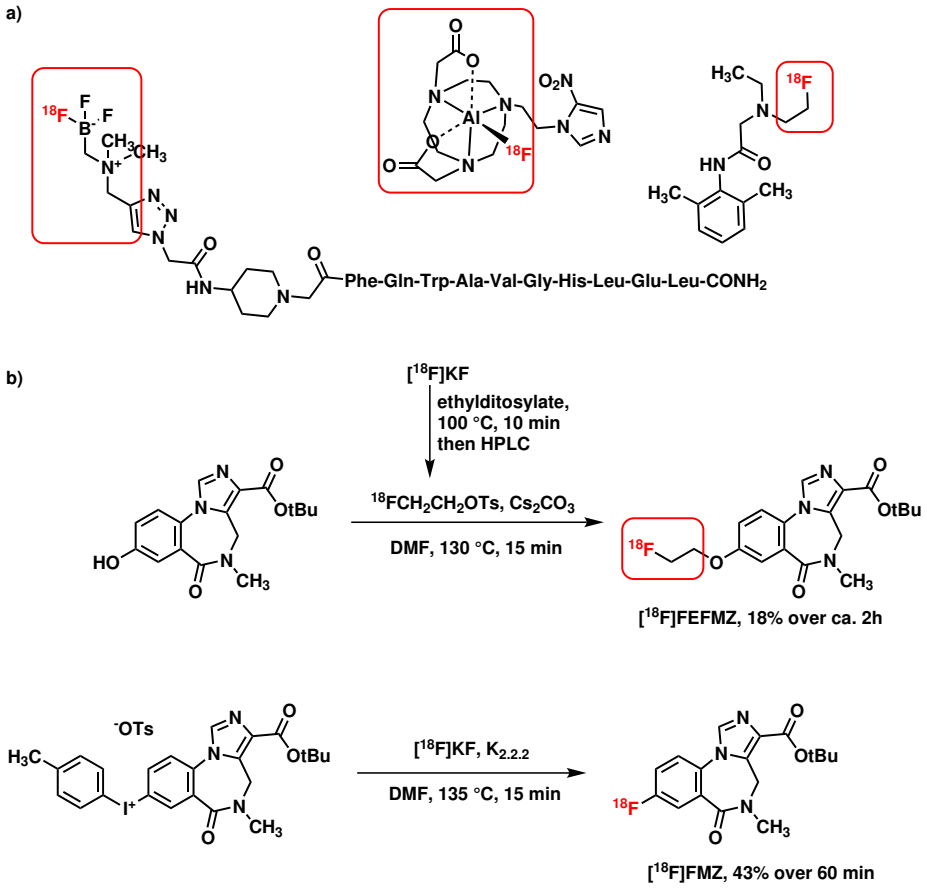

Figure 1.3: Examples for the use of "prosthetic groups" in ^{18}F-radiolabeling a) An RGD-peptide containing a trifluoroborate group for oncological imaging applications [19], nitroimidazole tagged with an aluminum [^{18}F]fluoride [20] and [^{18}F]radiocaine [21], containing a fluoroethyl group are examples for the use of prosthetic groups in radiolabeling. b) Radiosynthesis of [^{18}F]fluoroethylflumazenil [22] in comparison to [^{18}F]Flumazenil [23]

thesis of [^{18}F]FEFMZ allowed investigational studies without major optimization of the route, [^{18}F]FMZ required the development of new labeling techniques (iodonium salt precursors). However, with the new, suitable one-step direct labeling procedure in place, the yield of [^{18}F]FMZ synthesis profits from both the shorter synthesis time and the absence of intermediate purification, transfers and the related losses in activity. This approach highlights the desperate need of radiochemists for practical methods. The structural changes necessary to incorporate these prosthetic groups rarely improve the molecule's physiochemical properties − quite the opposite − but still constitute the most popular approach for introduction of ^{18}F into tracers at an early stage of tracer development. The direct fluorination of small molecules can be more difficult, but does not usually require significant structural changes to the molecular scaffold. Leaving practical aspects aside, it is the preferred strategy in ^{18}F-radiotracer design. The most prevalent fluorination reaction to introduce [^{18}F]fluoride is a traditional S_NAr reaction with a good leaving group (e.g. trimethylammonium, nitro, iodonium) on an electron poor arene [51, 52].

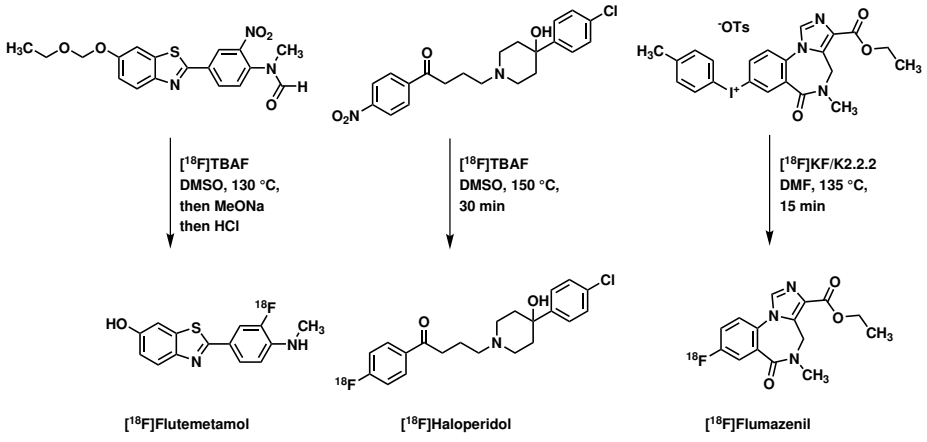

Figure 1.4: **Traditional radiosyntheses of [^{18}F]fluoroarenes via S_NAr reactions**

While a number of tracers can be accessed using this chemistry (Figure 1.4) [23,53,54], its application is inherently limited by the substrate's electron density. To expand the radiochemical toolbox, chemists have explored alternative reactions to radiofluorinate arenes and over the last decade a wealth of new methods has been published [51, 52]. They can roughly be categorized into two groups: 1. Transition metal mediated C–F bond formation (Figure 1.5) and 2. "Enhanced" nucleophilic aromatic substitution, with the traditional mechanism but innovative leaving groups. A report by the Hooker and Ritter [55–57] groups about a Pd(IV) reagent capable of inverting the inherent reactivity of fluoride pioneered the field of transition metal mediated radiofluorination. The method allows the radiochemist to radiolabel arenes in an electrophilic-like reaction mode, giving access to much more electron rich substrates than traditional S_NAr chemistry. While conceptually revolutionary, the method suffered from practical difficulties [55]. The reaction is air and moisture sensitive and requires intermediate purification of the Pd(IV) fluorinating reagent, limiting its practical use dramatically. Based on the same principles, a next-generation fluorination method based on Nickel was developed by the same groups [58]. Aryl-nickel complexes were shown to undergo C–F bond formation at room temperature in less than a minute and tolerate low amounts of water, alleviating several of the practical difficulties of the Pd-based method [59]. It was possible to validate the synthesis of [^{18}F]Fluorouracil for human radiopharmaceutical production [60]. However, the technical aspect of the process is still challenging and has not been adapted in routine radiopharmaceutical production environments since the proof-of-concept efforts at Massachusetts General Hospital. Both methods require the synthesis of organometallic complexes as labeling precur-

sors, which is challenging and presents a significant barrier for the typical radiochemist or radiopharmacist. Seeking to enable the use of commercial precursors, the Gouverneur group developed a copper-mediated radiofluorination of boronic esters [61]. The method utilizes a commercial Cu(I) complex and fluorination is achieved with air as an oxidant. The method is not sensitive to airborne moisture and the large-scale production of radiopharmaceuticals like F-DOPA has been demonstrated with this approach [62]. While the method is a significant advance, the synthesis of boronic esters can be at times difficult, and particular compound classes (e.g. amines, carboxylates) are incompatible with this approach.

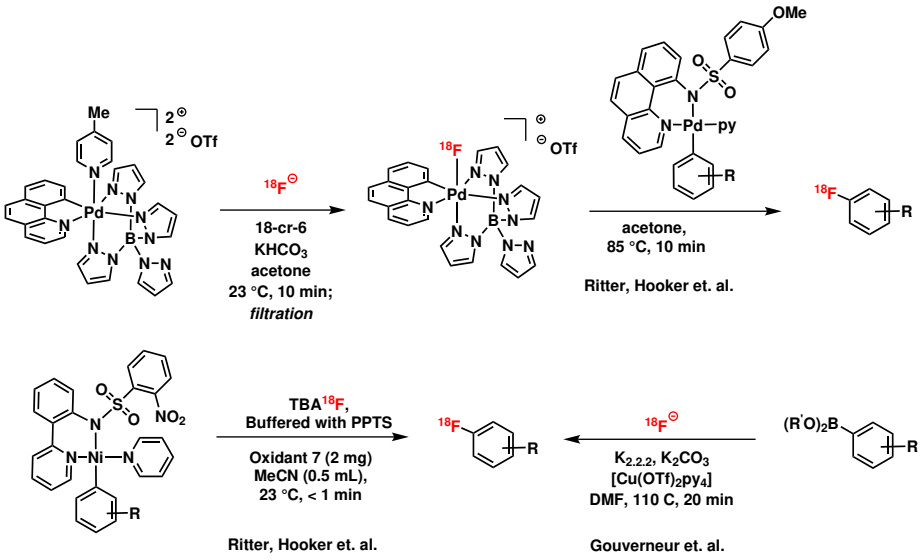

Figure 1.5: Modern ^{18}F-radiolabeling methodology involving organometallic intermediates; A Pd(IV) compound that can be converted into an electrophilic [^{18}F]fluorinating reagent to afford aryl fluoride from organopalladium(II)complexes, a Ni(II)aryl complex substrate for oxidative fluorination with ^{18}F and a copper-mediated fluorination of boronic esters are examples for state-of-the-art radiofluorination methodology

The other general strategy for the development of new ^{18}F-labeling methods has been based on the traditional S_NAr approach, but a broader substrate scope was achieved

by enhancing the reactivity of arene precursors towards nucleophiles. One example is the use of solid titanium oxide in combination with aryl tosylates [63]. The sulfonyl moiety was shown to be activated by coordination to the solid TiO_2-phase. Fluoride was bound to the same surface and the nucleophilic substitution occurred effectively through a mechanism reminiscent to classic solid-phase catalysis. The substrate scope of the method however mostly covered aliphatic substrates, while aromatic tosylates were challenging. Iodonium salts as precursors for S_NAr have extended the scope of the reaction, and chemists were able to further increase their reactivity by means of copper catalysis [64] or sophisticated design of the iodine substitution pattern or the use of iodine ylids [65, 66]. These methods are reliable and easy to adapt on scale, but like the traditional S_NAr reactions with iodonium salts, the precursor synthesis is challenging and limits the application to more complex molecules or scaffolds incompatible with the conditions under which the iodonium moieties are installed. A distinct approach was published by the Ritter group in 2016, employing phenols as precursors for deoxyfluorination via an uronium salt intermediate [16]. Phenols have many advantages as precursors, since they are typically bench stable compounds, often commercially available or easy to synthesize, they can be purified by most standard techniques and do not introduce inherently toxic elements to the reaction. The method proceeds via the formation of a uronium salt, which is able to capture fluoride from an anion exchange cartridge and undergo fluorination via an atypical concerted S_NAr mechanism. The method is not air and moisture sensitive and in principle amendable to scale up. However, the substrate scope is limited to electron poor arenes, much like classic S_NAr reactions.

In summary, several innovative radiofluorination methods have been developed and shown to be useful, but most of them have severe limitations with respect to substrate scope and practicality of scale up. While a substantial number of molecules can be accessed, I will present examples for electron rich arenes, which cannot be fluorinated with any of the above-mentioned methods despite great potential in imaging applications.

1.3 Epigenetic dysregulation in brain disease: histone deacetylases

Beyond the availability of practical radiolabeling, it is important to choose the target for any molecular imaging probe carefully [11]. The power of any data set acquired with any given imaging technique is fundamentally limited by the inferences that can be drawn from information about the observed protein target or metabolic function. One class of targets we believe to be the basis for a powerful imaging technique, and which will be the focus of the subsequent chapters, is introduced in this section.

Although the genetic material of every cell in our body is identical, the proteome varies greatly between cell types and tissues because the expression of genes is differentially regulated by mechanisms beyond the primary structure of our DNA [67]. These mechanisms, which dynamically regulate the transcription of DNA in response to external or environmental factors, and lead to heritable phenotypes, are collectively termed epigenetics [68, 69]. Among a variety of different molecular regulation mechanisms, acetylation of histones is a key determinant of chromatin packing and gene

transcription [70]. Two classes of enzymes, histone acetyl transferases [71] (HATs) and histone deacetylases [72, 73] (HDACs) work together to precisely regulate the acetylation state of the cellular proteins, including but not limited to histones [74–76]. Particularly the enzymes which remove acetyl marks, HDACs, have come into the focus of therapeutics research after small molecule inhibitors of HDACS have shown potential in treating certain cancers and several inflammatory conditions [77].

1.3.1 Classificaton of histone deacetylases and their involvement in brain disorders

There are 18 HDACs in humans, out of which 11 are zinc-dependent. 7 are NAD-dependent and typically referred to as sirtuins or class III HDACs (Figure 1.6) [78]. The latter won't be discussed further in this thesis. The zinc dependent isoforms 1-11 are divided into different classes based on their structural homology to yeast proteins. Class I contains isoforms 1-3 and 8, Class IIa consists of HDAC 4, 5, 7 and 9, Class IIb contains HDAC6 and 10 and Class IV only consists of a single member, HDAC 11, which has no homolog in yeast. Class I and IV are mostly located in the nucleus with exception of HDAC8, which is located both in the cytosol and the nucleus, and occurs in a membrane-associated form. Class II HDACs are primarily located in the cytoplasm, but class IIa can shuttle between the cytosol and the nucleus depending on their phosphorylation status [79].

As major regulators of gene expression, a rich vault of data about the involvement of HDACs in cancer exists, and several HDAC inhibitors (HDACi) are in approved for oncological indications or in clinical trials [77]. Inflammatory disease has emerged

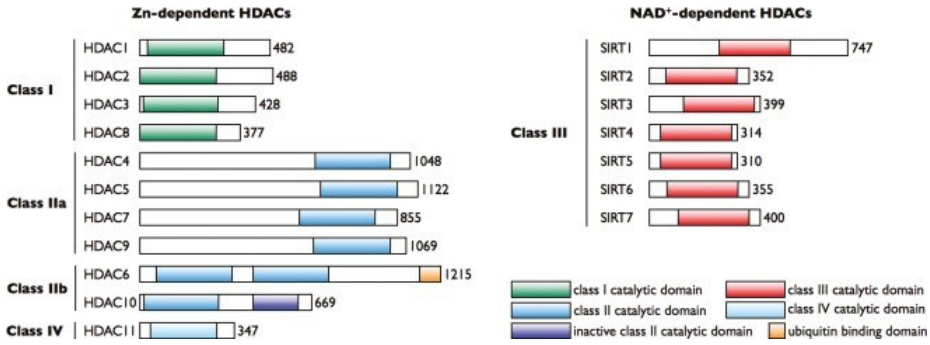

Figure 1.6: HDACs are classified according to their homology to yeast proteins (adapted from [80]): Class I, II and IV are Zn-dependent, class III is NAD^+-dependent. Class IIb has a second catalytic domain, which is only active in HDAC6. A ubiquitin binding domain is another crucial functional element of HDAC6

as another area in which HDACi have great therapeutic potential and avenues of treatment are explored [81]. While many links of HDAC dysregulation to psychiatric and neurodegenerative disease have been unraveled, the translational process towards effective therapeutics has been considerably slower in this domain [82, 83]. Among other reasons, the heterogeneity of many brain disorders and our poor understanding on a molecular biological level complicates the design of valid therapeutic targets and evaluation of potential therapeutics. A multitude of studies exists that link altered HDAC expression or activity to Alzheimer's disease [84], major depressive disorder [85], schizophrenia [86,87], bipolar disorder [87], and potentially learning disability [84, 88]. Therapeutic HDAC inhibition also seems a promising strategy for the treatment of Huntington's disease [89, 90]. The most extensive study on HDAC1 and HDAC2 transcript levels to date found significantly altered transcript levels of HDAC2 in the dorsolateral prefrontal cortex in schizophrenic patients, but no changes in HDAC1 and no changes in other brain regions [91]. The study demonstrates the correlation of regional dysregulation of specific HDAC isoforms to disease. Conse-

quently, to verify postmortem findings in patients, the need for tools to quantify HDACs with regional specificity in living patient populations is evident.

1.3.2 HDAC complexes and their selective inhibition

The biological role of HDACs is critically influenced by their engagement in quaternary protein complexes [92]. Several core complexes have been well described and attributed distinct biological functions. Some of the most well studied HDAC complexes are mSin3A, CoREST, NuRD and NCoR [93–97]. The first three are built around a core homo- or heterodimer of HDAC1 and HDAC2, whereas NCoR contains HDAC3, and each complex has distinct biological funcions. Chemoproteomic analyses of HDAC inhibitor behavior revealed that the protein complex can influence the binding of HDAC inhibitors, and that selectivity criteria not reflected in traditional recombinant IC_{50} assays are crucial to understand the behavior of these molecules as therapeutic agents [98, 99]. These findings suggest that knowing the precise complex selectivity of an HDAC inhibitor used in PET imaging could give information not only about the distribution of HDAC isoforms, but rather about the gene regulation state of brain regions of interest. In Chapter 3.3 this concept will be described in more detail.

1.3.3 HDAC6 and its selective inhibition

Structurally, class IIb HDACs are distinct from other isoforms because they have two active sites, and while in HDAC10 one of them is inactive HDAC6 has two fully functional zinc centers, in addition to a ubiquitin binding domain and a cytosolic

location signal [80]. HDAC6 does not regulate histone acetylation but rather regulates the acetylation state of α-tubulin [100] and stress-related proteins such as HSP90. HDAC6 has received interest, since HDAC6-selective treatment regimens have shown promise to avoid many of the side effects of first-generation pan-HDAC inhibitors [101]. A more mundane aspect is simply that isoform selectivity for particular HDACs is extremely hard to engineer and HDAC6 (along with HDAC3 [102–104] and to a lesser extent HDAC8 [105, 106]) is structurally different enough from other isoforms to offer a starting point for rational design of selective inhibitors. Most notably steric bulk has been a key strategy to prevent hydroxamates from binding most HDAC isoforms with the zinc active site shielded with amino acid side chains, while HDAC6 has a much more accessible active site [107, 108]. Work that led to the development of the first HDAC6 selective inhibitor [109] suggests that large polycyclic structures are capable of differentiating HDAC6 through interactions on the protein surface beneath the entry tunnel to the active site. Wagner, Holson and coworkers however established that it is largely sufficient to ensure sp^2-hybridization of the carbon in the α-position of the hydroxamate to achieve selectivity [110]. X-ray crystallographic studies of both HDAC6 catalytic domains conclude that two factors contribute to the isoform selectivity of HPOB [111]: 1) Selective inhibitors have diminished potential to interact with a surface motif which confers affinity to class I HDACs and 2) HDAC6 inhibitors tend to bind the Zn-center in a κ^1-mode via the hydroxylamine -OH, whereas pan-HDAC inhibitors bind in a κ^2-mode, hence additionally with the carbonyl oxygen. Both effects were caused by the lack of a linker between the Zn-binding group and an sp^2-hybridized carbon, restricting the depth

of reach of HDAC inhibitors into the entry tunnel. As a class IIb HDAC, it is most closely related to HDAC10, both possessing two catalytic sites. However, HDAC6 is the only histone deacetylase where both of those sites are active [111, 112]. Another noteworthy feature is the ubiquitin binding domain, which is paramount for the role of HDAC6 in protein degradation pathways. HDAC6 is crucial for both the formation and autophagy of aggresomes [113–115], and it has been demonstrated that the Lewy-bodies encountered in Parkinson's disease and other α-synucleinopathies share key features of aggresome biology. The characteristic protein depositions are significantly enriched with HDAC6, which is colocalized with α-synuclein. Interestingly, inclusion bodies in other plaque-forming dementias and Alzheimer's disease do not show the same recruitment of HDAC6 [116]. The formation of stress granules is dependent on HDAC6 [117], and HSP90 [118–120] is a well-established substrate of HDAC6, both indicating the isoform's importance in cellular stress response mechanisms. Another important substrate is α-tubulin, with far-reaching implications in diseases with reduced motility of organelles, intracellular transport and dysregulated cell cycle [100]. Aberrant HDAC6 expression levels have been heavily implicated in the pathophysiology of Glioblastoma multiforme [121–123], Rett syndrome [124, 125], major depressive disorder, Alzheimer's [126, 127] and Parkinson's diseases [80, 113, 128]. In mouse models, the correlation of HDAC6 expression and activity with anxiety, stress and depression-like behaviors is well documented [129–134] and HDAC6 mRNA was found to be decreased in depressed and remissive patients [135]. HDAC6 deficiency also disturbs dopaminergic signaling and influences associated behavior [136]. However, our understanding of these correlations in the living human brain remains limited, largely

due to the difficulties studying the biochemistry of the human CNS. Furthermore, the design of brain-penetrant HDAC6 selective agents has proven challenging, and high doses are needed to achieve functional effects of HDAC6 inhibition [131].

1.4 PET imaging of HDACs

While a solid body of evidence suggests that HDACs are promising therapeutic targets and potent small molecules exist and continue to be developed, our understanding of the immediate relevance of HDACs for brain disorders remains limited due to the difficulty of studying the living human central nervous system. In this section, a review of the field of HDAC-PET imaging is presented to better understand the context of work presented in later chapters of this dissertation. Several strategies toward HDAC PET tracers have been pursued, to varying degrees of success. Two fundamentally distinct approaches can be identified: 1) Labeling of HDAC substrates, leading to accumulation of fluorinated acetate through irreversible hydrolysis and 2) Labeling of HDAC inhibitors which reversibly bind their respective targets.

The first strategy has yielded several agents which are selective for Class IIa HDACs. Fluorination of acetate on otherwise class I selective substrates changes their selectivity through an interesting mechanism which is rationalized with the distinct active centers of class I and IIa HDACs [137]. Class I HDACs are efficient metallohydrolases, and a crucial component for their function is a hydrogen bond between the substrate amide carbonyl oxygen and a tyrosine in the binding pocket, which lowers the transition state energy associated with a tetrahedral anion, leading to rapid hydrolysis with an activated water molecule. In class IIa, the tyrosine is replaced with a histidine,

which cannot form the hydrogen bond, leading to significantly lower but still measurable hydrolase activity. However, class IIa active centers can accommodate sterically more demanding substrates [138]. H to F substitution on the acetyl moiety of amide substrates increases the steric bulk next to the amide bond, disrupting the fit of the substrate and twisting it out of the optimal position, and the authors suggest that thus the attack of an activated water molecule is disfavored, slowing down hydrolysis by class I HDAC. For class IIa, increasing degrees of fluorination of the acetate only increases the rate of hydrolysis through the increased electrophilicity of the carbonyl, while the steric constraints do not seem to disturb the substrate positioning relative to the activated water molecule. [^{18}F]FAHA [139–144] and analogues [137] (Figure 1.7) have been demonstrated to show HDAC IIa specific signal in the baboon brain and reflect dose-dependent changes in HDAC occupancy induced by SAHA treatment.

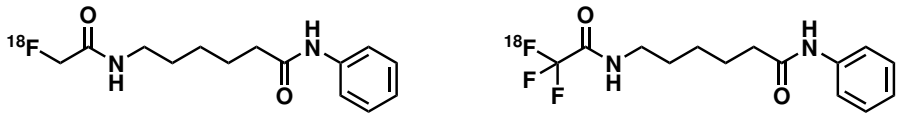

Figure 1.7: FAHA and TFAHA, two class IIa selective HDAC inhibitors suitable for PET imaging

The labeling of HDAC inhibitors to develop PET imaging agents has been particularly challenging with respect to brain uptake and suitable tracer kinetics [145–149]. The product of respective efforts is [^{11}C] Martinostat, a radiolabeled class I and IIb selective hydroxamate HDAC inhibitor [150]. It was hypothesized that a main contributor to its excellent brain uptake was the adamantane substituent, which we will support in Chapter 3. Beyond the CNS, the tracer was useful in imaging HDAC in the heart, and has potential to assess expression levels in the kidneys, spleen and

pancreas.

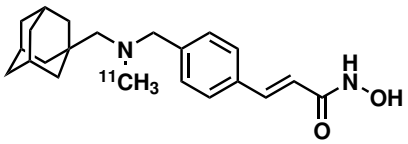

[11C]Martinostat

Figure 1.8: [^{11}C]Martinostat, a class-I and IIb selective HDAC imaging agent

The kinetics of [^{11}C]Martinostat (Figure 1.8) can be described using a 2-tissue compartment model, but it was found that standardized uptake value ratios (SUVR) relative to the whole brain are a reliable measure to quantify the targets of Martinostat [151]. Initial trials concluded that HDAC expression pattern in the human brain is conserved within healthy populations (Figure 1.9) and that systematic study of changes in regional expression levels as a function of disease is warranted [152]. Patients with schizophrenia, Alzheimer's disease, amyotrophic lateral sclerosis, alcohol abuse and Huntington's disease, among others, are currently enrolled or recruited for [^{11}C]Martinostat imaging studies.

The currently available version of Martinostat is labelled with ^{11}C, which limits its practicality, since logistics are constrained by its 20 min half-life. One key achievement presented in this work is the development of an ^{18}F-HDAC-radiotracer, which enables in vivo quantification of HDAC with the various benefits of a longer half-life. Additionally, an ^{18}F-labeled version enabled a detailed resolution of how different functional groups contribute to the remarkable brain uptake of Martinostat. As empirically identified, contribution of a single adamantane substituent was confirmed to be a major driving force for the brain penetrance of Martinostat. However, amine

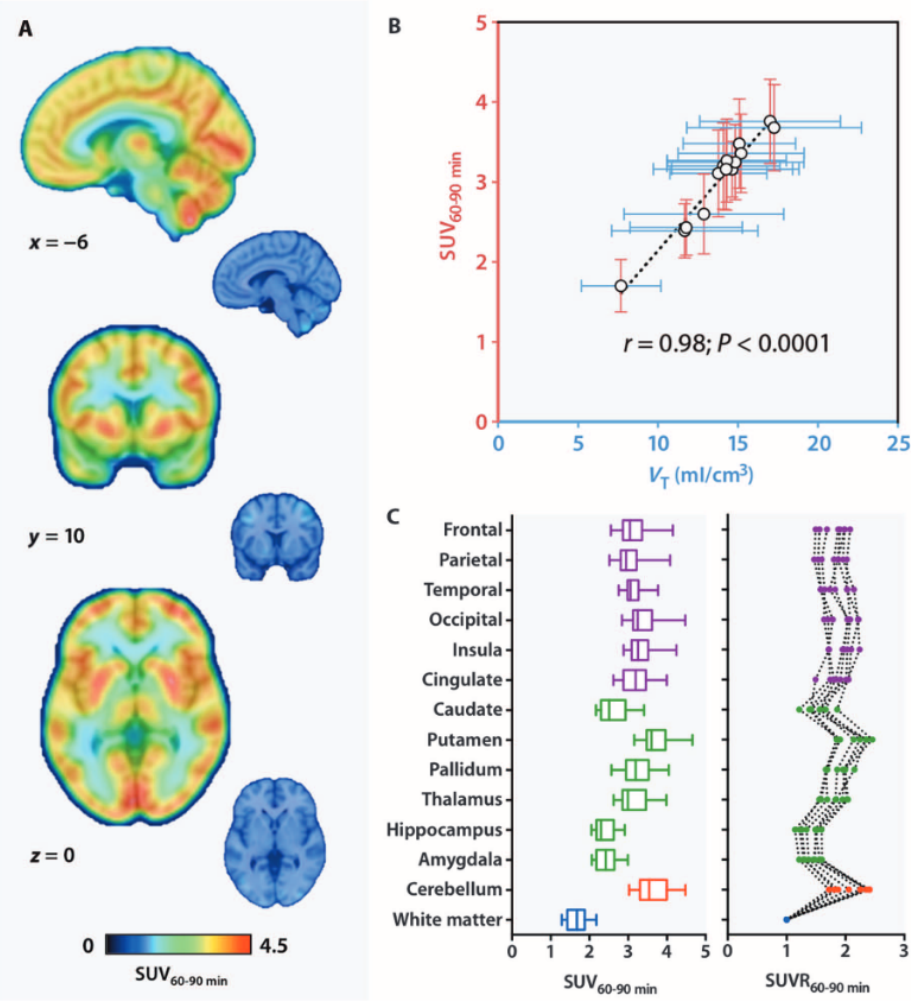

Figure 1.9: HDAC imaging in the human brain with [^{11}C]Martinostat. A Images of [^{11}C]Martinostat in the human brain, averaged from 60-90 min past injecton. B correlation of standardized uptake values with the volume of distribution. C Group summary of regional distribution of [^{11}C]Martinostat in the human brain (from Wey et. al. [152])

methylation significantly increases brain uptake as well. The work toward these findings is discussed in Chapter 3

1.5 Synopsis: Challenges in HDAC imaging

As evident in the last section, it remains challenging to gather quantitative data about HDACs in the human CNS. Several distinct avenues to address this unmet need were subject of this dissertation:

1) The general process of radiotracer development is often inefficient, and radiochemistry is a bottleneck. Especially HDAC inhibitors, which almost always bear amine and hydroxamate moieties, are a class of molecules that is historically challenging to access for ^{18}F radiolabeling methods. One goal addressed in this work is more general synthetic access to these molecules.

2) Even existing HDAC imaging probes are challenging to synthesize and distribute. Conversion of [^{11}C]Martinostat to an ^{18}F probe was another focus in dissertation.

3) The aim of understanding the biological role of single HDAC isoforms in the human brain introduces another layer of complexity to the imaging probe development pipeline. Selective imaging of HDAC6 with PET was the final key point in this body of work.

All three chapters have in common the basic chemical requirement for reliable, practical radiofluorination. A promising solution is presented in Chapter 2.

Chapter 2

Ruthenium Mediated Radiofluorination

This chapter includes work performed by M. Hassan Beyzavi, Debashis Mandal Erica D'Amato and Junting Chen, and is part of a manuscript that has been submitted for publication (currently under review). Hassan Beyzavi carried out most of the radiochemical experiments towards Figure 2.3 and Debashis Mandal determined appropriate Ruthenium complexes to perform the reactions. Erica D'Amato contributed to the conception of the project.

2.1 Meeting unmet needs in radiofluorination

Here we report the first ^{18}F-deoxyfluorination reaction of phenols activated through η^6 π-coordination of phenols to a ruthenium complex. The method combines deoxyfluorination through a PhenoFluor [153, 154]-like mechanism, [16] which ensures

large functional-group-tolerance, with π activation by ruthenium, which expands the substrate scope to even the most electron-rich phenols. As a consequence, the new ^{18}F-fluorination reaction is projected to exceed the accessible molecular diversity of ^{18}F-labeled molecules beyond what is currently obtainable with any conventional or modern arene ^{18}F-fluorination reaction. We further show that the transformation can be automated and scaled to provide labelled materials suitable for human PET imaging (Figure 2.1).

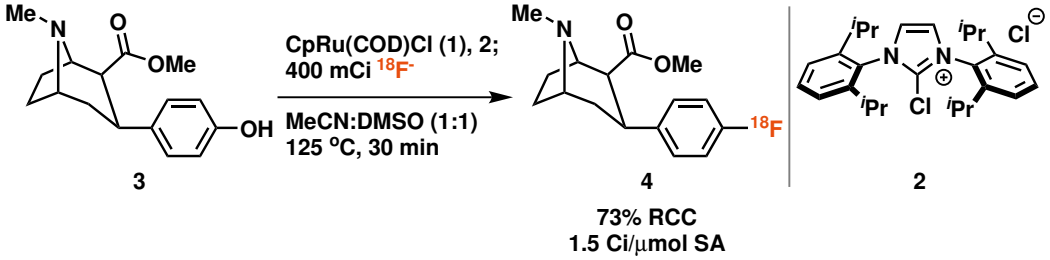

Figure 2.1: Synthesis of β-CFT via ruthenium-mediated deoxyfluorination.

Cognizant of the challenges we have observed with high-valent metal redox chemistry in ^{18}F-fluorination, we developed a metal-free ^{18}F-deoxyfluorination of phenols [16]. The method is exceptionally functional group tolerant, to the best of our knowledge, more so than any other late-stage fluorination reaction. The functional group tolerance could be rationalized through a mechanism analysis: The key tetrahedral intermediate features a non-basic, neutral organofluoride (B), which rearranges to product (Figure 2.2a). The tetrahedral intermediate (B) is in equilibrium with its corresponding uronium fluoride ion pair (A). The equilibrium is inconsequential for reactions with excess ^{19}F-fluoride [154,155]. But because [^{18}F]fluoride is used as the limiting reagent, detrimental side reactions from the ion pair (A) sequester [^{18}F]fluoride irreversibly, especially if the equilibrium constant K_1 is small, as is expected for electron-rich

phenols. As a consequence, although highly functional group tolerant, the substrate scope for current ^{18}F-deoxyfluorination is limited; and electron-rich phenols cannot be ^{18}F-deoxyfluorinated, despite the productive reaction with ^{19}F. Our strategy to device a more general reaction entailed to increase the equilibrium constant K, specifically $K_2 \gg K_1$. It is well established that $\eta^6 - \pi$-coordination of arenes to certain transition metal complexes reduce electron density of the arene, and activate the arene for nucleophilic aromatic substitution [156–162], although such a strategy has not been successfully implemented for general ^{18}F-fluorination reactions (Scheme 2.2b). Here we disclose the successful implementation of a practical, robust ruthenium-mediated ^{18}F-deoxyfluorination of both electron-rich and electron-poor phenols. The reaction retains the desirable features of deoxyfluorination without ruthenium and can tolerate nucleophilic functional groups such as amines. In contrast to the redox active ^{18}F-fluorination reactions with Pd, Ni, and Cu, the Ru center does not undergo redox chemistry, nor does the reaction proceed through high-valent complexes that could engage in undesired side reactions with amines or other nucleophilic groups.

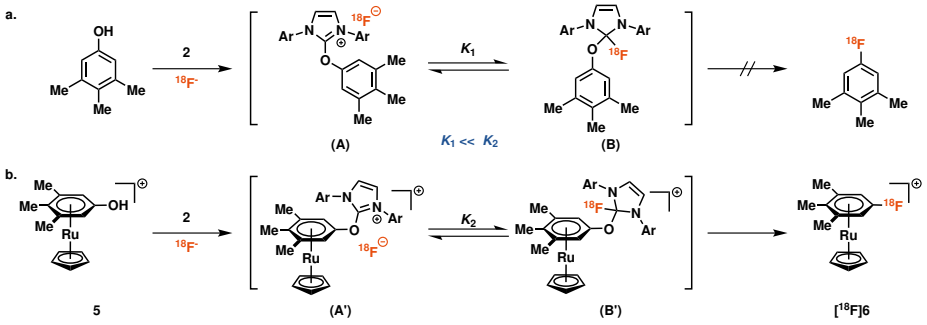

Figure 2.2: a) Concerted nucleophilic aromatic substitution (CS_NAr) via B to furnish the fluorinated arene. K_1: equilibrium constant. Ar = 2,6-diisopropylphenyl b) The ruthenium fragment decreases the electron density of the phenol, which renders the tetrahedral intermediate more favorable – $K_2 \gg K_1$. [^{19}F]6 was obtained in 75% yield from 5.

2.2 Development, scope and automation of Ru-mediated radiodeoxyfluorination

Heating the air and moisture stable Ru complex 1 with a phenol in ethanol for 30 min at 85 °C affords a solution of ruthenium phenol complex, e.g. 5; subsequent addition of chloroimidazolium chloride 2 provides a solution, which is used to elute [^{18}F]fluoride off an anion exchange cartridge. After addition of a 1:1 DMSO/acetonitrile (v/v) solution, the reaction mixture is heated for 30 min to afford aryl fluorides. No precautions to exclude moisture or air are necessary at any point in the process.

In line with our goal, electron-rich substrates like anisole (7a) and dialkylaniline derivatives (7c) show high radiochemical conversion (RCC). A variety of functional groups is tolerated, most importantly basic amines (7b, c, i, l) which can present a major limitation to several available radiofluorination methods [15, 57, 58]. Protic functional groups (7e, j, n) are unproblematic and phenolic hydroxyl groups can be selectively deoxyfluorinated in the presence of unprotected aliphatic alcohols without affecting carbinol stereochemistry (7h, l). Additionally, several heterocyclic scaffolds, including pyrimidines (7m), indoles (7o) and quinolines (7k) are good substrates for the reaction. Ortho-substitution is tolerated (7k, o). (Figure 2.3)

The overall yield of the reaction is affected by the RCC and elution efficiency (EE) of [^{18}F]fluoride off the anion exchange cartridge, and both were addressed when optimizing reaction conditions. Chloride as counterion (X) for CpRu(COD)X gave high yields, but both bromide and iodide diminished the RCC, possibly due to competi-

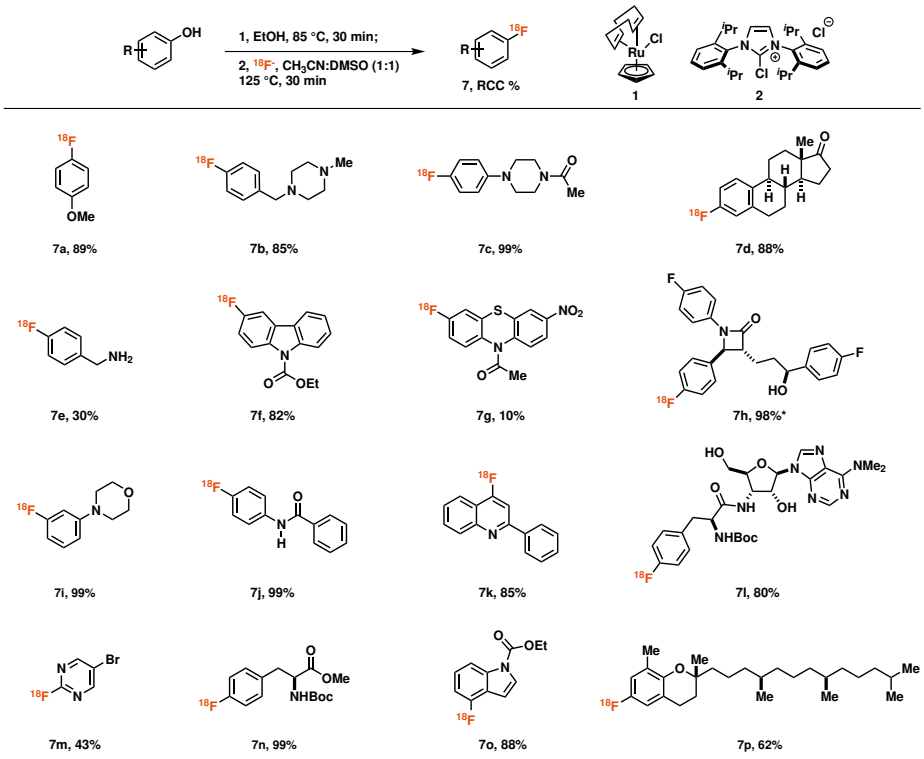

Figure 2.3: Substrate table for ruthenium-mediated ^{18}F-deoxyfluorination of phenols; RCC = Radiochemical conversion determined as fraction of product radioactivity of total counts by radio-TLC *26% isolated non-decay-corrected yield

tive nucleophilic attack. EE and RCC improved with higher concentration and molar excess of both 1 and 2. The minimal increases in yield obtained by more than three equivalents of 1 and 2 did not justify the expenditure of reagents and additional purification difficulties. Both EE and RCC were higher when ethanol was present in the reaction mixture. While more than 30% ethanol was detrimental to the fluorination, low solvent volumes were impractical to handle and we continued our work with 50 μL ethanol in 400 μL total reaction volume. Although several salt additives increased elution efficiency, the gain was offset by a reduction in RCC. None of the additives investigated improved the overall yield. Reaction temperatures below 125 °C and reaction times less than 30 min afforded lower yields of product.

For any ^{18}F-radiolabeling methodology to be practically useful, it needs to be amenable to automation on commercial radiosynthesis modules. On an Elixys (Sofie Biosciences) radiosynthesizer, we were able to perform the reaction in a fully automated fashion: from 461 mCi of [^{18}F]fluoride obtained in aqueous solution from a cyclotron, we were able to isolate 111 mCi of purified, protected [^{18}F]fluorophenylalanine derivative 9 within 80 min (Figure 2.4). The stereochemical purity of the starting material was maintained throughout the reaction. Initially, yields of the automated syntheses were more than tenfold lower than in manual experiments. The main factors responsible for the lower yields were identified as vial size and the associated headspace, and the use of 4 mL instead of 10 mL reactors resolved the issue. It is crucial to ensure that an internal temperature of 125 °C is reached when using a vial adapter. In commercial radiosynthesis systems for which smaller vials are not commonly avail-

able, high pressure is an alternative strategy to counteract the larger headspace. For example, in a Siemens Explora FDG4 system, an increase in pressure from 30 kPa to 205 kPa during the reaction improved the RCC toward protected fluorophenylalanine fivefold.

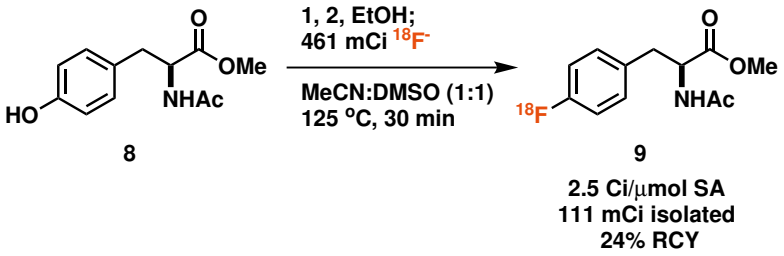

Figure 2.4: Fully automated ruthenium-mediated ^{18}F-deoxyfluorination of tyrosine derivative; 111 mCi isolated RCY (24 %) is non-decay-corrected

The ruthenium mediated dexoyfluorination presents a valuable addition to the radiochemical toolbox. Very electron rich substrates are challenging to fluorinate with conventional radiofluorination reactions, but unproblematic for this approach. Basic amines and ortho-substitution are fully compatible. The substrates are readily accessible and stable phenols. The reaction is operationally simple, can be executed in air in the presence of moisture, and automation is established. The method is broadly applicable and easy to adapt in a radiopharmaceutical production environment. A current technical limitation of the reaction is the requirement for 30-40 mg total mass of reagents (combination of phenol, 1 and 2), which can complicate purification and is not economic. Although several heterocyclic substrates are efficiently radiofluorinated (7k, 7m, and 7o), we have found that in certain cases the presence of heterocycles will interfere with efficient ruthenium complex formation. We attribute this fact to their ability to coordinate to the ruthenium center in modes detrimental to product

formation. Mechanistically, the slowest step in the sequence is product decomplexation. The reaction requires 30 min of heating, which reduces the yield by 20% merely through radioactive decay. Decomplexation could potentially be improved by more sophisticated design of the ruthenium ligand environment [163–166]. The elution efficiency is as low as 49% in some cases, which is an additional factor that limits the yield. Higher ionic strength of the eluent solution is a possible remedy, and efforts are ongoing in our laboratory to develop improved ruthenium complexes and imidazolium reagents to expand the utility and generality of the promising ^{18}F-deoxyfluorination reaction.

2.3 Experimental

2.3.1 Chemical synthesis

[CpRu(cod)Cl] (1)

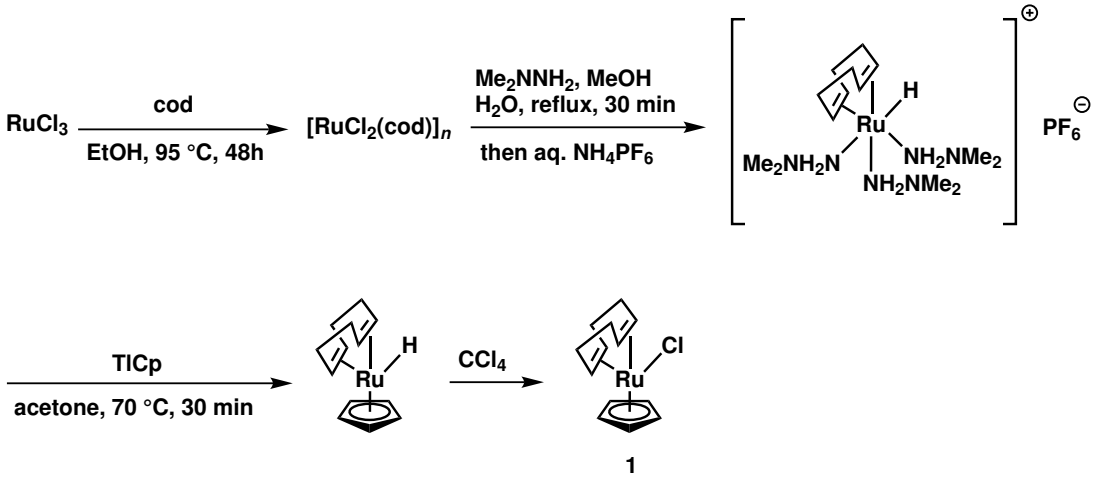

$[RuCl_2(cod)]_n$

A two-neck round bottom flask was flame-dried and purged with N_2. Ruthenium trichloride hydrate ($RuCl_3 \cdot$ x H_2O, 7.4 g, 0.03 mol, 1 eq) was added to the flask. The flask was evacuated and kept under vacuum for 1 h and then was purged with N_2. To the flask were added 1,5-cyclooctadiene (20 mL, 18 g, 0.16 mol, 5 equiv.) and ethanol (0.14 L, c = 0.2 M) to give a dark brown solution. The reaction mixture was stirred and heated at reflux at 95 °C for 48 h and subsequently cooled to 23 °C. The resulting brown precipitate was filtered off through a sintered glass funnel under air, and washed thoroughly with ethanol (50 mL). The brown solid was dried under vacuum for 48 h to afford $[RuCl_2(cod)]_n$ (8.2 g). The material was used in subsequent steps without further purification.

Note: Commercial $RuCl_3 \cdot$ x H_2O has variable water content, the total ruthenium content is 40−43%.

$[(cod)RuH(NH_2NMe_2)_3]PF_6$

To an oven dried 250 mL two-neck round bottom flask equipped with a magnetic stir bar was added $[RuCl_2(cod)]_n$ (5.50 g) under N_2. To the flask were added degassed methanol (55 mL), degassed water (13.8 mL) and freshly distilled degassed N,N-dimethyl hydrazine (55 mL, 43 g, 0.72 mol). The mixture was heated at 95 °C and stirred at the same temperature for 45 min. The resulting mixture was subsequently cooled to 23 °C over 60 min with stirring. Under N_2, to the above reaction mixture was added a degassed solution of NH_4PF_6 (5.5 g, 34 mmol) in H_2O (55 mL). The slurry was kept at −20 °C for 12 h under N_2. The resulting colorless precipitate

was filtered through a sintered glass funnel under air. Then the filtrate was concentrated under reduced pressure to half of the volume and was kept at −20 °C for 60 min. The resulting colorless precipitate was filtered through a sintered glass funnel to afford a second crop of product, which was combined with the previous fraction. The combined colorless precipitate was washed thoroughly with ice-cold water (200 mL) and dried under vacuum for 48 h to afford $[(cod)RuH(NH_2NMe_2)_3]PF_6$ (4.9 g). The material was used in subsequent steps without further purification.

[CpRu(cod)Cl] (3)

Caution: This step involves the use of toxic CpTl reagent. Proper care is essential to safely carry out this reaction, and the appropriate disposal of the thallium-contaminated flask, celite, gloves, needles and other materials is of the utmost importance for the safety of the chemist, staff, and other personnel.

Inside a nitrogen-filled glovebox, a 250 mL two necked round bottom flask equipped with a magnetic stir-bar was charged with $[(cod)RuH(Me_2NNH_2)_3]PF_6$ (5.00 g) and thallium cyclopentadienide (2.78 g, 10.3 mmol). The flask was sealed with a rubber septum and was brought outside the glovebox. Degassed acetone (88 mL) was added to the flask under N_2. The mixture was heated at 65 °C and stirred at the same temperature for 30 min. The resulting mixture was subsequently cooled to 23 °C over 20 min. The mixture was transferred with a cannula into a Schlenck flask, sealed, and brought inside a glovebox (Note: a rubber septum alone can not withstand the pressure difference inside the antechamber and presents a significant spill hazard). The mixture was filtered through a pad of celite under vacuum. The resulting filtrate

was concentrated in vacuo to afford a brown solid. Pentane (30 mL) was added to the brown solid and the mixture was shaken vigorously for 10 min. The resulting mixture was drawn into a syringe and filtered through a 0.2 nm PTFE syringe filter into a separate 50 mL flask containing CCl_4 (1.93 mL). A yellow precipitate was immediately observed. The above sequence of pentane (30 mL) addition to the brown solid was repeated. The supernatant was filtered again and added to the CCl_4 containing flask. The mixture was stirred inside a glove box for 30 min. Then the flask was removed from the glove box, and the mixture was filtered through a sintered glass funnel under air. The resulting solid was washed with pentane (30 mL) and dried under vacuum to afford [CpRu(cod)Cl] (1.21 g, 3.27 mmol, 16 ± 1 % from $RuCl_3$) as a dark yellow solid.

NMR Spectroscopy:

^{1}**H NMR** (500 MHz, $CDCl_3$, 23 °C, δ): 5.32−5.29 (m, 2H), 4.95 (s, 5H), 4.41−4.38 (m, 2H), 2.62−2.59 (m, 2H), 2.10−2.03 (m, 4H), 2.00−1.93 (m, 2H).

^{13}**C NMR** (125 MHz, $CDCl_3$, 23 °C, δ): 128.8, 87.1, 85.9, 78.7, 32.6, 28.1, 28.0.

HRMS (m/z) calc'd for $C_{13}H_{17}ClRu$ $[M\text{-}Cl]^+$, 275.0374; found, 275.0367.

Methyl acetyl-L-tyrosinate (8)

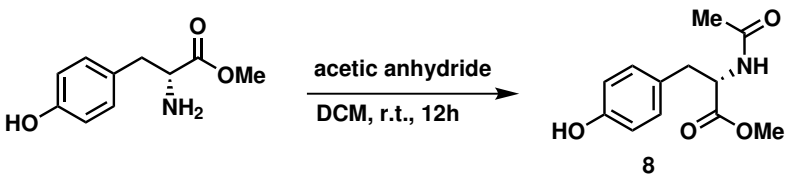

8

Acetic anhydride (50.9 μL, 54.9 mg, 0.538 mmol, 1.05 eq) was added to a solution of L-tyrosine methyl ester (100. mg, 0.513 mmol, 1.00 eq.) in dichloromethane (3 mL, c = 0.2 M) and stirred at room temperature for 12 h. The solvent was removed in vacuo and the product purified by column chromatography. Methyl acetyl−L−tyrosinate (8) was obtained as a colorless solid (102 mg, 0.430 mmol, 84%). $\mathbf{R}_f$ = (hexanes/ethyl acetate 25:75 (v/v)) 0.14

NMR Spectroscopy:

^{1}**H NMR** (600 MHz, $CDCl_3$, 23 °C, δ) 6.93 (d, J = 8.4 Hz, 2H), 6.73 (d, J = 8.4 Hz, 2H), 6.09 (d, J = 7.6 Hz, 1H), 4.86 (dt, J = 7.9, 6.0 Hz, 1H), 3.74 (s, 3H), 3.08 (dd, J = 14.1, 5.6 Hz, 1H), 2.97 (dd, J = 14.1, 6.3 Hz, 1H), 1.98 (s, 3H).

^{13}**C NMR** (126 MHz, $CDCl_3$, 23 °C, δ) 172.2, 170.21, 155.4, 130.1, 126.9, 115.5, 53.3, 52.3, 37.1, 22.9.

HRMS (m/z) calc'd for $C_{12}H_{16}NO_4$ $[M+H]^+$, 238.1079, found: 238.1080.

Fluoro−acetyl−L−tyrosinate 9

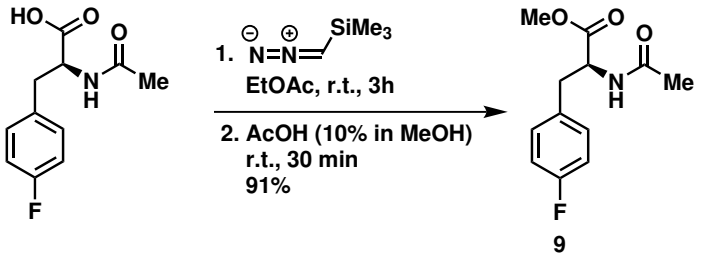

9

To a solution of N−acetyl−fluoro−L−phenylalanine (50. mg, 0.22 mmol, 1.0 eq.) in ethyl acetate (2 mL, c = 0.1 M) was added 0.12 mL trimethylsilyldia-

zomethane (2.0 M in diethyl ether, 0.24 mmol, 1.1 eq.) and stirred at room temperature for 3h. Then, 0.5 mL 10% acetic acid in methanol was added and the reaction mixture was stirred for another 30 min and then concentrated in vacuo. N−acetyl−4−fluoro−L−phenylalanine methyl ester 9 (48 mg, 0.20 mmol, 91%) was obtained as a colorless oil.

$\mathbf{R}_f$ = (hexanes/ethyl acetate 25:75 (v/v)) 0.22

NMR Spectroscopy:

^{1}**H NMR** (600 MHz, $CDCl_3$, 23 °C, δ) 7.04 (dd, J = 8.6, 5.4 Hz, 1H), 6.94 (t, J = 8.7 Hz, 1H), 6.19 (d, J = 7.9 Hz, 1H), 4.81 (dt, J = 7.8, 5.9 Hz, 1H), 3.68 (s, 2H), 3.09 (dd, J = 14.0, 6.0 Hz, 1H), 3.01 (dd, J = 14.0, 5.9 Hz, 1H), 1.95 (s, 2H).

^{13}**C NMR** (126 MHz, $CDCl_3$, 23 °C, δ) 172.0, 169.8, 162.0 (d, J = 245.5 Hz), 131.7, 130.7, 115.4 (d, J = 21.6 Hz), 53.2, 52.3, 37.0, 23.0.

^{19}**F NMR** (471 MHz, $CDCl_3$, 23 °C, δ) −115.7.

HRMS (m/z) calc'd for $C_{12}H_{15}FNO_3$ $[M+H]^+$, : 240.1036, found: 240.1030.

2.3.2 Manual radiosynthesis

Optimization of conditions

Ruthenium-phenol complex formation with [CpRu(cod)Cl] was carried out in EtOH. We found the presence of EtOH also significantly increases the elution efficiency of ^{18}F-fluoride. Therefore, we decided to investigate the effect of EtOH content in the reaction mixture on the radiochemical conversion.

The overall yields for EtOH = 0−30% are in the same range (EE x RCC = 20−30%) and above EtOH% = 30%, EtOH dramatically lowers the overall yield. (Figure 2.5)

The total volume of all reactions in Figure 2.5 is 2 mL. The other solvent mixture is (MeCN:DMSO 1:1). For example for the in 10% EtOH, the reaction was performed in the solvent mixture containing 200 μL EtOH and 1.8 mL (MeCN:DMSO 1:1). For all reactions except 0% EtOH, the elution was performed with only EtOH (but different volumes depending on EtOH percentage), and the remaining solvent (DMSO:MeCN 1:1) added after the elution. Note: for the first entry in the chart (0% EtOH), after the complexation step, EtOH was evaporated and exchanged with MeCN:DMSO (1:1).

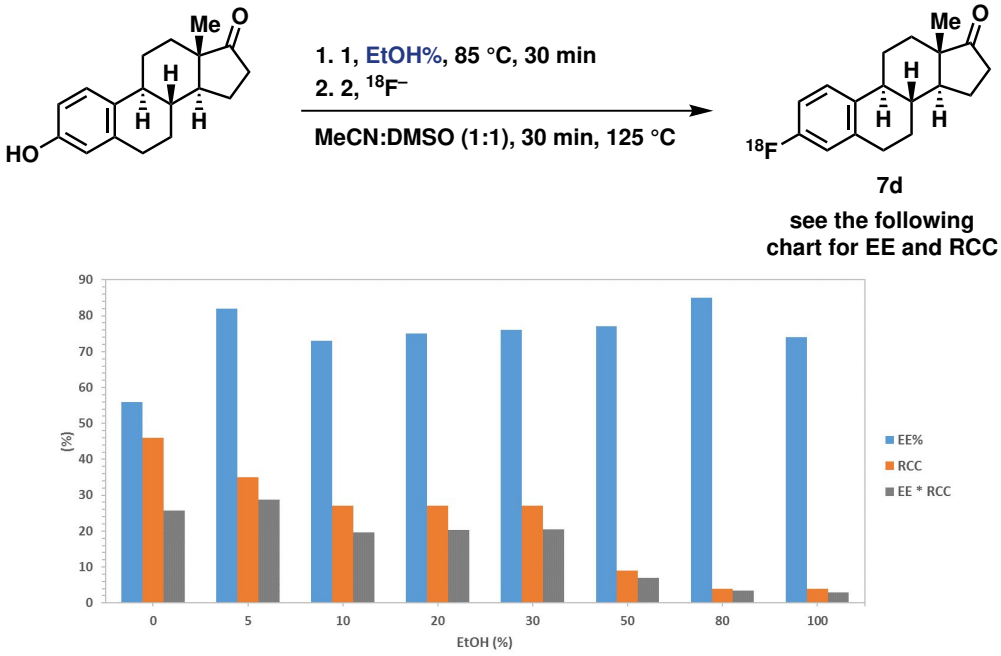

Figure 2.5: Effect of EtOH on the EE, RCC and the overall yield (EE x RCC) on the [^{18}F]deoxyfluorination of estrone

For comparability, the volume of the reaction mixtures mentioned in Figure 2.5 were kept all constant to optimize the ethanol content. However, a reduction of volume from 2 mL to 400 μL, the overall yield from ca. 25% was increased to ca. 45% for the reaction without Ethanol. (Figure 2.5) As extremely low amounts ($<$50 μL) of

ethanol make the elution practically challenging, we reduced our overall volume to 400 μL with 12.5% EtOH.

General procedure for [^{18}F]deoxyfluorination of phenols

A phenol (8.7 μmol, 1.0 eq.) and [CpRu(cod)Cl] (1) (8.0 mg, 2.6 μmol, 3.0 eq.) were added to EtOH (50. μL, c = 0.80 M) in a 0.5 dram (1.8 mL) borosilicate glass vial. The vial was capped, and the reaction mixture was stirred at 85 °C for 30 min. The vial was removed from the hot plate and allowed to stand for 3 min at 23 °C. To the vial, N,N′-bis-(2,6-diisopropylphenyl)chloroimidazolium chloride (2) (12 mg, 26 μmol, 3.0 eq.) and 150 μL of MeCN were added, and the resulting solution mixture was loaded into a 1.0 mL polypropylene syringe. [^{18}F]fluoride solution from the cyclotron (50 μL, 7.1 mCi) was loaded with a syringe onto a QMA anion exchange cartridge (Chromafix 30-PS-HCO_3), and the cartridge was washed with MeCN (1.0 mL). The cartridge was inverted and fitted with a female x female luer adapter. With the syringe, which contained the corresponding solution of phenol-ruthenium complex and 2, the [^{18}F]fluoride was eluted into a 1 dram (3.7 mL) borosilicate vial. The cartridge was washed with DMSO (150 μL), followed by DMSO:MeCN (50 μL, 1:1 (v/v)). The reaction vial, which contained 400 μL of the reaction mixture was sealed with a teflon-lined cap and was heated at 125 °C for 30 min. The vial, which contained the reaction mixture was removed from the heat and was allowed to stand for 3 min at 23 °C. The reaction mixture was analyzed by radio-HPLC and radio-TLC. The products were characterized by comparing the radio-HPLC trace of the crude reaction mixtures with the HPLC UV traces of the authentic reference samples.

All ^{18}F-labeled molecules were characterized by comparing the retention time of the product (γ-trace) in the crude reaction mixture to the retention time of an authentic reference sample. Note: radioactivity chromatographs are offset by 0.15 min on account of the delay introduced by the spatial separation between the diode array detector and the radioactivity detector. Elution Efficiency (EE) was calculated as following:

$$EE = \frac{(activity\ on\ cartridge\ after\ loading\ of\ ^{18}F\ from\ cyclotron)}{(eluted\ activity\ of\ [^{18}F]fluoride\ in\ reaction\ vial)}$$

2.3.3 Automated radiosynthesis

For reactions performed on the Elixys, an adapter was needed to accommodate Wheaton 3 mL v-vials. A cylinder of solid aluminum (diameter 0.60 in, height 0.52 in) was manufactured for that purpose.

Optimization of Synthesis

Influence of vial size and type:

In ethanol (200 μL), methyl acetyl-L-tyrosinate (8) (5.0 mg, 21 μmol, 1.0 eq), [CpRu(cod)Cl] complex 1 (10 mg, 27 μmol, 1.3 eq) and N,N′-bis(2,6-diisopropylphenyl)-2-chloroimidazolium chloride (2) (15 mg, 33 μmol, 1.6 eq) were mixed in a dram vial and heated at 85 °C for 30 min to constitute the eluent. [^{18}F]Fluoride was loaded onto QMA anion exchange cartridge (Chromafix 30-PS-HCO_3), and the cartridge was washed with 1 mL of ethanol to remove water from [^{18}F]fluoride. The cartridge was inverted and fitted with a female x female luer adapter. [^{18}F]fluoride was eluted with the eluent into a dram vial (3 mL Wheaton v-vial, 8 mL Wheaton v-vial). Then, acetonitrile (300 μL)

followed by DMSO (300 μL) were passed through the cartridge and collected into the same vial. The reaction vial was sealed with a teflon-lined cap and heated at 130 °C for 30 min. The reaction was subsequently cooled to room temperature and the radiochemical conversion was determined by radio-TLC. The results are summarized in Figure 2.6.

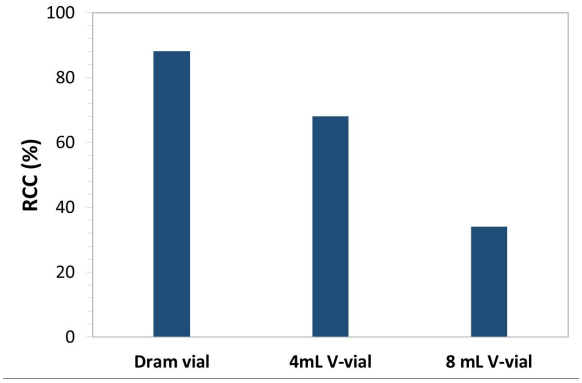

Figure 2.6: Influence of vial size and type on [^{18}F]deoxyfluorination of methyl acetyl-L-tyrosinate.

Influence of pressure:

The precursor solution was prepared by heating methyl acetyl-L-tyrosinate (8) (5.0 mg, 21 μmol, 1.0 eq), [CpRu(COD)Cl] (1) (10 mg, 27 μmol, 1.3 eq), N,N′-bis(2,6-diisopropylphenyl)-2-chloroimidazolium chloride (2) (15 mg, 33 μmol, 1.6 eq)) in ethanol (250 μL, 200 proof) at 85 °C for 30 min and diluting with DMSO (0.4 mL) and acetonitrile (0.4 mL). In a Siemens Explora FDG4, fluoride was captured on a QMA previously conditioned (with 1 mg K_2CO_3 in 1 mL water an subsequently washed with 10 mL water), eluted with Kryptofix solution (2 mL water, 8 mL acetonitrile, 10 mg K_2CO_3, 50 mg $K_{2.2.2}$) and dried azeotropically with acetonitrile (1 mL) three times. The precursor solution was added and heated at a defined pressure (30 kPa or 205 kPa) for 30 min. A sample was taken to determine the radiochemical conversion.

At 30 kPa 4.1% RCC and at 205 kPa 21% RCC were observed.

Automated Radiosynthesis of [^{18}F]-N-acetyl-methyl-(4-fluoro)phenylalanine

Methyl acetyl-L-tyrosinate (5.0 mg, 21 μmol, 1.0 eq), [CpRu(COD)Cl] (1) (7.0 mg, 27 μmol, 1.3 eq), 30 mg *N,N′*-bis(2,6-diisopropylphenyl)-2-chloroimidazolium chloride (2) (65 μmol, 3.1 eq) were heated in 250 μL ethanol (200 proof) at 85 °C for 30 min to constitute the eluent.

On an automated synthesis platform (Elixys, Sofie Biosciences), aqueous [^{18}F]fluoride was trapped on a QMA cartridge and ethanol (1 mL 200 proof) was passed through the cartridge to remove residual water. 461 mCi of F-18 were measured at t = 0. The eluent was used to elute fluoride off the QMA into a 3 mL Wheaton V-vial. 0.8 mL 1:1 DMSO/MeCN were used to flush the piping and collected in the V-vial as well. Remaining on Cartridge: 66.4 mCi (t = 22 min), in reactor (after reaction): 239 mCi (t = 45 min), Elution efficiency, decay corrected, accounting for losses in transfer: 69.0%.

The mixture was stirred at elevated temperature (set-point at 150 °C) for 30 min and subsequently cooled to room temperature. A sample was used to determine the radiochemical conversion by analytical HPLC (69% RCC, Figure 2.7, analytical HPLC on an Eclipse XDB-C18 column (10 x 4.6 mm, 5 μM), by a gradient from 5% MeCN/H_2O/0.1% TFA to 95% MeCN/H_2O/0.1%TFA within 10 min at a flow rate of 2 mL·min^{-1}. The solution was diluted to 2 mL with water and loaded onto a semipreparative HPLC and purified with a Gemini NX-C18 (250 x 10 mm, 5 μm) column with a gradient from 5% MeCN/H_2O/0.1% TFA to 60% MeCN/H_2O/0.1%

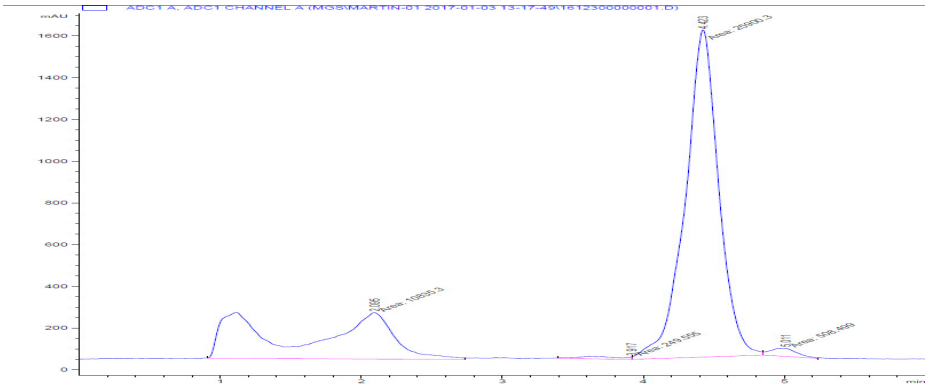

Figure 2.7: Determination of radiochemical conversion; Crude reaction mixture γ-trace, RCC = 69%.

TFA within 45 min, at a flow rate of 3 mL·min^{-1} (Figure 2.8). 111 mCi were isolated (t = 80 min).

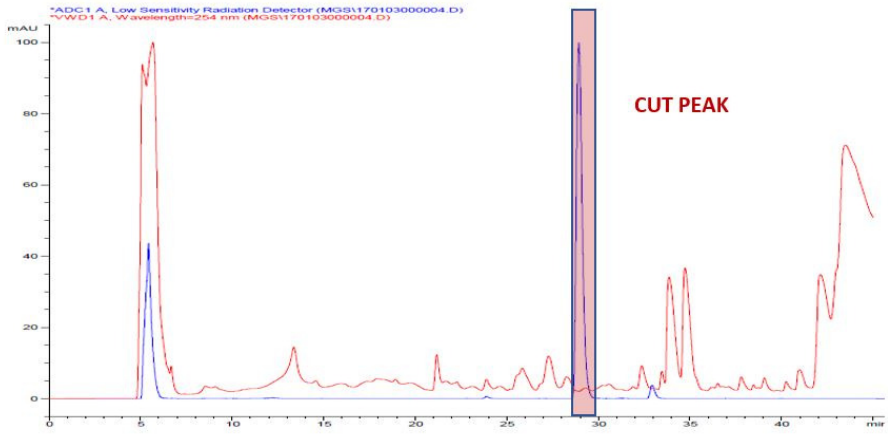

Figure 2.8: Semipreparative HPLC purification; overlay of γ-trace (blue) and UV(254 nm) trace

Isolated radiochemical yield: 24.1 % non-decay corrected (t = 80 min), 40.0 % decay corrected.

The radiochemical identity was confirmed by analytical HPLC on an Eclipse XDB-C18 column (10 x 4.6 mm, 5 μM), by a gradient from 5% MeCN/H_2O/0.1% TFA to

95% MeCN/H_2O/0.1%TFA within 10 min at a flow rate of 2 mL·min^{-1}. (Figure 2.9)

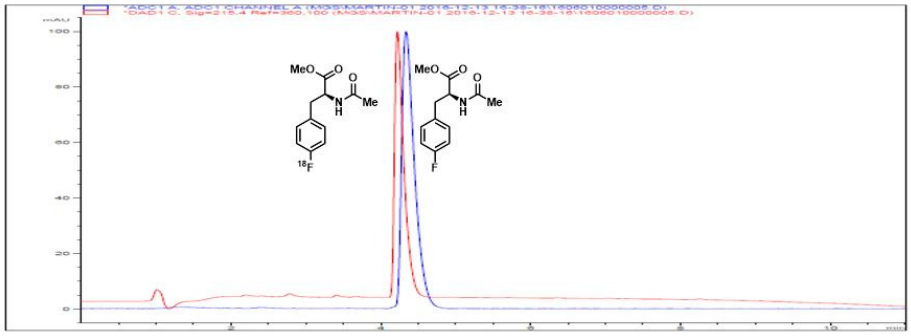

Figure 2.9: Confirmation of radiochemical identity; overlay of γ-trace (blue) and UV (254 nm) trace (red)

Specific activity was determined to be 2.5 mCi·nmol^{-1} (7.84 nmol·mL^{-1} molar concentration in sample by calibration curve, 19.6 mCi·mL^{-1} activity concentration at end of synthesis) (Figure 2.10) via a calibration curve (Figure 2.11) acquired with an authentic standard for N-acetyl-4-fluoro-L-phenylalanine methyl ester, with the same analytical HPLC method as for the confirmation of radiochemical identity and a 30 μL injection per sample.

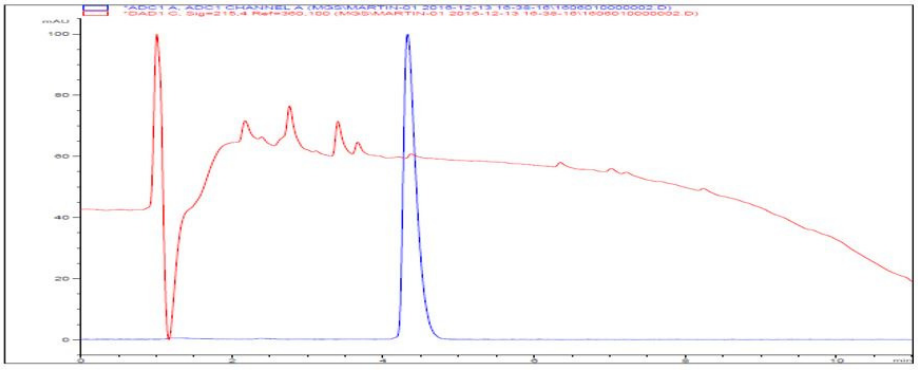

Figure 2.10: Determination of specific activity; Overlay of γ-trace (blue) and UV(215 nm) trace (red) of purified fraction; AUC = 36.05.

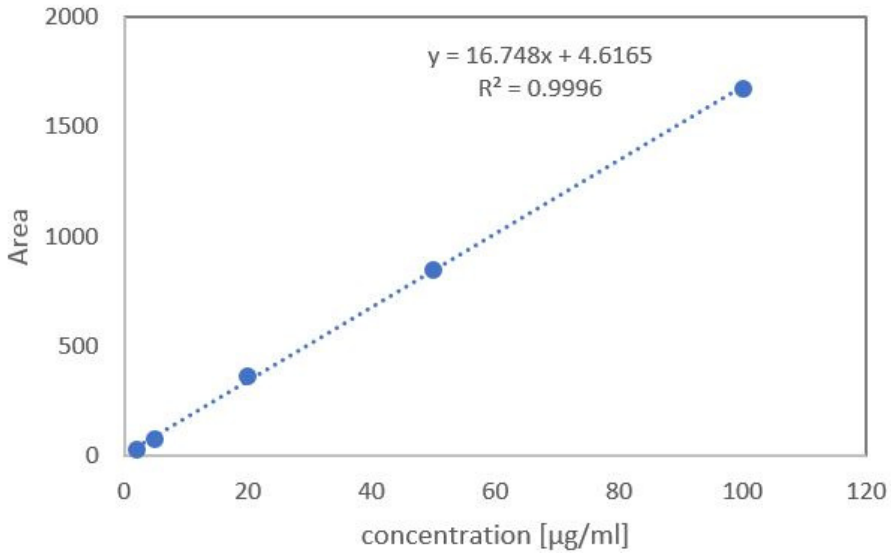

Figure 2.11: Calibration curve acquired with authentic standard at 215 nm (averaged triplicate) for determination of specific activity.

Determination of enantiopurity A racemic standard was analyzed on a Chiralcel AD column (250 x 4.6 mm, 10 μm) with 10% isopropanol in hexanes at a flow rate of 1 ml·min^{-1} and monitored at 254 nm. (R)- and (L)-N-acetyl-4-fluoro-phenylalanine methyl ester separated well under these conditions. Coinjection with a sample of the reaction mixture showed the retention of stereochemical information through the labeling procedure. (Figure 2.12)

Automated radiosynthesis of [^{18}F]-β-CFT (4)

Methyl (1R,5S)-3-(4-hydroxyphenyl)-8-methyl-8-azabicyclo[3.2.1]oct-2-ene-2-carboxylate (3) (5.0 mg, 18 μM, 1.0 eq), [CpRu(COD)Cl] (3) (10 mg, 27 μmol, 1.5 eq), N,N′-bis(2,6-diisopropylphenyl)-2-chloroimidazolium chloride (30 mg, 65 μmol, 3.6 eq) were heated in 250 μL ethanol (200 proof) at 85 °C for 30 min to constitute the eluent. On an automated synthesis platform (Elixys, Sofie Biosciences), aqueous [^{18}F] Fluo-

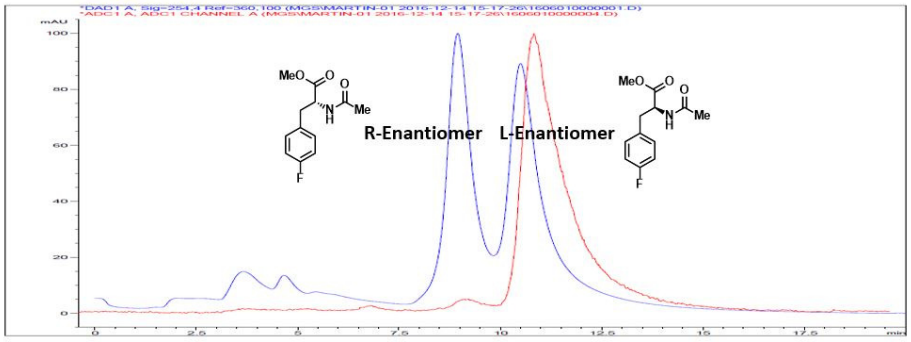

Figure 2.12: Coinjection of racemic N-acetyl-4-fluoro-phenylalanine methyl ester with reaction mixture; ee of labeling product determined >97%; UV(254 nm) trace in blue, γ-trace in red

ride was trapped on a QMA cartridge and 1 mL 200 proof ethanol was passed through the cartridge to remove residual water. 409 mCi were measured at t = 0. The eluent was used to elute fluoride off the QMA into a 3 mL Wheaton V-vial (adapter as specified). In order to flush the pipe, 0.8 mL 1:1 DMSO/MeCN were used and collected in the V-vial as well. Remaining on Cartridge: 28.9 mCi (t = 42 min), in reactor (after reaction): 200 mCi (t = 46 min), Elution efficiency, decay corrected, accounting for losses in transfer: 65.5%

The mixture was stirred at elevated temperature (set-point at 160 °C) for 30 min and subsequently cooled to room temperature. A sample was used to determine the radiochemical conversion by analytical HPLC (73% RCC, determined by analytical HPLC on an Eclipse XDB-C18 column (10x4.6 mm, 5 μM) by a gradient from 5% MeCN/H_2O/0.1% TFA to 95% MeCN/H_2O/0.1%TFA within 10 min at a flow of 2 mL·min^{-1}, Figure 2.13).

An analytical sample was obtained by diluting the crude reaction mixture with water

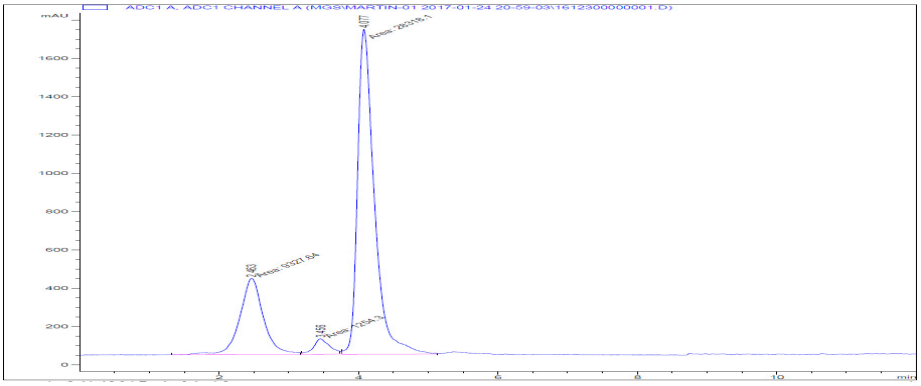

Figure 2.13: Analytical HPLC of reacton mixture to determine radiochemical conversion, γ-trace

to 2 mL and subsequent purification via semipreparative HPLC on a Gemini NX-C18 column (250 x 10 mm, 5 μm) with a gradient from 5% MeCN/H_2O/0.1% TFA to 60% MeCN/H_2O/0.1% TFA within 45 min at 3 mL·min^{-1}. The pure sample was used to confirm the radiochemical identity of the product (Figures 2.14 and 2.15) and for determination of the specific activity with the same analytical HPLC conditions used for the determination of radiochemical conversion. The product has very low UV absorption and the amount of β-CFT in the purified sample was below the detection limit. At the measured radioactivity concentration, the specific activity was determined to be greater than 1.5 Ci·μmol^{-1}.

The majority of the product was not retained on the column and an isolated yield could not be determined. Based on the content of product in the solvent front as determined by HPLC, we estimate that under appropriate purification conditions an isolated yield of ca. 30 % non-decay corrected can be achieved. Based on our experience, we recommend to investigate SPE protocols and subsequent HILIC or normal phase chromatography.

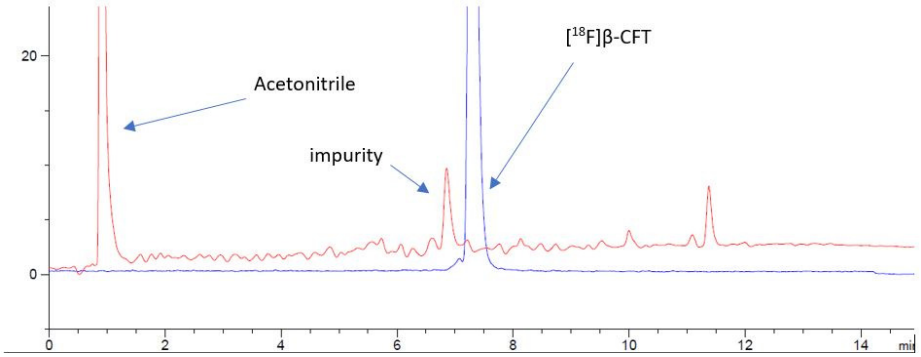

Figure 2.14: HPLC trace of purified analytical sample; UV(210 nm)-trace in red, γ-trace in blue.

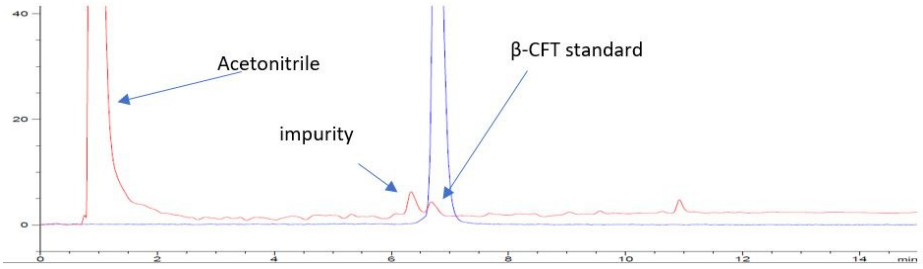

Figure 2.15: HPLC trace of analytical sample with added authentic standard of β-CFT; UV(210 nm)-trace in red, γ-trace in blue.

Chapter 3

Imaging Histone Deacetylases With Positron Emission Tomography

3.1 Development of MGS3

This chapter includes work performed by F. Al Schroeder, Hsiao-Ying Wey, Michael S. Placzek, Changning Wang, Genevieve V. d. Bittner, Ramesh Neelamegam, and was published in *ACS Chemical Neuroscience* **2016**, *7*(5), 528-533. Al Schroeder and Ramesh Neelamegam contributed to the conception of the project, Hsiao-Ying Wey assisted with non-human primate data analysis, Michael Placzek assisted with rodent data analysis and Al Schroeder and Genevieve Van de Bittner assisted with scanner operation and animal care. Non-human primate Martinostat imaging data were acquired by Changning Wang.

3.1.1 Strategic prioritization of candidates

As outlined in Chapter 1.4, both the unreliable radiosynthesis as well as the restrictions imposed by the use of ^{11}C limited the potential of [^{11}C]Martinostat. To develop an ^{18}F analog of [^{11}C]Martinostat, we attempted two distinct strategies: 1) labeling by installation of a fluorine-bearing prosthetic group; or 2) fluorination of the aromatic ring. The first approach is represented by CN146, which contains a fluoroethyl substituent, while the second approach is actualized by the structures MGS1-3, which are labeled on the aromatic ring (Figure 3.1). Ex vivo prioritization of compounds was achieved using a validated functional recombinant HDAC assay to determine the extent to which candidate structures engage HDAC subtypes [150]. As shown in Figure 3.1, installation of a fluoroethyl prosthetic group reduces HDAC affinity drastically. Therefore, we focused our efforts on three leads, MGS1-3.

Initial interrogation of brain uptake of the MGS1-3 series utilizing the existing [^{11}C]Martinostat radiotracer indicated a comparable reduction in [^{11}C]Martinostat uptake in rat following administration of either 1 mg·kg^{-1} of unlabeled [^{19}F]MGS1-3 or unlabeled [^{12}C]Martinostat, providing evidence for brain penetrance and in vivo HDAC engagement of the candidate structures and warranting investments in radiolabeling.

3.1.2 Radiosynthesis of MGS1-3

The radiosynthesis of the MGS series was achieved on the basis of traditional S_NAr chemistry (Figure 3.3). While the labeling and reductive amination of 4-formyl-3-nitrocinnamate (**10**) was successful, apart from MGS3 the conversion of the intermediary ester **12a-c** into the hydroxylamine did not proceed under any attempted

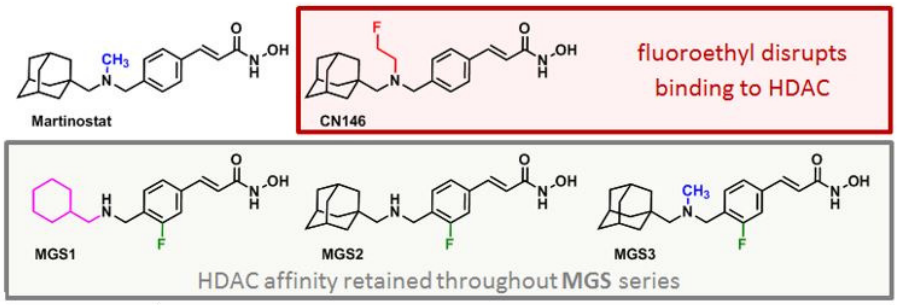

IC50 (nM)	HDAC1	HDAC2	HDAC3	HDAC6	HDAC8
Martinostat	0.3	0.8	0.6	4.1	>15000
CN146	222	651	470	308	>30000
MGS1	1.64	14.2	0.54	11.7	725
MGS2	0.8	6.4	0.5	9.5	>5000
MGS3	0.78	7.0	0.76	11.6	>30000

Figure 3.1: Recombinant HDAC assay, IC_{50} values for candidate molecules to elucidate how structural modifications to [^{12}C]Martinostat impact target engagement. While installation of a fluoroethyl prosthetic group disrupts HDAC binding, the target affinity is retained throughout the MGS series.

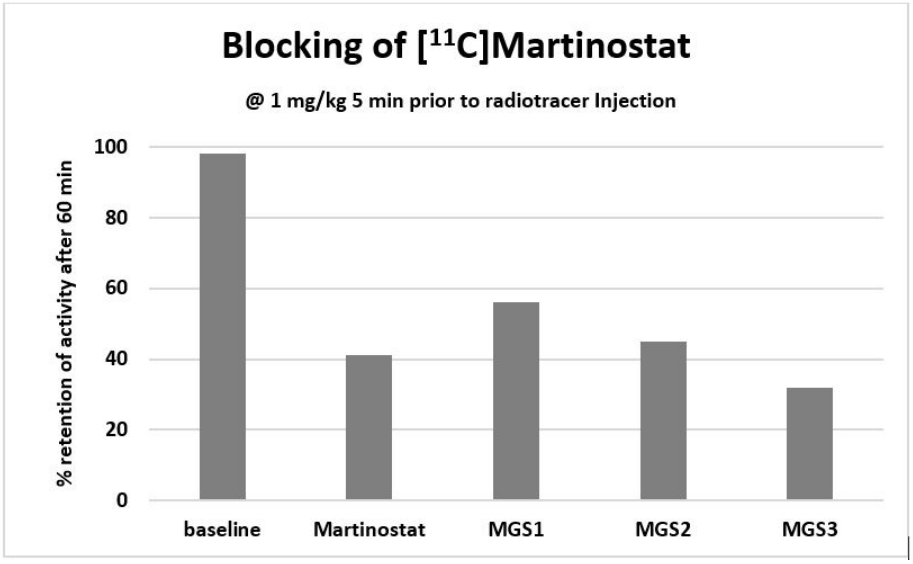

Figure 3.2: [^{11}C]Martinostat blocking experiments confirm brain penetrance of the MGS series

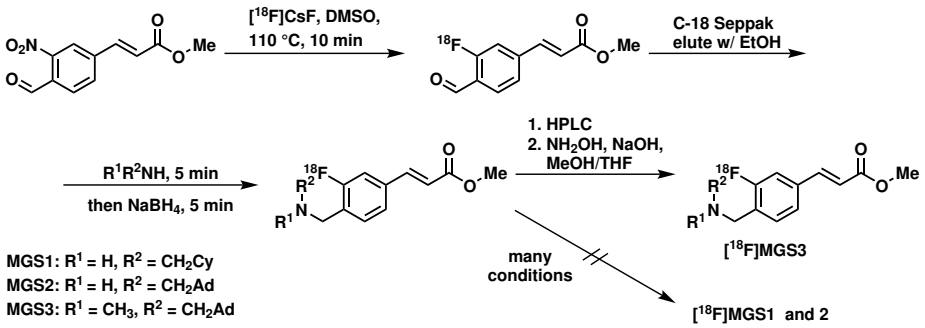

Figure 3.3: Radiosynthesis of [^{18}F]MGS3 and initial attempted route to synthesize [^{18}F]MGS1-2

conditions.

A different protecting group strategy resolved these issues: The use of a 3,3-dimethyldioxazole protecting group for the hydroxamate in compound **16** was compatible with the fluorination and reductive amination. It was synthesized in 5 steps from 2-nitro-4-bromobenzaldehyde (**13**) (Figure 3.4.

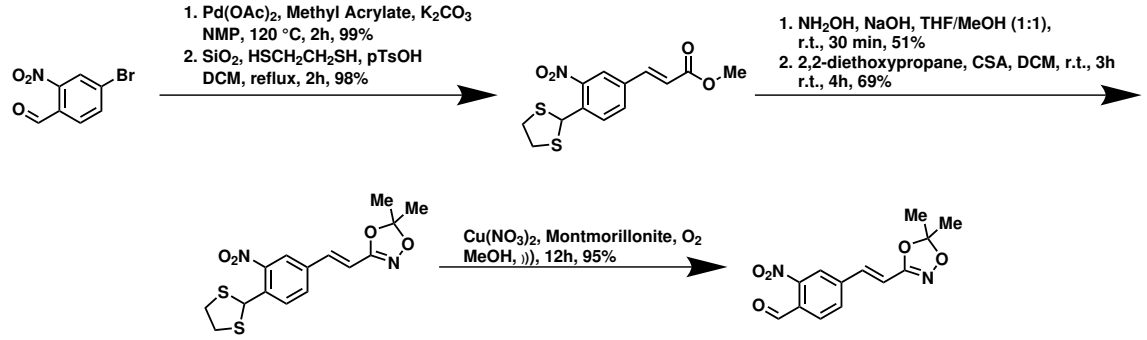

Figure 3.4: Synthesis of labeling precursor for [^{18}F]MGS1-2

Deprotection of the hydroxamate in radiochemistry proved difficult under the same conditions that effected the transformation on traditional organic chemistry scale. Gratifyingly, we found that increasing the concentration of the intermediate by addition of carrier **19** resolved these problems and we were able to synthesize [^{18}F]MGS1 and 2 (Figure 3.5). In order to preserve the high specific activity, the structurally

truncated dimethyldioxazole **20** was employed which was separable from the radiotracer by HPLC.

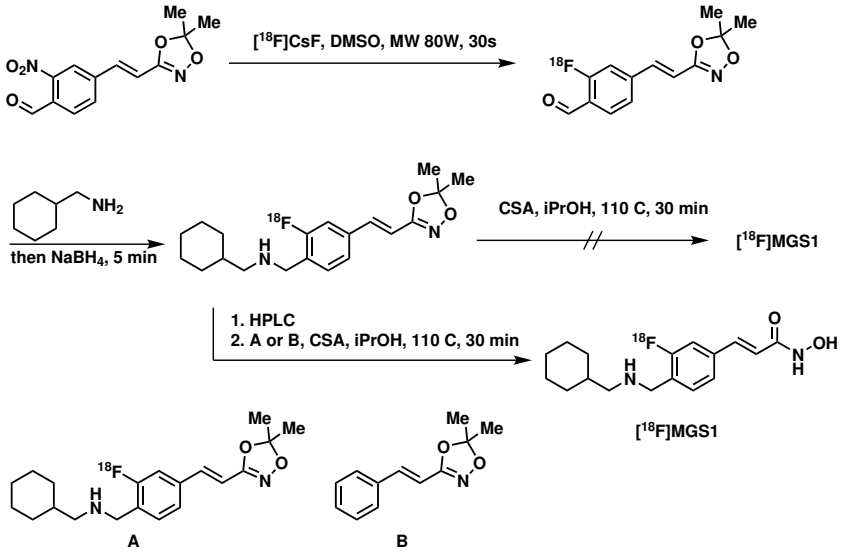

Figure 3.5: Radiosynthesis of [^{18}F]MGS1 with addition of carrier

3.1.3 Rodent PET-CT

To verify in vivo specific, saturable binding of the three candidate structures, MGS1-3, to HDAC, we radiolabeled each compound with ^{18}F. Although yields were generally low (see Experimental, section 3.4.2), we obtained sufficient amounts in high specific activity to conduct dynamic PET/CT imaging in rodents. The time-activity curves of a whole-brain volume of interest (VOI) at baseline were compared to intravenous pre-treatment with 1 mg·kg^{-1} of unlabeled, [^{12}C]Martinostat immediately prior to radiotracer injection. As shown in Figure 3.6, all ^{18}F tracers showed similar baseline TAC profiles, including a rapid increase in whole brain activity with peak activity around 10 min post injection, and limited washout over the 2 h scan inter-

val. Consistent with saturable in vivo binding, pre-treatment with a brain-penetrant HDAC inhibitor increases the rate of [^{18}F]MGS1-3 washout, resulting in a 40-50% reduction in [^{18}F]MGS1-3 compared to peak activity within two hours (Figure 3.6. This observation indicates in vivo HDAC engagement of MGS1-3 signal in rodents is predominantly due to saturable, and hence specific binding to their respective targets.

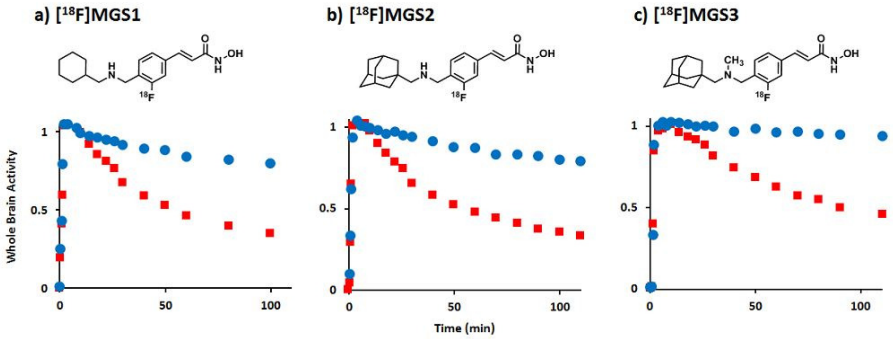

Figure 3.6: PET-CT Imaging of [^{18}F]MGS1-3 in rat. Graphs show tracer uptake in brain at baseline and after pre-treatment with [^{12}C]Martinostat (1mg·kg^{-1}). Robust blocking was observed for all three tracers: a) [^{18}F]MGS1, b) [^{18}F]MGS2 and c) [^{18}F]MGS3. Time-activity curves for whole brain VOI (baseline: blue, blocking: red) confirm high specific/non-specific binding ratio for all three molecules, as the retained activity after two hours is markedly reduced by administration of a blocking agent

3.1.4 Non-human primate imaging

To determine the degree to which specific structural changes of tracer molecules impact brain penetrance and in vivo distribution, as well as for validation of the compounds in a higher species, we advanced MGS1-3 to nonhuman primates. Dynamic PET/MRI imaging in baboon (*Papio anubis*) revealed differences between the labelled molecules in greater detail. Brain images of [^{18}F]MGS1-3 standardized uptake value (SUV), summed over 30-60 min post-radiotracer injection, are shown in com-

Table 3.1: Physical properties and Standard uptake values of MGS-series.

Radiotracer	**[^{18}F]MGS1**	**[^{18}F]MGS2**	**[^{18}F]MGS3**
SUV, baboon	0.566	1.22	1.80
cLogP	3.07	3.77	4.17
TPSA	61.35	61.35	52.56

parison to [^{11}C]Martinostat in Figure 3.7. All three tracers penetrate the blood brain barrier, but the overall SUV greatly varies across the substitution patterns, indicated by the grey bar next to the images. While MGS3 reaches about 78% of the uptake of [^{11}C]Martinostat, seemingly minor structural changes have a detrimental influence on the uptake properties. Formal removal of the methyl group on the amine, as shown by MGS2, results in only about 52% of the uptake of [^{11}C]Martinostat, which is equivalent to an additional 33% reduction of brain uptake with compared to MGS3. Even more strikingly, substitution of the adamantyl substituent for cyclohexyl results in an SUV of 0.56, a 69% decrease compared to MGS3. In Figure 3.8, the whole-brain time-activity curves are shown which

Brain penetrance often correlates to specific physical properties of molecules within a series (Table 3.1), such as their distribution coefficient (LogP) or total polar surface area (TPSA) [167]. In the case of [^{18}F]MGS1-3, it is true that with a higher computed LogP (cLogP) [168, 169], brain penetrance increases. The cLogP of MGS1-3 (3.07, 3.77, 4.17 respectively) correlate linearly ($R^2 = 0.99$) with the SUV. In comparison, the TPSA values of 61.35 for both MGS1 and 2, and 52.56 for [^{18}F]MGS3 do not seem to correlate well with the observed behavior. It has previously been suggested

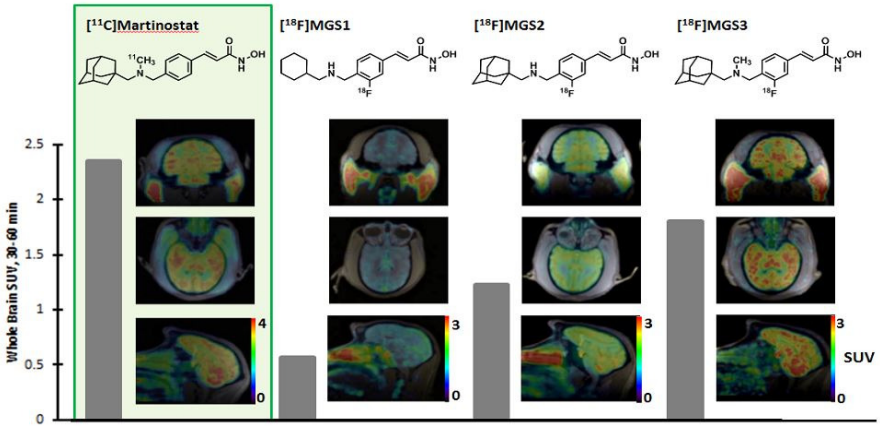

Figure 3.7: Whole brain radiotracer uptake in NHP. Images show the distribution of [^{11}C]Martinostat as well as [^{18}F]MGS1-3 in baboon brain in three planes each. The images are shown in subject space. The respective whole brain SUV 30-60 minutes are quantified for each tracer by the grey bar.

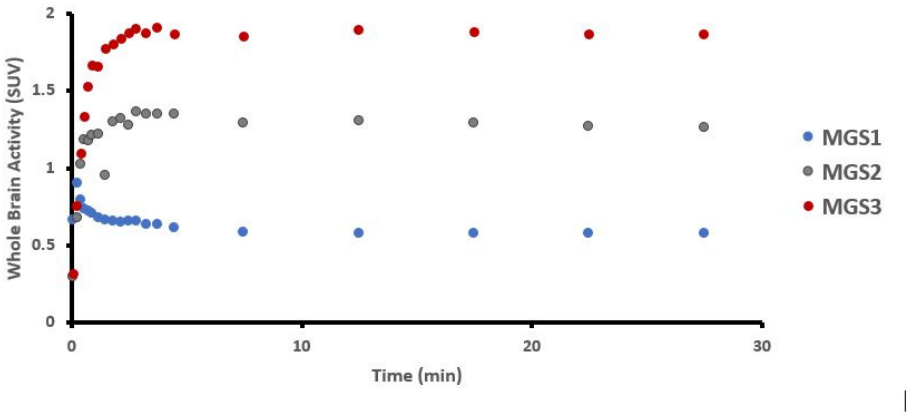

Figure 3.8: Whole brain time activity curves of [^{18}F]MGS1-3 in baboon

that the high brain penetrance of adamantyl bearing structures can be explained by an increased lipophilicity, with a rigid and constricted atomic configuration compared to linear alkanes, which typically leads to undesirable nonspecific binding [170]. Our findings are consistent with that hypothesis. Apart from the adamantyl substituent, another factor we were specifically interested in was the influence of amine methylation on brain uptake, which was tested through comparison of MGS2 and MGS3. Formal removal of a methyl group from the parent structure is estimated to decrease the pK_A by roughly one unit. However, at physiological pH, this change is not expected to alter the protonation state significantly, since pK_A values of secondary and tertiary acyclic aliphatic amines are typically greater than 9 [171]. The influence on the cLogP and, ultimately, the SUV is nonetheless profound, as described above. The effect of methylation on brain uptake within the MGS-series is therefore merely based on overall polarity.

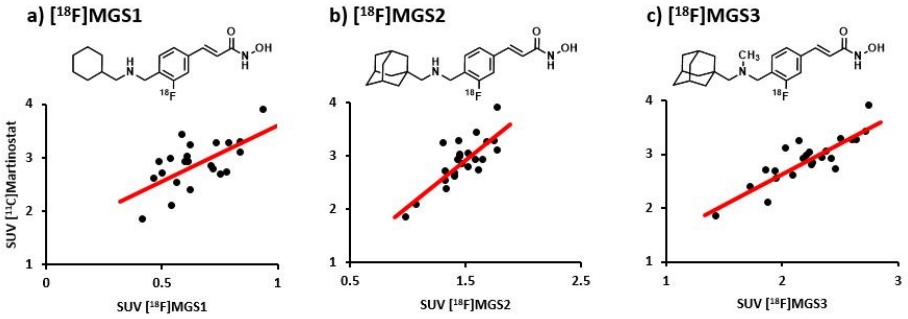

Figure 3.9: Regional correlation between distributions of different tracers a) Regional correlation analysis between [^{11}C]Martinostat and [^{18}F]MGS1 averaged 30-60 min after TOI, Spearman r = 0.64, R^2=0.41; b) [^{11}C]Martinostat and [^{18}F]MGS2 averaged 30-60 min after TOI, Spearman r = 0.79, R^2=0.63; c) [^{11}C]Martinostat and [^{18}F]MGS3 averaged 30-60 min post injection, Spearman r = 0.86, R^2=0.73;

Beyond brain uptake, the regional tracer distribution was assessed to determine the

suitability of a candidate ^{18}F tracer as an analog for [^{11}C]Martinostat. To compare regional distribution, images for each tracer were coregistered to the Black baboon atlas [172], 38 ROIs were chosen and symmetrical regions averaged. The regional SUV values for [^{18}F]MGS1-3 were determined and compared to [^{11}C]Martinostat (Figure 3.9, Table 3.2). While for [^{18}F]MGS1, the correlation is relatively poor (but still significant, Spearman r = 0.64, P = 0.005), correlation increases across the series to [^{18}F]MGS3 (Spearman r = 0.86, P = 3.5 x 10^{-6}). This degree of correlation strongly suggests a high specific binding component as well as engagement of the same targets as [^{11}C]Martinostat.

The results presented here are limited by several consequences of the inefficient radiochemistry. Poor yields and the manual synthesis only allowed for low doses to be administered. Full validation of [^{18}F]MGS3, including blocking experiments in baboons, rigorous kinetic quantification using an arterial input function and automated production for human use will require a more efficient synthesis, which is currently under investigation. Our laboratory is investigating the detailed contributions of HDAC subtypes in different tissues to the overall signal.

3.1.5 Conclusion

We developed a series of new ^{18}F-labeled radiotracers for measuring HDAC occupancy in the central nervous system. It was found that within the examined series, the major driving force for brain uptake could be attributed to an adamantyl substituent. Additionally, it was determined that methylation of an amine moiety also drastically increases SUV, overall affording the desired replacement for [^{11}C]Martinostat.

[^{18}F]MGS3 exhibits specific binding, as well as comparable brain uptake and regional distribution to [^{11}C]Martinostat, which warrants further investigation of more efficient radiosyntheses to facilitate full imaging validation and enable use in human subjects.

3.2 Translational efforts toward human neuroimaging with [^{18}F]MGS3

The methods employed to synthesize [^{18}F]MGS3 on an investigational scale are not practical for routine human radiopharmaceutical production. Non-metal-assisted deoxyfluorination of a phenol was unsuccessful, the synthesis of iodinium ylids was hampered by decomposition during attempts to prepare the labeling precursor and the boronic ester necessary to attempt copper-mediated fluorination was not obtained in diverse synthetic attempts. As discussed in Chapter 2, the coordination of Ruthenium in an η^6-fashion extended the substrate scope of deoxyfluorination with imidazolium reagents. We were pleased to find that the method was applicable to MGS3 and furnished the ester-intermediate in $> 90\%$ yield in manual experiments.

For regulatory and dosimetric purposes, the synthesis of radiopharmaceuticals for human imaging needs to be fully automated and well documented and controlled. The process needs to be carried out by staff which typically does not have a strong background in organic or organometallic chemistry in a cGMP environment with stringent quality control requirements. The goal was to implement a radiopharmaceutical production process for [^{18}F]MGS3 at the Martinos Center of Massachusetts General Hospital. Reaction optimization was carried out on an Elixys (Sofie Biosystems), and the technology was ultimately transferred to a Siemens Explora GN/FDG4 radiosynthesis module which is designated for human radiopharmaceutical production.

3.2.1 Reaction optimization on a Sofie Elixys radiosynthesizer

As described in Chapter 2, generally higher amounts of reagents were necessary to obtain acceptable yields under automated conditions due to losses in reagent transfer and different dimensions of the reaction environment. The eluent was prepared by heating 5 mg phenol precursor, 30 mg chloroimidazolium chloride and 10 mg CpRu(COD)Cl in 400 μL ethanol for 30 minutes at 85 °C. With the hardware adjustments discussed in Chapter 2, we were able to obtain up to 90% radiochemical conversion in the first step of the reaction. Roughly 20% of initial activity was converted into the final product over two steps.

3.2.2 Technology transfer to Siemens Explora FDG4

With the conditions optimized on the Sofie Elixys we faced challenges in technology transfer to the Explora with respect to the elution process. Using the dedicated elution line was not an option due to the risk of cross-contaminating other radiopharmaceuticals produced on the same unit with ruthenium and reagents not controlled in respective processes.

We established that elution with $K_{2.2.2}$ and potassium carbonate or bicarbonate, followed by azeotropic dry-down with acetonitrile was compatible with the first step of the sequence, but diminished the yield of the conversion of ester to hydroxamate. Reducing the amount of base used for elution did not restore the desired reactivity. As a consequence, the traditional dry-down approach had to be abandoned.

A six-port/two-position valve was installed such that the position of the QMA can

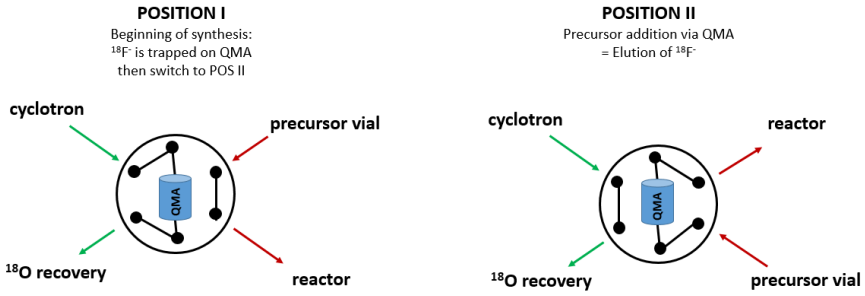

Figure 3.10: Switching valve for elution of [^{18}F]fluoride for synthesis on Siemens Explora GN/FDG4

be switched between the cyclotron/^{18}F-trapping line and the precursor line used for addition of the ruthenium complex (Figure 3.10). In that way, the reaction mixture at no point contaminates any reagent lines other than the precursor line and cross-contaminations are eliminated. The final recipe begins with trapping of ^{18}F on an anion exchange cartridge with the QMA-valve in position A, then a switch into position B and addition of the precursor solution via the QMA, effectively eluting ^{18}F into the reactor. The fluorination proceeds while heating the reaction mixture to 125 °C (IR Feedback, Set point 135 °C) for 30 min at an initial pressure of 205 kPA. The radiochemical conversion of the first step is 52% by analytical HPLC. After cooling to 35 °C, 1.5 mL of a hydroxylamine solution is added for five minutes and diluted with water before purification.

Purification of [^{18}F]MGS3 with SPE and HPLC

The requirements for human radiopharmaceutical doses are stringent. The mass limit for injection of tracer is 0.5 μg per dose, the limit for unknown impurities 0.1 μg per

dose. The ruthenium content has to be below 1ppm and limits are enforced for acetonitrile, DMSO, methanol, THF and other organic solvents. Consequently, a robust purification strategy is essential when designing a production process for radiopharmaceuticals. [^{18}F]MGS3, when produced as described above, is obtained in a complex mixture of numerous organic impurities. The volume at the end of the reaction is almost 2 mL before the addition of water, which is too high for effective HPLC purification, especially with respect to the high organic solvent content of the reaction mixture. It is therefore almost inevitable to perform a pre-purification step to remove most of the organic solvent, hydroxylamine and ruthenium, which can lead to complications with silica-based stationary phases in HPLC.

OASIS MAX is a mixed-phase anion exchange SPE, which showed good selectivity for MGS3 and high recovery of material upon elution. The retention and elution were highly pH-dependent and it was determined that a pH of less than 5 was optimal for elution of product, while trapping was best at a pH >8. After synthesis, the reaction mixture is diluted with only 2 mL of water, because higher amounts cause the urea byproduct of the chloroimidazolium hydrolysis to precipitate, which leads to clogging of the cartridge. The cartridge is then washed with water and eluted with 1.5 mL of a 1:1 mixture of ethanol and 0.1M acetic acid. It was crucial to pre-purify with OASIS MAX SPE systems because bulk organic impurities were detrimental for reverse phase purification, and under HILIC conditions the water content was too high and no retention was achieved. Under HILIC conditions, good peak shapes and separation from the precursor could be achieved, the low polarity of the analyte made it difficult however to achieve resolution from numerous other impurities(Figure 3.11).

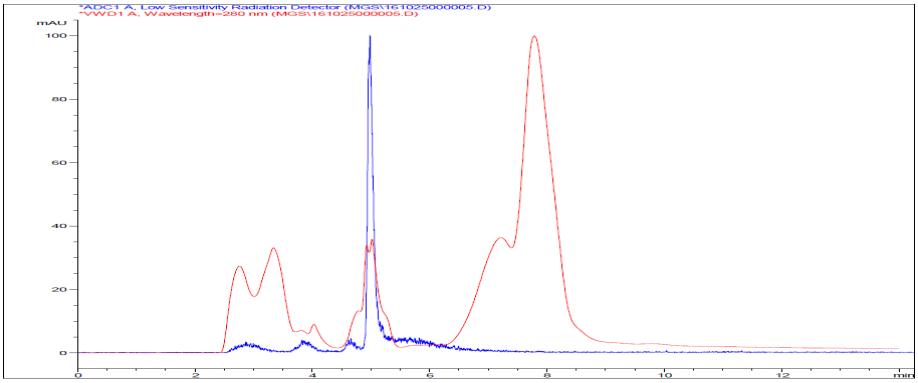

Figure 3.11: Semipreparative HPLC UV(254) trace under HILIC conditions

It was found that separation of [^{18}F]MGS3 from the non-fluorinated phenolic hydroxamate under acidic or neutral conditions was not possible with reverse phase HPLC on any phase available to us at the time. (CN, C-18, C-8, PFP, Phenyl, Phenylhexyl, Hypercarb, Amino, ...) The two compounds showed virtually identical reaction times with alcoholic or acetonitrile organic solvents in the presence or absence of TFA and formic acid. However, under basic conditions separation could be achieved on classic C-18 phases with both ethanol and acetonitrile as organic phases. The use of sodium hydroxide as an additive in the mobile phase was problematic for most conventional column materials, and specifically base-stable materials had to be used to preserve column longevity. The purification was optimized on a Phenomenex Gemini NX-C18 semipreparative column (250 x 10 mm, 5μm) for direct-cut product isolation. High base concentrations lead to hydrolysis of the product (Figure 3.12), while enough base is needed to assure good peak shapes and separation from precursor-derived hydroxamate.

Further, it was important to keep storage buffers consistent. In Figure 3.13, the

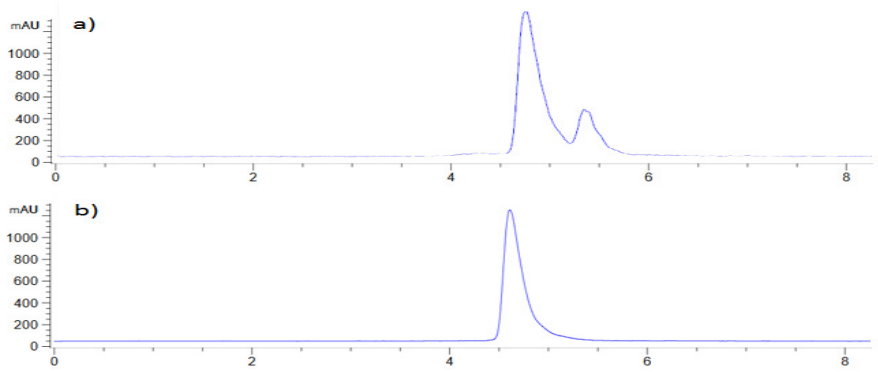

Figure 3.12: Influence of basicity of mobile phase a) with 5 mM NaOH, the product is unstable towards hydrolysis in solution, and the formation of carboxylate can be observed; b) with 4 mM NaOH, a clean γ-trace was achieved.

difference between a run after the colum was stored in mobile phase compared to storage over 50% ethanol is shown.

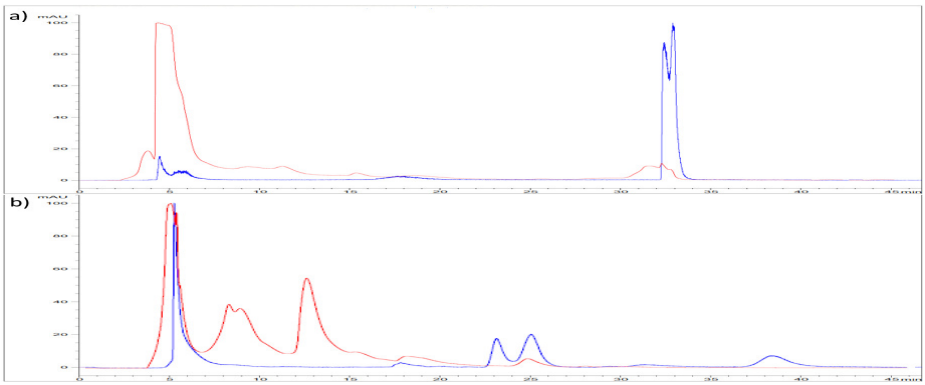

Figure 3.13: semipreparative purification of [^{18}F]MGS3 after SPE pre-purification γ-traces in blue, UV(254 nm) in red; a) Gemini NX-C18 stored over mobile phase (52% EtOH, 4 mM NaOH), run with 3 mL·min^{-1}; b) Gemini NX-C18 stored over 50% ethanol, purification with 40% EtOH, 4 mM NaOH at 3 mL·min^{-1}.

The final mobile phase consists of 40% ethanol (200 proof) with an overall NaOH content of 0.4 mM, and the column is stored over 50% ethanol.

Impurities have to be tightly controlled before doses can be released for human in-

jection. The process to synthesize [^{18}F]MGS3 utilizes some problematic compounds which have to be controlled for beyond HPLC and GC analysis for UV-absorbing impurities and trace solvents.

The ruthenium content is limited to 1 ppm for injectable doses. ICP measurements early in purification development have shown that the Ruthenium content is around 0.1 ppm in the final formulated dose. The ruthenium content will need to be re-assessed during validation, but is not expected to be problematic. Thallium was not detectable in any analyzed samples of formulated product.

Hydroxylamine is a genotoxic impurity and thereby limited to 120 μg daily for studies with a duration below 14 days. Derivatization to acetone oxime and GC analysis is neither very sensitive nor practical for routine QC. An alternative method is the derivatization with FmocCl [173]. Down to single digit mg·mL^{-1} concentrations can easily be detected with analytical HPLC using this approach (Figure 3.14).

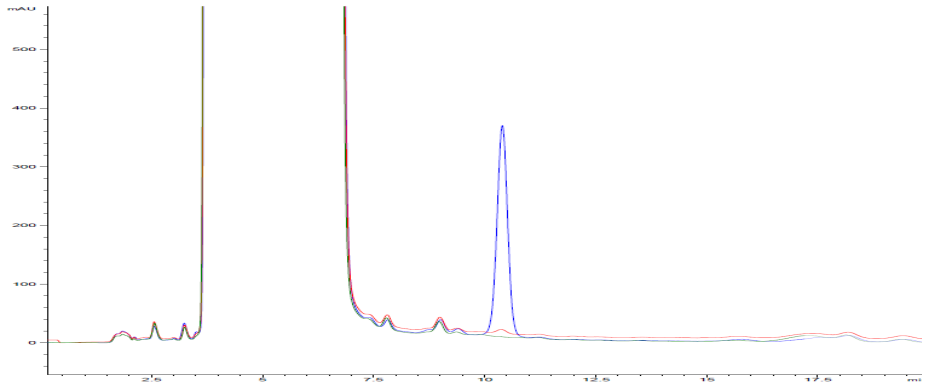

Figure 3.14: Detection of hydroxylamine through derivatization with FmocCl and HPLC over a PFP-phase with buffered methanol/water at 265 nm

In conclusion, a process for the production of human injection grade [^{18}F]MGS was developed. The tracer can be synthesized fully automated on a Siemens GN/FDG4 platform with easily installed custom valves, and assays for all problematic impurities

have been worked out. The purification protocol includes a mixed-phase anion exchange SPE pre-purification, followed by reverse-phase HPLC under basic conditions.

3.3 Biochemical investigation of targets of Martinostat and MGS3

When new radiotracers (or other tool-compounds) are developed, IC_{50}-values acquired *in vitro* with recombinant enzymes are typically used to establish target engagement and quantify selectivity. Needless to say, several layers of complexity intrinsic to any biological system are completely ignored with this approach: Many proteins behave differently in the presence of cellular binding partners, and selectivity can only be determined between molecules that are actively measured, introducing bias. However, it is impractical or even impossible at this time to employ more holistic methods to characterize a more accurate profile of protein targets small molecules interact with. In this section, attempts are made to gain a more detailed understanding of the actual binding events that occur between Martinostat/MGS3 and their *in vivo* protein targets.

3.3.1 Isoform selectivity determined by Cellular Thermal Shift Assays (CETSA)

On a very fundamental level, traditional recombinant enzyme inhibiton assays ignore that most proteins function as part of a regulary complex environment, particularly HDACs. To determine whether the findings from recombinant assays hold true in the human brain, and to evaluate the similarity of [^{18}F]MGS3 and [^{11}C]Martinostat, the engagement of different HDAC isoforms in tissue was compared using CETSA. Figure 3.15 shows hypothetical melting curves of a protein in the presence and ab-

sence of a small molecule binder. The temperature difference ΔT_m is the result of thermodynamic stabilization of the tertiary structure of the protein through the interactions with the small molecule inhibitor, which leads to a higher melting point of the protein. Since denatured proteins are typically insoluble, the intensity of a band obtained through western blotting corresponding to the protein of interest corresponds to the amount of soluble, non-denatured protein and increases with a higher fraction of small-molecule bounds protein. While quantitative statements about the interactions are difficult to derive from CETSA, it confers the advantage of taking into account all the protein-protein interactions in the lysate which can affect the binding of small molecules to the protein. Furthermore, the proteins are not recombinant but rater directly derived from the species of interest. Two distinct approaches can be chosen to obtain information about the thermal stabilization of target proteins:

1. The temperature can be varied at a constant concentration of small molecule and the denaturation curves compared to obtain ΔT_m (Figure 3.15) or
2. Variable concentrations of a compound can be present at a temperature close to the melting point to quantify the relative thermal stabilization of a protein by a given concentration of small molecule binder.

The second approach can give additional information about the relative affinity toward several proteins relative to one another. Since we were trying to understand the molecular target of [^{18}F]MGS3 and [^{11}C]Martinostat, which are only present at very low doses in imaging experiments, we opted for the latter approach to rank the likely engagement with several targets.

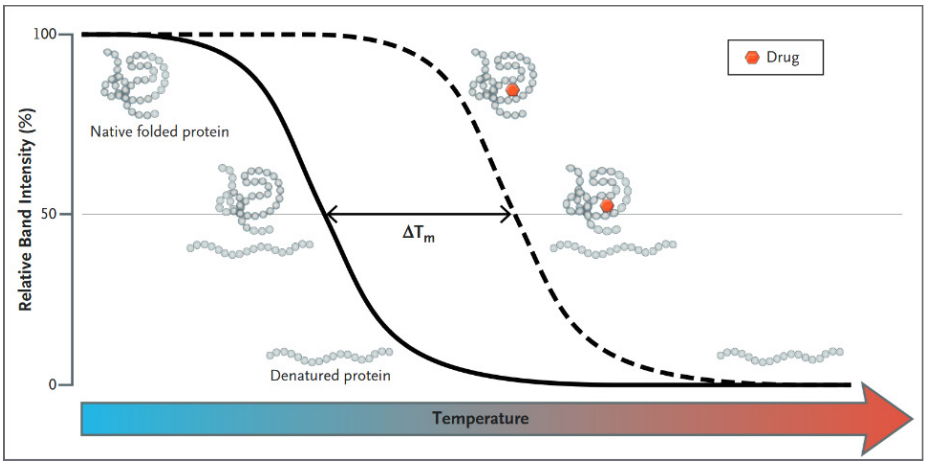

Figure 3.15: schematic depiction [174] of the principle behind CETSA: binding of small molecules increases the melting point of proteins

MGS3 [µM]	HDAC 1	HDAC2	HDAC3	HDAC6	HDAC8
0.16	2	9	0	0	3
0.8	11	40	9	0	0
4	35	34	16	0	0
20	52	43	35	0	0
100	72	64	58	0	2

Mstat [µM]	HDAC1	HDAC2	HDAC3	HDAC6	HDAC8
0.16	5	10	12	2	4
0.8	29	40	29	0	7
4	54	62	27	1	8
20	69	82	28	0	2
100	87	81	35	2	5

Figure 3.16: Cellular Thermal Shift Assays (CETSA) to clarify target engagement of MGS3 and Martinostat in human DLPFC lysate, relative thermal stabilization of HDAC isoforms by MGS3 and Martinostat

As shown in Figure 3.16, the relative thermal stabilization of the investigated HDAC isoforms by both MGS3 and Martinostat is remarkably similar. These data suggest that the distribution observed in imaging should be equivalent for both tracers. However, the complete absence of HDAC6 engagement is to be judged with caution: Proteins with high molecular weights receive less overall thermal stabilization through association with small molecules relative to the free energy necessary for denaturation. Consequently, CETSA is not necessarily applicable to heavy proteins and HDAC6 with a molecular weight of 134 kDa might not be a suitable enzyme to study with this technique. A further confounding factor of target identification with CETSA is the intrinsic bias, as the assay needs to be optimized for any given enzyme and tissue. Therefore, the assay is unable to give information about unexpected or unknown targets.

3.3.2 Unbiased chemoproteomics to identify targets of Martinostat

No battery of inhibition assays can comprehensively determine the targets of a small molecule *in vivo*. In an attempt to clarify the contributions of different isoforms of HDAC, but also other potential targets, to the overall PET signal of [^{11}C]Martinostat more comprehensively, an unbiased mass-spectrometry approach was chosen. In addition to information obtained by CETSA, the selectivity of Martinostat for certain HDAC complexes can conceivably be unraveled by such an approach as well through identification of co-precipitated complex members.

Synthesis of a hydroxamate functionalized solid phase

The basis of this chemoproteomic approach was a solid phase functionalized with a Martinostat-like molecule. With the use of mass spectrometry, differences in the protein profile enriched by the matrix in the presence and absence of Martinostat can be detected and give information about the proteins that Martinostat engages with, and proteins that bind to these targets. Different strategies exist in the design of such solid phases and two options were compared:

1. Covalently linked Martinostat-like functionalization of NHS-ester beads

2. Non-covalent functionalization of beads through biotinylation of a Martinostat-like molecule and streptavidin-linked beads.

The first strategy proved problematic due to high amounts of non-specific binding to the beads in the absence of any functionalization. This observation can be explained by low amounts of hydrolyzed NHS-ester, yielding free carboxylates which are HDAC-binders, therefore enriching HDACs even in the absence of hydroxamate-functionalization. An indicator that this mechanism might be causative for the non-specific enrichment of HDAC2 observed with NHS-functionalized beads it the ability of free Martinostat to reduce binding to the beads. Consequently, the work was continued with a streptavidin-functionalized solid phase.

Three biotinylated hydroxamates were examined for their ability to enrich HDACs. (Figure 3.17) It was found that in the absence of a PEG-linker, no enrichment of HDACs could be achieved. Between PEG-4 and PEG-12 linkers, no major difference was observed in the ability of the compound to enrich HDAC2. For synthetic simplicity, the work was continued with PEG-4.

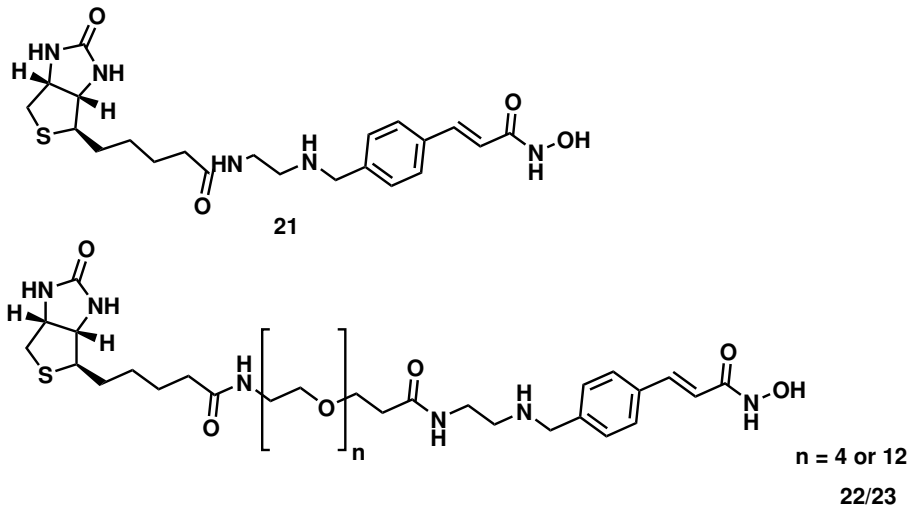

Figure 3.17: Biotin-tagged hydroxamate probes for functionalization of Streptavidin beads

Western Blot optimization and Validation of Pull-Down Experiments

To confirm the validity of the approach, we conducted western blot analysis of the pull-down experiments to confirm that known targets of Martinostat behave as predicted under the chosen conditions. The engagement of Martinostat with HDAC2 and HDAC6 could be confirmed via reduced binding at higher concentration of competing Martinostat in the lysate. (Figure 3.18) Other proteins, like LSD1 and HDAC10, did not show a clear dose-dependent blockade. These results are in accordance with previous data and may serve as a quality control criteria for mass spectrometry data analysis.

TMT10 mass spectrometry for target ID

In recent years, the number of chemoproteomic methods has drastically increased and a diverse array of different questions can be addressed with sophisticated com-

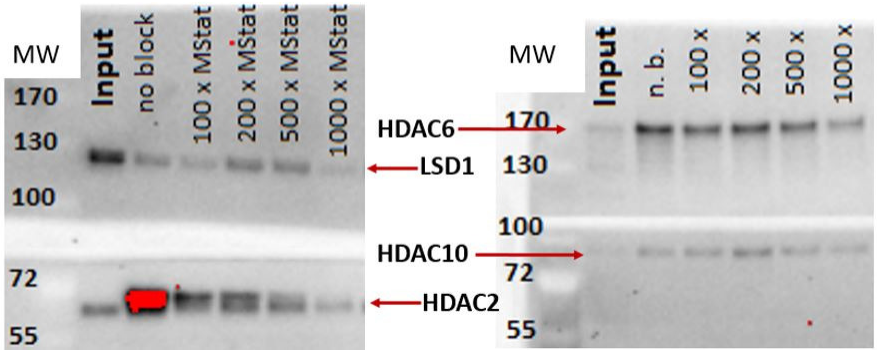

Figure 3.18: Competition of Martinostat with matrix to establish QC for MS outcome: While HDAC2 and HDAC6 clearly exhibit reduced binding upon increased Martinostat concentration, HDAC10 and LSD1 do not show decreased signal.

binations of chemical tags, stable isotope labeling and elaborate mass spectrometric analysis [175,176]. The approach chosen to elucidate the targets of [^{11}C]Martinostat is based on chemical tags with differential isotope labeling, known as tandem mass tags (TMT). A set of 10 distinct mass tags known as TMT10 or TMT 10-plex is commercially available and can be used to discern differential protein abundance in complex samples with two replicates for up to five different experimental conditions [177].

In order to overcome the inherent bias of western blot analysis, the pull-down protocol was optimized for mass spectrometry applications. Specifically, no blocking protein was used and additional washing steps ensured the complete removal of surfactants and other interference compounds.

We conducted a TMT10 analysis of different concentrations of Martinostat competitor in the brain tissue lysate. Solubility of the compound limited the maximum excess to 1000x bead capacity. We additionally compared 500x, 200x and 100x excess of soluble competitor to the protein levels after enrichment in the presence of vehicle only. While these investigations are still ongoing, an exemplary analysis is shown

as a volcano plot in Figure 3.19. The absolute magnitude of the abundance difference is plotted against the p-value of the difference. The further away a protein is located from the origin, the more likely it is a target of Martinostat – either directly or through association. As shown in Figure 3.19, HDAC2 and HDAC6 are the only HDACs identified to engage Martinostat as predicted. HDAC1 and HDAC3 could not be detected. HDAC11 is a known binding partner of HDAC6, which could explain the decreased HDAC11 binding to the solid phase with competing Martinostat.

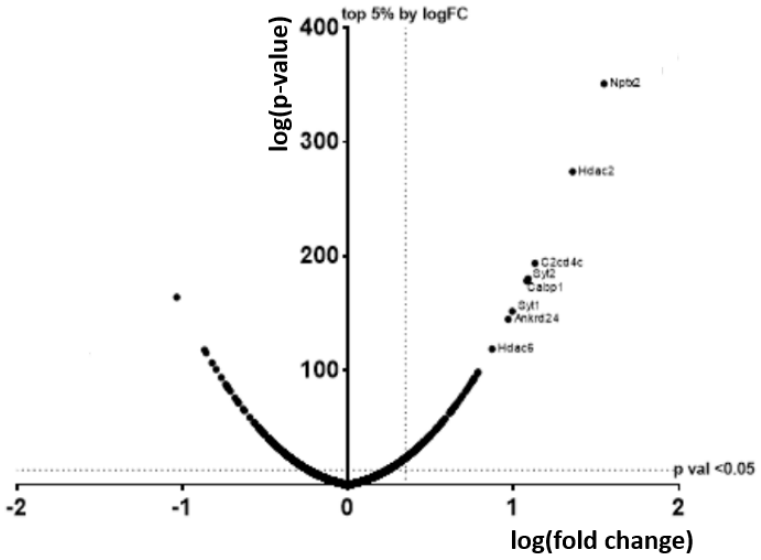

Figure 3.19: Volcano plot of comparison between vehicle and 200x excess Martinostat competition: Beyond the expected HDAC2 and HDAC6, a number of other proteins, most notably several synaptic proteins, show behavior suggestive of Martinostat binding or association with HDAC

In summary, we made headway towards an unbiased target-ID platform based on chemoproteomics, that could clarify in an unbiased manner how different HDAC isoforms, their complexes and non-HDAC proteins contribute to the overall signal observed in [^{11}C]Martinostat and [^{18}F]MGS3 imaging.

3.4 Experimental

3.4.1 Chemical synthesis

Materials and Methods

All air- and moisture-insensitive reactions were carried out under an ambient atmosphere and magnetically stirred. All air- and moisture-sensitive manipulations were performed using oven-dried glassware, under nitrogen atmosphere. Flash chromatography was performed on Dynamic Adsorbents Silica Gel 40-63 μm particle size on a Biotage Isolera One instrument, with an automatically generated gradient of hexanes and ethyl acetate. Anhydrous acetonitrile was purchased from VWR and used as received. All deuterated solvents were purchased from Cambridge Isotope Laboratories. NMR spectra were recorded on either a Varian Unity/Inova 600 spectrometer operating at 600 MHz for ^{1}H acquisitions, a Varian Unity/Inova 500 spectrometer operating at 500 MHz and 125 MHz for ^{1}H and ^{13}C acquisitions, respectively, or a Varian Mercury 400 spectrometer operating at 375 MHz for ^{19}F acquisitions. Chemical shifts are reported in ppm with the solvent resonance as the internal standard. For ^{1}H NMR: $CDCl_3$, 7.26; DMSO-d_6, 2.05; For ^{13}C NMR: $CDCl_3$, 77.16; DMSO-d_6, 39.52. Data is reported as follows: s = singlet, d = doublet, t = triplet, q = quartet, m = multiplet, br = broad; coupling constants in Hz; carbon signals are singlets unless otherwise noted. All substrates were used as received from commercial suppliers, unless otherwise stated.

4-Formyl-3-Nitro Methyl Cinnamate (10)

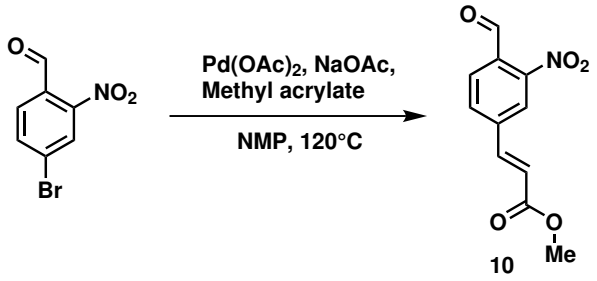

To 4-bromo-2-nitrobenzaldehyde (5.70 g, 24.5 mmol, 1.00 eq), oven-dried sodium acetate (2.24 g, 27.3 mmol, 1.10 eq) and palladium acetate (11 mg, 50 μmol, 2.0 mol%) under nitrogen atmosphere was added 60 mL NMP. The mixture was heated to 120 °C and methyl acrylate (3.20 g, 37.2 mmol, 1.50 eq) were added as soon as the temperature was reached. After TLC showed complete consumption of starting material, the mixture was cooled to room temperature, partitioned between ethyl acetate and 5% LiCl (aq) and the aqueous layer was extracted twice more with ethyl acetate. The combined organic layers were washed twice with 5% LiCl (aq) and then brine, dried over $MgSO_4$, filtered and concentrated in vacuo. The residue was purified by flash column chromatography. 5.70 g (24.2 mmol, 98.8 %) of **10** was obtained as an off-white solid.

NMR Spectroscopy:

^{1}**H NMR** (500 MHz, $CDCl_3$, 23 °C, δ): 10.42 (s, 1 H), 8.23 (d, J=1.0 Hz, 1 H), 7.99 (d, J=7.8 Hz, 1 H), 7.88 (d, J=8.3 Hz, 1 H), 7.72 (d, J=16.1 Hz, 1 H), 6.63 (d, J=15.7 Hz, 1 H), 3.85 (s, 3 H).

^{13}**C NMR** (125 MHz, $CDCl_3$, 23 °C, δ): 187.3, 166.0, 150.0, 140.6, 140.2, 132.7,

131.4, 130.4, 123.4, 123.3, 52.2.

HRMS(m/z) calc′d for $C_{11}H_NO_5$ $[M+H]^+$, 236.0559; found, 236.0563.

4-(1,3-dithiolan-2-yl)-3-nitro methyl cinnamate (14)

To aldehyde **10** (200 mg, 851 μmol, 1.00 eq) was added 1,2-ethanedithiol (86 μl, 1.0 mmol, 1.2 eq), pTsOH monohydrate (20 mg, 0.12 mmol, 14 mol%), 4 g silica gel and 25 mL DCM. The mixture was stirred at reflux for 2.5 h, cooled to room temperature and filtered. The silica gel was washed with three lots of DCM and the combined filtrates were concentrated in vacuo. The residue was purified by flash chromatography. 260 mg (835 μmol, 98.1%) of **14** was obtained as a light yellow solid.

NMR Spectroscopy:

^{1}**H NMR** (500 MHz, $CDCl_3$, 23 °C, δ): 8.08 (d, J=8.3 Hz, 1 H), 7.98 (s, 1 H), 7.70 (d, J=7.8 Hz, 1 H), 7.63 (d, J=16.1 Hz, 1 H), 6.49 (d, J=16.1 Hz, 1 H), 6.16 (s, 1 H), 3.81 (s, 3 H), 3.32 - 3.58 ppm (m, 4 H).

^{13}**C NMR** (125 MHz, $CDCl_3$, 23 °C, δ): 166.5, 148.5, 141.4, 138.7, 135.0, 131.9, 131.1, 123.7, 120.9, 52.0, 50.4, 40.0.

HRMS(m/z) calc′d for $C_{13}H_{13}S_2NO_4$ $[M+H]^+$, 312.0359; found, 312.0363.

Dioxazole dithioacetal 15

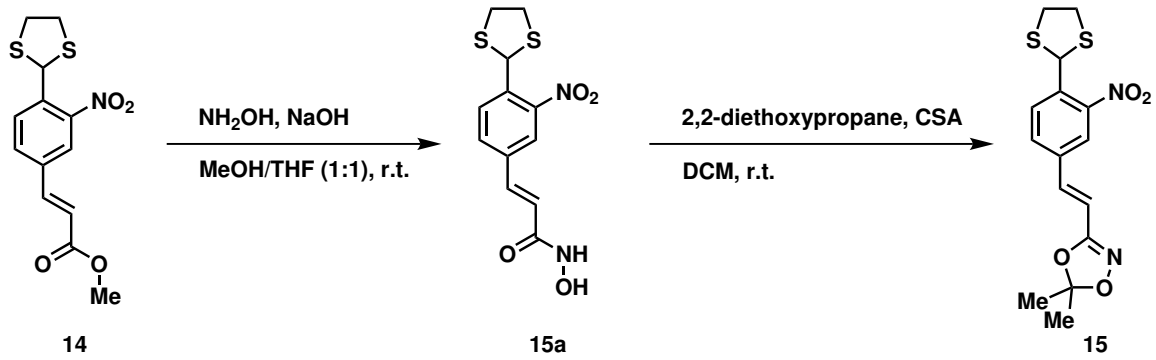

Ester **14** (200 mg, 640 μmol, 1 eq) was dissolved in 3 mL MeOH/THF (1:1). At room temperature, 0.5 mL hydroxylamine solution (50% in water) and 0.5 mL 5M NaOH were added. After 2 minutes, the mixture was poured onto 10 mL of an ice/water mixture and 2 mL conc. HCl were added. The mixture was kept at 0°C for several minutes, then the precipitate was isolated by filtration and washed with water. 102 mg (327 μmol, 51.1%) of hydroxamic acid **15a** were obtained and used without further purification after drying under high vacuum for 24 h.

To a suspension of hydroxamate (50 mg, 0.16 mmol, 1 eq) in 4 mL DCM was added 2,2-diethoxypropane (63 mg, 0.48 mmol, 3 eq) and camphorsulfonic acid (37 mg, 0.16 mmol, 1 eq). The solution became clear within a few minutes, stirring was continued for four hours at room temperature until no hydroxamic acid was remaining. The solution was washed with brine, dried over $MgSO_4$, filtered and concentrated in vacuo. The product was purified by flash chromatography. **15** was obtained as a light yellow oil (39 mg, 0.11 mmol, 69%).

NMR Spectroscopy:

^{1}H NMR (500 MHz, $CDCl_3$, 23 °C, δ): 8.08 (d, J=8.3 Hz, 1 H), 7.91 (d, J=1.5 Hz, 1 H), 7.67 (dd, J=8.3, 1.5 Hz, 1 H), 7.13 (d, J=16.1 Hz, 1 H), 6.67 (d, J=16.1 Hz, 1 H), 6.17 (s, 1 H), 3.31 - 3.51 (m, 4 H), 1.65 ppm (s, 6 H).

^{13}C NMR (125 MHz, $CDCl_3$, 23 °C, δ): 157.8, 148.6, 137.8, 135.7, 134.2, 131.1, 130.9, 123.2, 116.1, 112.6, 50.4, 39.6, 24.9.

HRMS(m/z) calc′d for $C_{15}H_{16}S_2N_2O_4$ $[M+H]^+$, 353.0624; found, 353.0621.

3-(4-formyl-3-nitrostyryl)-5,5-dimethyl-1,4,2-dioxazole (16)

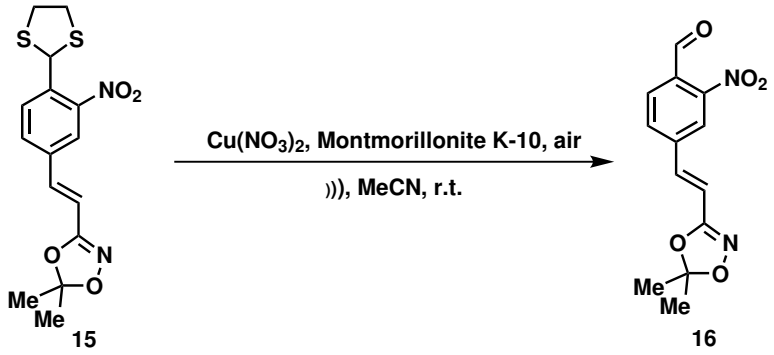

To an emulsion of Montmorillonite K-10 (160 mg) and copper sulfate hydrate (84 mg, 0.36 mmol, 3.0 eq) in 1 mL of acetonitrile was added dithiolane **15** (42 mg, 0.12 mmol, 1.0 eq). The mixture was sonicated under ambient atmosphere for 3h, concentrated in vacuo, and 10 mL DCM were added to the residue. The insoluble matter was removed by filtration and the filtrate was concentrated in vacuo. The product was purified by flash column chromatography. 31 mg (0.11 mmol, 92%) of **16** was obtained as a light yellow solid.

NMR Spectroscopy:

^{1}H NMR (500 MHz, $CDCl_3$, 23 °C, δ): 10.42 (s, 1 H), 8.16 (d, J=1.76 Hz, 1 H), 7.99 (d, J=8.22 Hz, 1 H), 7.85 (dd, J=8.80, 1.80 Hz, 1 H), 7.21 (d, J=15.80 Hz, 1 H), 6.82 (d, J=15.85 Hz, 1 H), 1.67 (s, 6 H).

^{13}C NMR (125 MHz, $CDCl_3$, 23 °C, δ): 187.3, 157.6, 147.2*, 140.9, 133.5, 131.6, 130.6, 130.4, 123.1, 116.6, 115.1, 24.6. *peak very weak

HRMS(m/z) calc′d for $C_{13}H_{12}N_2O_5$ $[M+H]^+$, 276.0746; found, 276.0755.

3-fluoro-4-formyl methyl cinnamate (11)

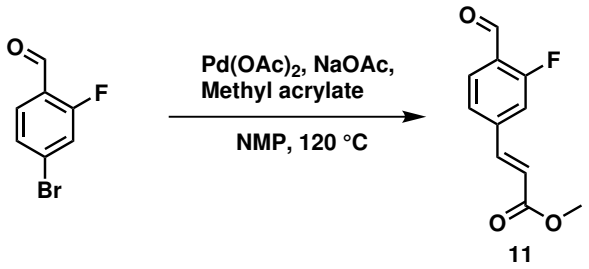

11

To 4-bromo-2-fluorobenzaldehyde (10.0 g, 49.3 mmol, 1.00 eq), oven-dried sodium acetate (4.44 g, 5.42 mmol, 1.10 eq) and palladium acetate (14 mg, 0.20 mmol, 4.0 mol%) under nitrogen atmosphere was added 80 mL NMP. The mixture was heated to 120 °C and methyl acrylate (6.60 mg, 76.4 mmol, 1.55 eq) were added as soon as the temperature was reached. After TLC showed complete consumption of starting material, the mixture was cooled to room temperature, partitioned between ethyl acetate and 5% LiCl (aq) and the aqueous layer was extracted twice more with ethyl acetate. The combined organic layers were washed twice with 5% LiCl (aq) and brine,

dried over $MgSO_4$, filtered and concentrated in vacuo. The residue was purified by flash column chromatography. **11** (8.42g, 40.0 mmol, 82.0%) was obtained as an off-white solid.

NMR Spectroscopy:

^{1}**H NMR** (500 MHz, Chloroform-d, 23 °C, δ): 10.34 (s, 1 H), 7.88 (t, J=7.3 Hz, 1 H), 7.64 (d, J=15.7 Hz, 1 H), 7.40 (d, J=8.3 Hz, 1 H), 7.30 (d, J=10.8 Hz, 1 H), 6.53 (d, J=16.1 Hz, 1 H), 3.82 ppm (s, 3 H).

^{13}**C NMR** (125 MHz, Chloroform-d, 23 °C, δ): 186.36, 166.05 (d, J=93.5 Hz), 163.63, 142.36, 141.88, 129.22, 124.74, 124.15, 122.12, 115.47 (d, J=20.0 Hz), 52.06.

^{19}**F NMR** (470 MHz, Chloroform-d, 23 °C, δ): –124.36.

HRMS(m/z) calc'd for $C_{11}H_9FO_3$ $[M+H]^+$, 208.0536; found, 208.0546.

5,5-dimethyl-3-styryl-1,4,2-dioxazole (20)

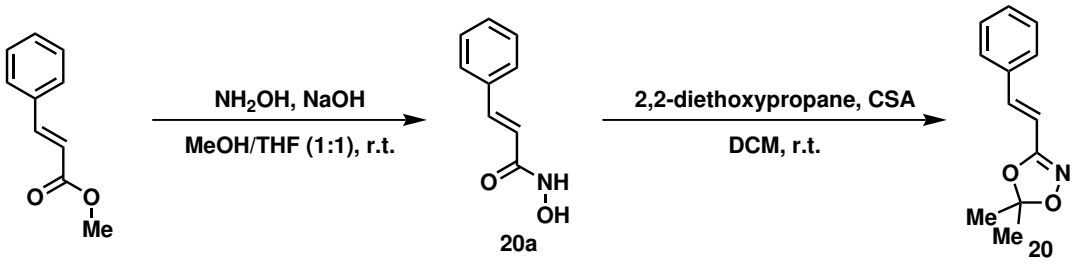

To ethyl cinnamate (5.00 g, 28.4 mmol, 1.00 eq) in 20 mL MeOH/THF (1:1) was added 20 mL 50% aqueous hydroxylamine and stirred at room temperature for 12 h. The reaction mixture was then poured onto ice/6M HCl (50 mL) and extracted with DCM and twice with ethyl acetate. The combined organic layers were washed with brine, dried over sodium sulfate and filtered. The filtrate was concentrated in vacuo to afford a colorless oil, which was triturated with ether until crystallization occurred. The white solid was isolated by filtration, washed with water and ether and dried under vacuum. 3.20 g (19.6 mmol, 69.0 %) of cinnamyl hydroxamate were obtained and used without further purification.

To cinnamyl hydroxamate (3.00 g, 18.4 mmol, 1.00 eq) in 50 mL DCM were added camphorsulfonic acid (4.27 g, 18.4 mmol, 1.00 eq) and 2,2-diethoxypropane (7.30 g, 55.2 mmol, 3.00 eq). The mixture was stirred for 12 hours at room temperature. The solution was then washed with water and brine, dried over magnesium sulfate, filtered and concentrated in vacuo. The light yellow oil was subjected to flash column chromatography to afford **20** (2.78 g, 13.7 mmol, 74.0%) as a white solid.

NMR Spectroscopy:

^{1}**H NMR** (500 MHz, Chloroform-d, 23 °C, δ): 7.47 (d, J=6.6 Hz, 2 H), 7.29 - 7.42

(m, 3 H), 7.18 (d, J=16.4 Hz, 1 H), 6.61 (d, J=16.4 Hz, 1 H), 1.66 ppm (s, 6 H).

^{13}**C NMR** (500 MHz, Chloroform-d, 23 °C, δ): 158.5, 137.7, 135.0, 129.5, 128.9, 127.3, 115.4, 109.5, 24.8.

HRMS(m/z) calc'd for $C_{12}H_{13}NO_2$ $[M+H]^+$, 204.1019; found, 204.1026.

Methyl 4-(((cyclohexylmethyl)amino)methyl-3-fluorocinnamate (12a)

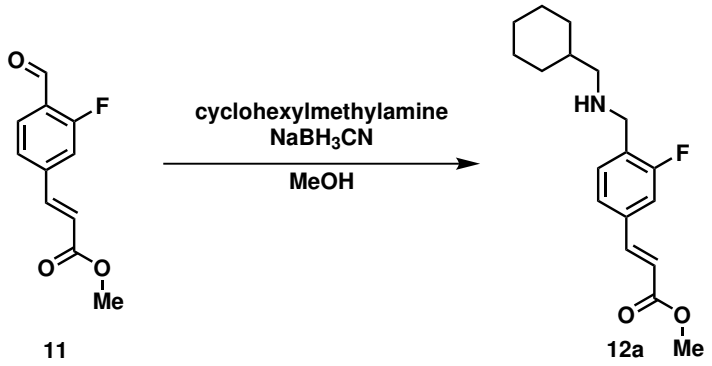

To a solution of cyclohexylmethylamine (652 mg, 5.76 mmol, 1.20 eq) and **10** (1.00 g, 4.80 mmol, 1.00 eq) in 10 mL methanol was added sodium cyanoborohydride (452 mg, 7.20 mmol, 1.50 eq) and stirred at room temperature for 24 h. The reaction mixture was then partitioned between ethyl acetate and water, the aqueous layer was extracted two more times with ethyl acetate, the combined organic layers were washed with brine, dried over magnesium sulfate, filtered and concentrated in vacuo. The oily residue was redissolved in dichloromethane and concentrated HCl was added until no further precipitation was observed. The solid was isolated by filtration, washed with isopropanol, ether and dried under vacuum. **12a** (1.45 g, 4.75 mmol, 82.4 %) was

obtained as a white solid.

NMR Spectroscopy:

^{1}H NMR (500 MHz, DMSO-d_6, 23 °C, δ): 9.54 (br. s., 2 H), 7.84 (s, 1 H), 7.72 (d, J=10.8 Hz, 1 H), 7.58 - 7.68 (m, 2 H), 6.77 (d, J=16.1 Hz, 1 H), 4.13 (s, 2 H), 3.34 (s, 2 H), 2.73 (d, J=6.4 Hz, 2 H), 1.51 - 1.90 (m, 6 H), 1.02 - 1.27 (m, 3 H), 0.90 ppm (d, J=12.2 Hz, 2 H).

^{13}C NMR (125 MHz, DMSO-d_6, 23 °C, δ): 166.84, 161.21 (d, J=232.7 Hz), 143.06, 137.70, 133.39, 125.06, 121.50, 120.55, 115.10, 52.86, 52.10, 52.07, 43.54, 34.60, 30.55, 26.00, 25.49.

^{19}F NMR (470 MHz, DMSO-d_6, 23 °C, δ): -115.51.

HRMS(m/z) calc′d for $C_{18}H_{24}FNO_2$ $[M+H]^+$, 306.1869; found, 306.1937.

Methyl 4-(((adamantylmethyl)amino)methyl-3-fluorocinnamate (12b)

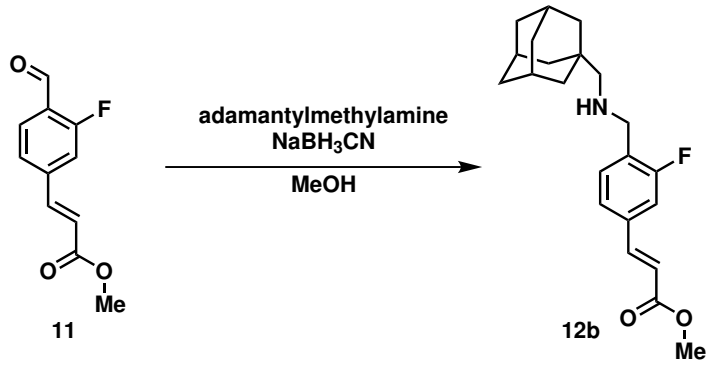

A solution of adamantylmethylamine (95.2 mg, 0.576 mmol, 1.20 eq) and **11** (100 mg, 0.480 mmol, 1.00 eq) in 2 mL methanol was stirred for 30 min, then sodium borohydride (27.2 mg, 0.720 mmol, 1.50 eq) and stirred at room temperature for 12 h. The reaction mixture was then partitioned between ethyl acetate and water, the aqueous layer was extracted two more times with ethyl acetate, the combined organic layers were washed with brine, dried over magnesium sulfate, filtered and concentrated in vacuo. The oily residue was purified by flash column chromatography. **12b** (135 mg, 0.378mmol, 78.8%) was obtained as a white solid.

NMR Spectroscopy:

^{1}**H NMR** (500 MHz, $CDCl_3$, 23 °C, δ): 7.60 (d, J=16.1 Hz, 1 H), 7.37 (t, J=7.6 Hz, 1 H), 7.24 (d, J=7.8 Hz, 1 H), 7.16 (d, J=10.8 Hz, 1 H), 6.38 (d, J=15.7 Hz, 1 H), 3.81 (s, 2 H), 3.78 (s, 3 H), 2.20 (s, 2 H), 1.93 (br. s., 3 H), 1.65 - 1.72 (m, 3 H), 1.57 - 1.64 (m, 3 H), 1.49 ppm (s, 6 H).

^{13}**C NMR** (125 MHz, $CDCl_3$, 23 °C, δ): 167.12, 161.20 (d, J=246.1 Hz), 143.47, 134.91 (d, J=7.6 Hz), 130.41 (d, J=5.7 Hz), 130.23 (d, J=15.3 Hz),124.01, 118.47,

114.03 (d, J=25.8 Hz), 61.97, 51.74, 47.73 (d, J=1.9 Hz), 40.79, 37.18, 33.40, 28.42.

^{19}**F NMR** (470 MHz, $CDCl_3$, 23 °C, δ): −118.81.

HRMS(m/z) calc′d for $C_{22}H_{28}FNO_2$ $[M+H]^+$, 358.2182; found, 358.2240.

Methyl 4-(((adamantylmethyl)(methyl)amino)methyl-3-fluorocinnamate (12c)

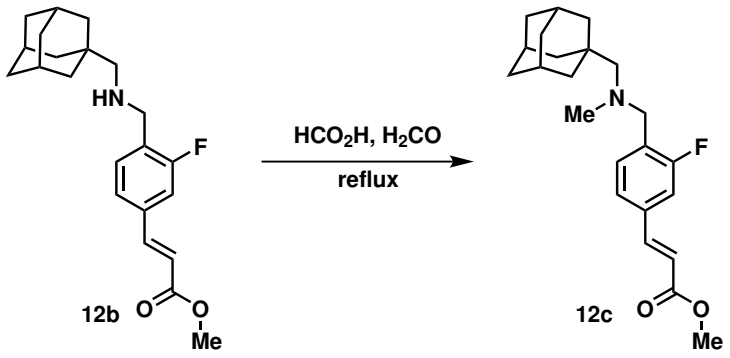

12b (150 mg, 420 μmol) was heated at reflux in 2 mL formic acid and 2 mL formalin for 24 h. The reaction mixture was neutralized with saturated sodium bicarbonate solution and partitioned between water and ethyl acetate. The aqueous layer was extracted twice more with ethyl acetate, the combined organic layers were washed with water and brine, dried over magnesium sulfate, filtered and concentrated in vacuo. The residue was purified by flash column chromatography to yield **12c** (101 mg, 273 μmol, 65%) as a white solid.

NMR Spectroscopy:

^{1}**H NMR** (500 MHz, $CDCl_3$, 23 °C, δ): 7.69 (d, J=16.1 Hz, 1H), 7.61 (s, 1H), 7.27 - 7.39 (m, 2H), 7.23 (d, J=10.3 Hz, 1H), 6.47 (d, J=16.1 Hz, 1H), 3.87 (br. s., 3H), 3.66 (br. s., 2H), 2.29 (s, 3H), 2.18 (s, 2H), 2.00 (s, 3H), 1.62 - 1.81 (m, 6H), 1.56 (s,

6H).

^{13}**C NMR** (125 MHz, $CDCl_3$, 23 °C, δ): 167.21, 161.31 (d, J=237.5 Hz), 143.61, 134.72, 131.39, 129.56, 123.84, 118.38, 114.15, 113.96, 71.02, 57.23, 51.76, 45.65, 41.02, 37.23, 35.18, 28.50.

^{19}**F NMR** (470 MHz, $CDCl_3$, 23 °C, δ): −117.62.

HRMS(m/z) calc′d for $C_{23}H_{30}FNO_2$ $[M+H]^+$, 372.2339; found, 372.2388.

Methyl 4-(((adamantylmethyl)amino)methyl)-cinnamate (24)

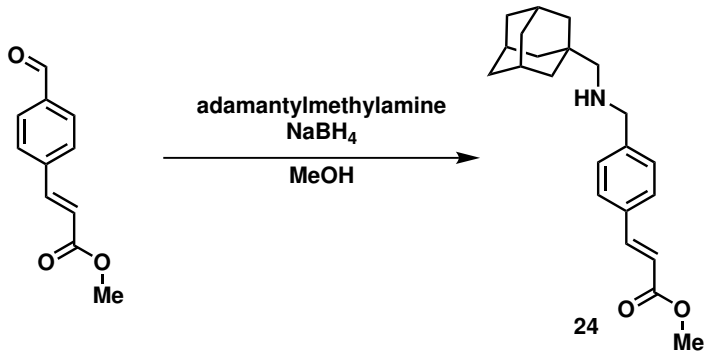

Adamantylmethylamine (1.0 g, 6.0 mmol, 1.1 eq) and (E)-methyl 4-formylcinnamate (1.0 g, 5.3 mmol, 1.0 eq) was dissolved in MeOH (30 mL) and the mixture was stirred at room temperature for 2 h. Sodium borohydride (0.61g, 16 mmol, 3.0 eq) was then added, and the suspension was stirred overnight at room temperature. The white precipitate was filtered and dried to obtain **24** (1.35 g, 4.0 mmol, 75%) as a white solid.

NMR Spectroscopy:

^1H **NMR** (500 MHz, $CDCl_3$, 23 °C, δ): 7.69 (d, J=15.7 Hz, 1 H), 7.48 (d, J=8.3

Hz, 2 H), 7.35 (d, J=7.8 Hz, 2 H), 6.42 (d, J=15.7 Hz, 1 H), 3.76 - 3.85 (m, 5 H), 2.23 (s, 2 H), 1.96 (br. s., 3 H), 1.59 - 1.76 (m, 6 H), 1.47 - 1.56 ppm (m, 6 H).

^{13}C NMR (125 MHz, $CDCl_3$, 23 °C, δ): 167.6, 144.8, 143.7, 132.9, 128.4, 128.1, 117.1, 62.1, 54.3, 51.7, 40.9, 37.2, 33.5, 28.5.

HRMS(m/z) calc′d for $C_{22}H_{29}NO_2$ $[M+H]^+$, 340.2277; found, 340.2242.

Methyl 4-(((adamantylmethyl)(2-fluoroethyl)amino)methyl)-cinnamate (25)

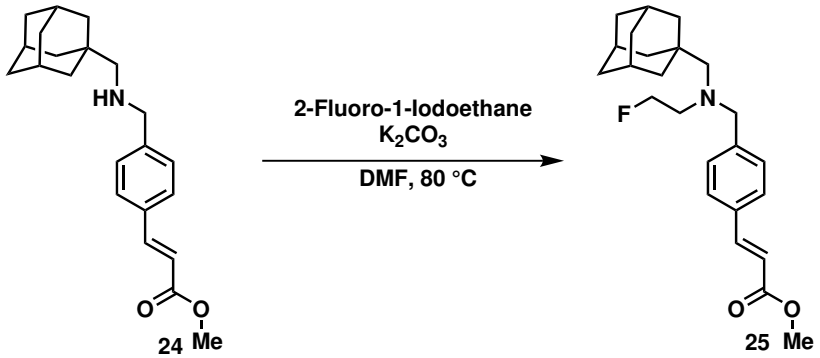

To a solution of **21** (220 mg, 0.647 mmol, 1.00 eq) in 3 mL DMF was added 2-fluoro-1-iodoethane (118 mg, 0.679 mmol, 1.05 eq) and sodium hydride (19 mg, 0.78 mmol, 1.20 eq) and stirred at 80°C under nitrogen atmosphere for 48 h. The reaction mixture was cooled to room temperature, partitioned between water and ethyl acetate, the aqueous layer extracted twice with ethyl acetate and the combined organic layers washed with water and brine. The organic phases were then dried over magnesium sulfate, filtered and concentrated in vacuo. The product was purified by flash chromatography. **25** (78 mg, 0.202 mmol, 31%) was obtained as a clear oil.

NMR Spectroscopy:

^{1}H NMR (500 MHz, $CDCl_3$, 23 °C, δ): 7.69 (d, J=15.7 Hz, 1 H), 7.37 - 7.53 (m, 4 H), 6.42 (d, J=16.1 Hz, 1 H), 4.34 - 4.54 (m, 2 H), 3.81 (s, 3 H), 3.71 (s, 2 H), 2.62 - 2.78 (m, 2 H), 2.26 (s, 2 H), 1.95 (br. s., 3 H), 1.59 - 1.79 (m, 6 H), 1.52 ppm (br. s., 6 H).

^{13}C NMR (125 MHz, $CDCl_3$, 23 °C, δ): 167.6, 144.8, 143.0, 133.0, 128.9, 128.0, 117.1, 82.8, 68.6, 55.8, 51.7, 41.2, 37.2, 35.1, 31.6, 28.5.

^{19}F NMR (470 MHz, $CDCl_3$, 23 °C, δ): −220.52.

HRMS(m/z) calc′d for $C_{24}H_{32}FNO_2$ $[M+H]^+$, 386.2495; found, 386.2510.

General Procedure for Synthesis of Hydroxamates

To a solution of the respective ester (1 mmol) in 5 ml MeOH/THF (1:1) was added sequentially 1.5 mL hydroxylamine solution (50% in water) and 1 mL 1 M NaOH. The reaction mixture was stirred at room temperature until TLC showed complete consumption of starting material. Then, the reaction mixture was cooled to 0 °C and brought to pH 7 with 1M HCl, when precipitation occurred. The solid was isolated by filtration, washed with water and dried under high vacuum.

Characterization MGS1

NMR Spectroscopy:

^{1}**H NMR** (500 MHz, DMSO-d_6, 23 °C, δ): 10.93 (br. s., 1H), 9.00 - 9.48 (br. s., 1H), 7.74 (d, J=7.3 Hz, 1H), 7.31 - 7.57 (m, 3H), 6.58 (dd, J=15.9, 3.7 Hz, 1H), 4.14 (s, 2H), 2.76 (s, 2H), 1.48 - 1.88 (m, 6H), 1.02 - 1.27 (m, 3H), 0.80 - 0.99 (m, 2H).

^{13}**C NMR** (125 MHz, DMSO-d_6, 23 °C, δ): 163.3, 162.0 (d, J=246.5 Hz), 139.5, 137.4, 134.1, 124.6, 122.9, 120.9, 115.2, 53.6, 44.3, 35.3, 31.2, 26.7, 26.2.

^{19}**F NMR** (470 MHz, DMSO-d_6, 23 °C, δ): -115.58.

HRMS(m/z) calc′d for $C_{17}H_{23}FN_2O_2$ $[M+H]^+$, 307.1781; found, 307.1822.

Characterization MGS2

NMR Spectroscopy:

^{1}**H NMR** (500 MHz, DMSO-d_6, 23 °C, δ): 7.46 (t, J=7.8 Hz, 1H), 7.25 - 7.40 (m, 3H), 6.47 (d, J=16.1 Hz, 1H), 3.67 (s, 2H), 2.10 (s, 3H), 1.89 (s, 3H), 1.51 - 1.72 (m, 6H), 1.45 (s, 6H).

^{13}**C NMR** (125 MHz, DMSO-d_6, 23 °C, δ): 163.6, 161.7 (d, J=236 Hz), 137.2, 136.7, 131.4, 130.0, 124.3, 121.6, 114.6, 62.5, 47.7, 41.4, 37.8, 34.3, 28.9.

^{19}**F NMR** (470 MHz, DMSO-d_6, 23 °C, δ): −119.45.

HRMS(m/z) calc′d for $C_{21}H_{27}FN_2O_2$ $[M+H]^+$, 359.2135; found, 359.2155.

Characterization MGS3

NMR Spectroscopy:

^{1}**H NMR** (500 MHz, DMSO-d_6, 23 °C, δ): d = 7.30 - 7.55 (m, 4 H), 6.45 (d, J=15.6 Hz, 1 H), 3.53 (s, 2 H), 2.15 (s, 3 H), 2.02 - 2.10 (m, 2 H), 1.88 (br. s., 3 H), 1.50 - 1.70 (m, 6 H), 1.43 ppm (br. s., 6 H) .

^{13}**C NMR** (125 MHz, DMSO-d_6, 23 °C, δ): 162.92, 161.32 (d, J=243.6 Hz), 137.41, 136.36, 132.08, 127.88 (d, J=24.9 Hz), 123.13, 120.53, 114.32 (d, J=27.8 Hz), 70.49, 57.27, 45.87, 40.88, 37.19, 35.18, 28.29.

^{19}**F NMR** (470 MHz, DMSO-d_6, 23 °C, δ): −117.22.

HRMS(m/z) calc′d for $C_{21}H_{27}FN_2O_2$ $[M+H]^+$, 373.2291; found, 373.2256.

Characterization CN146

NMR Spectroscopy:

^{1}**H NMR** (500 MHz, DMSO-d_6, 23 °C, δ): 10.74 (br. s., 1 H), 9.01 (br. s., 1 H), 7.50 (d, J=8.3 Hz, 2 H), 7.36 - 7.45 (m, 3 H), 6.43 (d, J=14.7 Hz, 1 H), 4.43 (dt, J=47.4, 4.9 Hz, 2 H), 3.64 (s, 2 H), 2.62 (dt, J=25.9, 4.9 Hz, 2 H), 2.22 (s, 2 H), 1.89 (br. s., 3 H), 1.64 (d, J=11.7 Hz, 3 H), 1.57 (d, J=11.2 Hz, 3 H), 1.47 ppm (br. s., 6 H).

^{13}**C NMR** (125 MHz, DMSO-d_6, 23 °C, δ): 163.31, 142.11, 138.59, 133.75, 129.22, 127.85, 118.92, 82.95 (d, J=170.6 Hz), 67.94, 61.54, 55.95 (d, J=26.8 Hz), 40.94, 37.17, 35.10, 28.27.

^{19}**F NMR** (470 MHz, DMSO-d_6, 23 °C, δ): −219.41.

HRMS(m/z) calc′d for $C_{21}H_{27}FN_2O_2$ $[M+H]^+$, 387.2448; found, 387.2518.

Methylcinnamate diamine 26

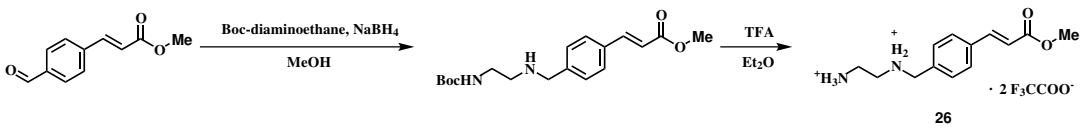

26

To a solution of Methyl 4-formylcinnamate (250 mg, 1.31 mmol, 1.00 eq) in 3 mL methanol was added Boc-ethylenediamine (315 mg, 2.00 mmol, 1.50 eq) and stirred for 2h at room temperature. Then, sodium borohydride (495 mg, 13.1 mmol, 10.0 eq) was added in small portions and the mixture stirred for another 2h. Then, the reaction mixture was concentrated in vacuo, and the intermediate was purified by flash chromatography. The product was dissolved in 10 mL ether and 1 mL trifluoroacetic acid was added and the reaction was stirred at room temperature for 3h. The precipitate was isolated by filtration and dried under vacuum. The product (292 mg, 0.632 mmol, 48.2%) was isolated as a white solid.

NMR Spectroscopy:

^{1}**H NMR** (500 MHz, DMSO-d_6, 23 °C, δ): 8.50 (br. s., 5H), 7.75 (d, J = 7.9 Hz, 2H), 7.64 (d, J = 16.0 Hz, 1H), 7.56 (d, J = 7.9 Hz, 2H), 6.67 (d, J = 16.0 Hz, 1H), 4.22 (s, 2H), 3.70 (s, 3H), 3.24 – 3.18 (m, 4H).

^{13}**C NMR** (125 MHz, DMSO-d_6, 23 °C, δ): 167.01, 159.65, 144.10, 135.04, 134.33, 130.84, 128.96, 119.15, 116.16, 51.95, 50.14, 44.16, 35.63.

HRMS(m/z) calc′d for $C_{13}H_{18}N_2O_2$ $[M+H]^+$, 235.1441; found, 235.1445.

PEG-4 methylcinnamate 27

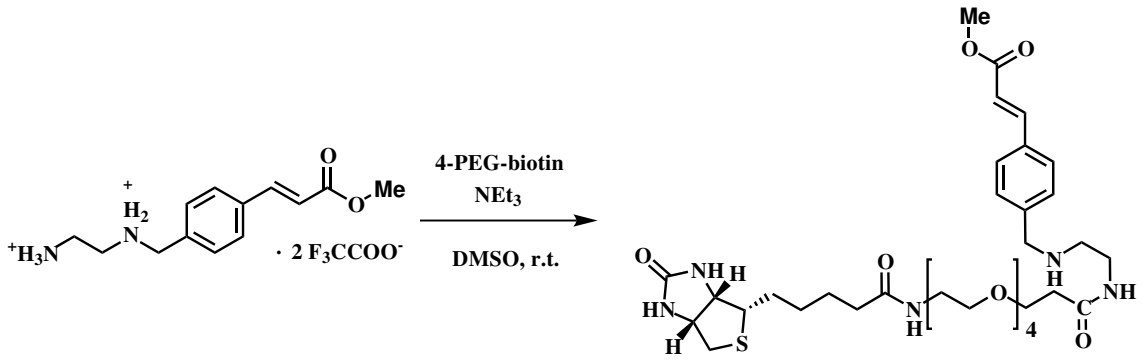

To a suspension of methyl (E)-4-(((2-aminoethyl)amino)methyl)cinnamate · 2 TFA (7.86 mg, 17.0 μmol, 1.00 eq) in DMSO (200 μL) was added 4-PEG-NHS-biotin (10.0 mg, 17.0 μmol, 1.00 eq) and triethylamine (7.1 μL, 51 µmol, 3.0 eq). After stirring for 12 h trimethylamine (7.1 μL, 51 μmol, 3.0 eq) was added again and the solution was stirred for 5 h. The product was purified by HPLC (Eclipse XDB-C18, 9.4x250 mm, 5μm, H_2O/MeCN/0.1% TFA from 95/5 to 5/95 over 60 min, 5mL·min^{-1} to afford 27 (8.88 mg, 12.5 μmol, 73.5%) as pale yellow waxy solid. **27** was then redissolved in 1 mL THF and 1 mL MeOH to give a stock solution with a concentration of 4.44 mg/mL.

HRMS(m/z) calc'd for $C_{34}H_{53}N_5O_9S$ $[M+H]^+$, 708.3637; found, 708.3640.

$\mathbf{R}_f$ (DCM/5%MeOH/0.5%TEA) = 0.59.

$\mathbf{R}_t$ (Eclipse XDB-C18, 4.6x150 mm, 5μm; MeCN/H_2O/0.1% TFA 5/95 to 95/5 over 10 min, 2ml·min^{-1}) = 2.5 min.

4PEG-biotin hydroxamate 22

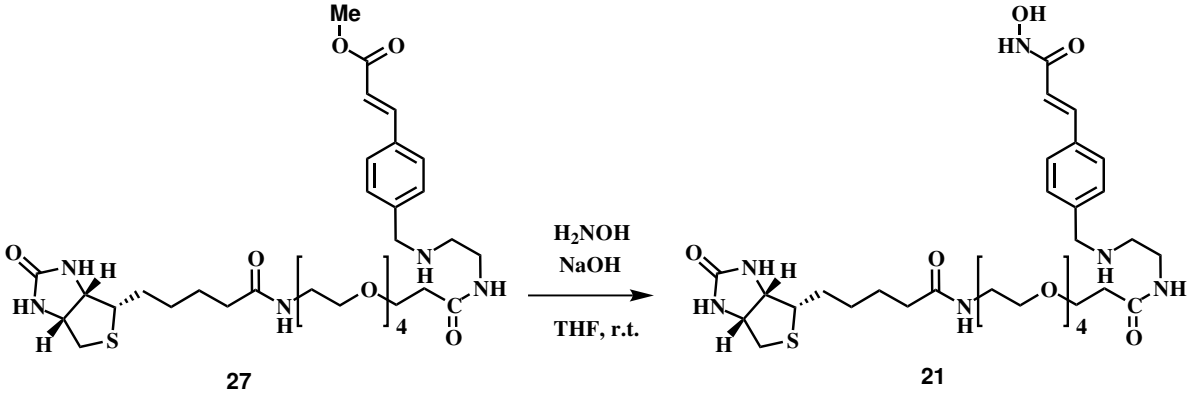

To a solution of 27 (500 μL, 2.22 mg, 3.13 μmol) was added hydroxylamine (100 μL, 50%) and sodium hydroxide (20 μL, 6M). After 10 min of stirring, the product was purified by semipreparative HPLC (Eclipse XDB-C18, 9.4x250 mm, 5μm, MeCN/H_2O/0.1% TFA from 5/95 to 50/50 over 45 min, 5mL·min^{-1}; R_t = 15.60 min) to give 6 as a purple, waxy solid (2.36 mg, 1.67 μmol, 53.4 %).

HRMS(m/z) calc'd for $C_{33}H_{52}N_6O_9S$ $[M+H]^+$, 709.3589 ; found, 709.3611.

$\mathbf{R}_t$ (Eclipse XDB-C18, 4.6x150 mm, 5μm; MeCN/H_2O/0.1% TFA 5/95 to 95/5 over 10 min, 2 ml·min^{-1}) = 3.1 min.

3.4.2 Radiochemistry

Preparation of [^{18}F]fluoride

Aqueous [^{18}F]fluoride obtained from a cyclotron was passed through a SPE Chromafix 30-PS-HCO_3 cartridge that had been previously conditioned with 5.0 mg·mL^{-1} aqueous potassium carbonate and then washed with 18 mL of Millipore Milli-Q water. The captured [^{18}F]fluoride was washed by passing 2 mL of Millipore Milli-Q water through the cartridge. [^{18}F]Fluoride was eluted from the cartridge into a conical vial using 5.0 mg·mL^{-1} of base in Millipore Milli-Q water/acetonitrile solution 1:4 (v/v)(2.0 mL, 6.6 μmol).

Note: for all semi preparative HPLC purifications in the following radiochemical procedures, a reverse phase column (Agilent Eclipse XDB-C18, 9.4 x 250mm,5 μm) was used.

[^{18}F]MGS1 and 2

[^{18}F]Fluoride (94.23 mCi for MGS1, 523.6 mCi for MGS2) was eluted from the cartridge into a 4 mL glass vial using 0.7 mL of 5.0 mg·mL^{-1} aqueous cesium carbonate. Azeotropic dry down at 110 °C was performed by adding 1 mL of dry acetonitrile to the eluted fluoride and evaporating the mixture under a stream of nitrogen gas. After complete evaporation, 1 ml of acetonitrile was added and evaporated in the same way, the process was repeated another time. After dry down, 10 μL Millipore Milli-Q water were carefully added to the solid, resolubilizing as much as possible of the precipitate. Then 0.8 mg of precursor 4 in 0.3 mL DMSO were added and

heated for 5 min at 110 °C. The solution was transferred into another 4 mL glass vial containing 20 μL of the respective amine and stirred for 5 min at room temperature. Then 1 mL of a saturated solution of sodium borohydride in isopropanol was added. After stirring for 10 min at 60 °C, the mixture was diluted to 2 mL with water and purifed by semi-preparative HPLC (gradient H_2O/MeCN with 0.1% TFA each at 5 ml·min^{-1}; [^{18}F]MGS1: 55:45 (v:v), R_T 8-10 min; [^{18}F]MGS2: 5 min 35:65 (v:v), then ramp to 60:40 (v:v) over 20 min, R_T 17 min). The isolated fractions containing the product were diluted with water, loaded onto a C-18 Sep-Pak solid phase extraction cartridge (conditioned with 1 mL ethanol and 20 mL water), washed with 10 mL of water and eluted with 1.5 mL isopropanol. 5 mg of 6 and 5 mg camphor sulfonic acid were added and the mixture was heated to 110 °C for 30 min. The vessel was opened for the last five minutes to reduce the volume. Then the mixture was diluted to 2 mL with water and purified by semi-preparative HPLC to isolate the product.

For [^{18}F]MGS1, a gradient 0.1 %TFA (aq)/MeCN (90:10 (v:v) for 5 min, then ramp to 35:65 (v:v) over 20 min, R_T about 11 min) was employed for separation and reformulation via a C-18 SepPak solid phase extraction cartridge was successful. 2.1 mCi of [^{18}F]MGS1 was obtained (7% radiochemical yield, decay corrected at TOI, 180 min synthesis time).

For [^{18}F]MGS2, a direct cut method using EtOH/0.01M NaOH (40:60 (v:v), R_T 40 min) was used to purify the final product and the eluted radiolabeled compound formulated by neutralizing the solution with acetic acid and dilution with saline to 10% ethanol content for injection. 1.5 mCi of [^{18}F]MGS2 was obtained (0.9% radiochemical yield, decay corrected at TOI, 180 min synthesis time).

[^{18}F]MGS3

[^{18}F]Fluoride (610 mCi) was eluted from the cartridge into a 4 mL glass vial using 0.4 mL of 5.0 mg·mL^{-1} aqueous potassium carbonate. Azeotropic dry down at 110 °C was performed by adding 0.7 mL of 5 mg·mL^{-1} $K_{2.2.2}$ in dry acetonitrile to the eluted fluoride and evaporating the mixture under a stream of nitrogen gas. After complete evaporation, 1 ml of acetonitrile was added and evaporated in the same way, the process was repeated another time. 1 mg of 4-formyl-3-nitro methyl cinnamate in 0.3 mL DMSO was added to the vial and heated to 110 °C for 5 minutes. The resulting brown liquid was diluted to 20 mL with water, loaded onto a SepPak C-18 solid phase extraction cartridge and elute with 1 mL EtOH into a vial containing adamantylmethyl methylamine and stirred for 5 min at room temperature. Then 65 mg $NaB(CN)H_3$ were added at once and the mixture stirred for 10 min at 60 °C, diluted to 2 mL with water and purifed by HPLC (gradient H_2O/MeCN with 0.1% TFA each, 75:25 (v:v) for 5 min, then ramp to 40:60 (v:v) over 20 min, R_T 17 min). The isolated fractions containing the product were diluted with water, loaded onto a C-18 Sep-Pak solid phase extraction cartridge, washed with 10 mL of water and eluted with 1.5 mL MeOH/TFA 1:1. To the solution were added 200 μL each 50% aq. NH_2OH and 6M NaOH and stirred at room temperature for 5 min. a gradient of water containing 0.1% TFA and acetonitrile was employed for separation (25:75 (v:v) for 5 min, then ramp to 65:35 (v:v) over 20 min, R_T about 16 min, broad peak). The fractions containing the product were diluted with water, loaded onto an Oasis

HLB solid phase extraction cartride and washed with 10 mL of water. The product was eluted with ethanol diluted with saline to 10% ethanol content for injection. 0.80 mCi [^{18}F]MGS3 was obtained (0.3% radiochemical yield, decay corrected at TOI, 130 min synthesis time).

Quality control of injected doses

Quality control was performed by analytical HPLC (Agilent Eclipse XDB-C18, 4.6 x 150mm, 5 μm). Aliquots of the injected dose were loaded onto an HPLC system to control their purity. In a second run, the radiolabeled product was coinjected with a non-radioactive standard and retention times were compared. After completion of the chromatograph, peaks on UV and radioactivity detector were integrated and the radiochemical and chemical purity were determined by the area of integration. All tracers matched the retention time of the respective standards and exceeded 95% chemical purity and 90% radiochemical purity. Shown below are γ-traces of purified radiotracer spiked with cold standard aligned with the UV-trace at 254 nm.

[^{18}F]MGS1

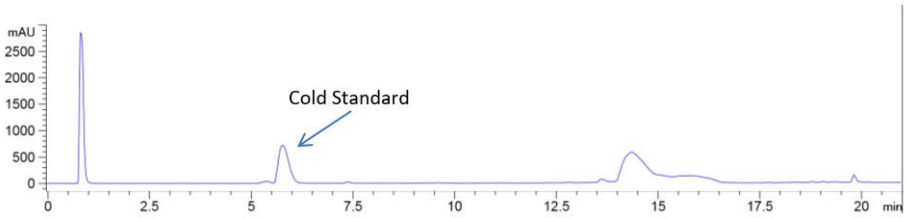

Figure 3.20: UV(254) trace of [^{18}F]MGS1

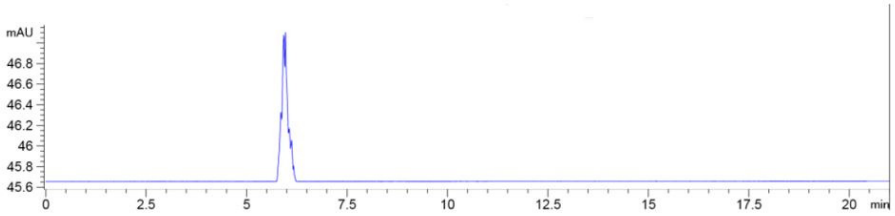

Figure 3.21: gamma trace of [^{18}F]MGS1

[^{18}F]MGS2

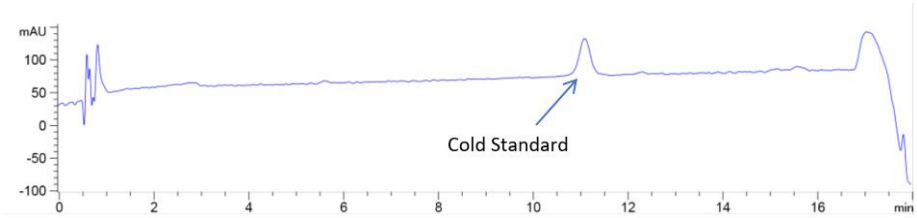

Figure 3.22: UV(254) trace of [^{18}F]MGS2

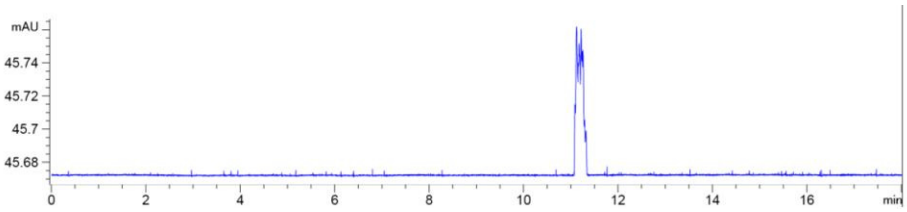

Figure 3.23: gamma trace of [^{18}F]MGS2

[^{18}F]MGS3

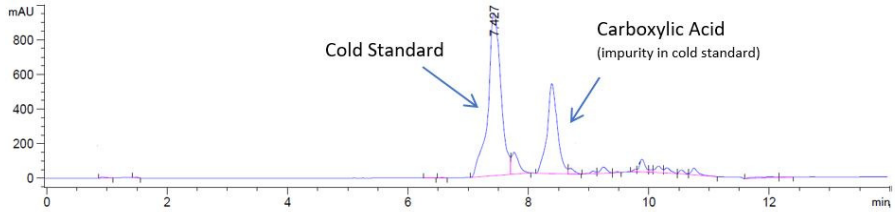

Figure 3.24: UV(254) trace of [^{18}F]MGS3

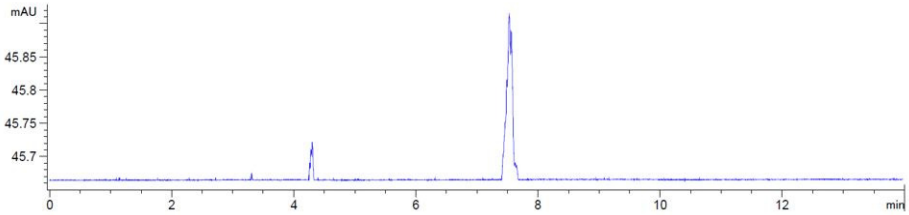

Figure 3.25: gamma trace of [^{18}F]MGS3

3.4.3 Biochemistry

HDAC Inhibition Assay

The assays were carried out at the Broad Institute. All recombinant human HDACs were purchased from BPS Bioscience. The substrates, Broad Substrates A and B, were synthesized in house. All other reagents were purchased from Sigma-Aldrich. Caliper EZ reader II system was used to collect all data. HDAC inhibition assays: Compounds were tested in a 12-point dose curve with 3-fold serial dilution starting from 33.33 μM. Purified HDACs were incubated with 2 μM (the concentration is kept the same for all the HDACs, below K_m of substrate) carboxyfluorescein (FAM)-labeled acetylated or trifluoroacetylated peptide substrate (Broad Substrates A and B, respectively) and test compound for 60 min at room temperature, in HDAC assay buffer that contained 50 mM HEPES (pH 7.4), 100 mM KCl, 0.01% BSA, and 0.001% Tween-20. Reactions were terminated by the addition of the known pan HDAC inhibitor LBH-589 (panobinostat) with a final concentration of 1.5 μM. Substrate and product were separated electrophoretically, and fluorescence intensity in the substrate and product peaks were determined and analyzed by Labchip EZ Reader. The reactions were performed in duplicate for each sample. IC_{50} values were automatically calculated by Origin8 using 4 Parameter Logistic Model. The percent inhibition was plotted against the compound concentration, and the IC_{50} value was determined from the logistic dose-response curve fitting by Origin 8.0 software.

Thermal Shift Assays

Lysate from the dorsolateral prefrontal cortex of three donors was adjusted to 2 mg·mL^{-1} total protein, pooled and split into 115 µL aliquots. 1% of the total volume DMSO containing increasing amounts of [^{12}C] Martinostat or [^{19}F]MGS3 were added (0, 3.2, 16, 80, 400 nM, 2.0, 10 μM final concentration). The lysate was incubated with inhibitor at room temperature for 30 min under inversion. The aliquots were divided into 50 μL samples and heated to 55 °C or 60 °C respectively for 3 min, and cooled to room temperature for 3 min. Input aliquots with 1% DMSO were kept at room temperature. All samples were immediately centrifuged for 20 min (18000 x g, 4 °C) and the supernatants collected. 3 x SDS loading buffer containing 125 mM DDT was added and samples were heated to 90 °C for 10 min. Samples heated to 55 °C were used for HDAC1/2/6/8 western blots, 60 °C were used for HDAC3 western blots.

Chemoproteomics

Tissue Lysis

Postmortem frozen human brain tissue was obtained from the Harvard Brain Tissue Resource Center, University of Miami Brain Endowment Bank, Human Brain and Spinal Fluid Resource Center and Brain Tissue Donation Program at the University of Pittsburgh Medical Center through the National Institute of Health (NIH) NeuroBioBank. Informed consent was obtained from next to kin for all donors. None of the donor brains had abnormal neuropathy diagnoses. Tissue from cerebellum or dorsolateral prefrontal cortex was weighed in a precooled Eppendorf tube and sus-

pended in lysis buffer (PBS, 150 mM NaCl, 0.15% NP-40, Roche protease inhibitor (04693159001), 1% casein) at 200 mg·mL^{-1} and homogenized with an electric pestle homogenizer for 60 seconds. Another volume of lysis buffer was added and the lysate was sonicated on ice in 3 second pulses for 30 seconds at 10% power (Fisher Scientific Model CL-18). After 30 min rotation at 4 °C, the lysate was centrifuged for 20 min at a rotation of 18.000 g at 4 °C. The supernatant was collected and the total protein concentration was determined using a bicinchoninic acid (BCA) assay (Pierce 23227). If donors were pooled, the concentration was adjusted with lysis buffer before combining the lysates.

Pull-down assays

Thermo Fisher Dynabeads MyOne Streptavidin C1 (100 µL, 1mg) were immobilized on a magnetic stand, the supernatant removed, the beads washed with 100 µL PBS and resuspended in the same volume. Biotinylated hydroxamate X stock solution (300 µM, 20 µl, 2.12 µg, 6 nm, ca. 2000 x bead capacity) as added and incubated with inversion at room temperature for 30 min. The supernatant was removed, the beads were washed again with 100 µL PBS and resuspended in 100 µL PBS.

For competition experiments, the lysate was preincubated for 30 min at room temperature with an appropriate concentration of competitor. The lysate (200 μL) was added to the beads and either incubated for 2 h at room temperature or overnight at 4 °C on the rotator. The beads were washed 3 times with 100 μL wash buffer (PBS, Roche protease inhibitor (04693159001) and a fourth time with 100 μL PBS. For western blot, the beads were resuspened in 60 μL SDS loading dye, boiled for 10

min at 90 °C and stored at -80 °C until analysis. For chemoproteomic analysis, the samples were covered with 20 μL PBS, stored at -80 °C and submitted to the Broad Institute for processing.

Western Blotting

Protein separation was accomplished on a Criterion Stain-Free 4-20% gel (Biorad 567-8095) at 200 V for 50 min. Protein transfer onto a low fluorescence PVDF membrane (Biorad 62-0264) was performed at 0.14 A for 60 min. Gel and membrane imaging for quality control was conducted with a Chemidoc XRS system (Biorad 170-8264). Membranes after transfer were treated with Tris buffered saline/Tween 20 (TBST, 0.1% Tween 20) with 5% blocker (Biorad 170-6404) overnight at 4 °C. The following steps were then carried out at room temperature. The membrane was washed with TBST, incubated with primary antibody solutions (1% blocker in TBST with appropriate dilution of antibody: HDAC1: Thermo Fisher PA1-860 1:5000, HDAC2: Abcam ab124974 1:5000, HDAC3: Abcam ab32369 1:5000, HDAC6: Santa Cruz sc11420 1:5000, HDAC8: Abcam ab187139 1:5000, , LSD1: Cell Signaling #2184 1:4000, HDAC10: abcam ab108934 1:4000) for 1 h, washed with TBST, incubated with secondary antibody (1% blocker in TBST with appropriate dilution of antibody: anti-rabbit-HRP: Cell Signaling #7074S 1:5000, anti-mouse-HRP: Cell Signaling #7076S 1:5000) for 1h, washed with TBST and TBS and developed with ECL prime western blotting reagent (GE RPN2232) and imaged with a Chemidoc XRS system with Image Lab 5.2.1.

Images were exported as 600 dpi Tif files and processed in Image J as 8-bit images. Background was substracted and Gaussian smooting with a 50 pixel radius was applied. Images were inverted and the measurement tool was used to quantify band intensity.

3.4.4 Imaging

Animal Preparation

RODENT A total of 12 male Sprague-Dawley rats (Charles River Labs) between 2 and 4 months of age were used for imaging. Animals were pair-housed until they reached a weight of 500 g, and were kept on a 12 h : 12 h light:dark cycle. All treatment and imaging experiments were performed according to procedures approved by the Institutional Animal Care and Use Committee at the Massachusetts General Hospital. Anesthesia consisting of isoflurane (3% for induction, 2% for maintenance) and oxygen carrier was administered to each animal. For i.v. administration, a catheter was placed in a lateral tail vein of each animal. The catheter was connected to a syringe via an extension line. Animals received a bolus injection of either vehicle (1:1:8 DMSO:Tween80:saline) or blocking agent in solution (1 $mg{\cdot}mL^{-1}$, 1 $mg{\cdot}kg^{-1}$ in 1:1:8 DMSO:Tween80:saline) immediately prior to injection of the radiotracer.

NHP Four baseline PET/MR studies were carried out with two baboons (both females, *Papio anubis*, 13.4 and 16.2 kg) as approved by the Institutional Animal Care and Use Committee at the Massachusetts General Hospital. *Nil per os* was instructed 12 h prior to the study. Anesthesia was induced with intramuscular (i.m.) ketamine (10 $mg{\cdot}kg^{-1}$) and xylazine (0.5 $mg{\cdot}kg^{-1}$). Anesthesia was continued during the study

with 1-1.5% isoflurane in medical oxygen and ketamine/xylazine effects were reverted with yobine (0.11 mg·kg^{-1}, i.m.) prior to the scan. Radiotracer injection was performed through a catheter in the saphenous vein. Vital signs (end-tidal CO_2, oxygen saturation, heart rate, and respiration rate) were under continuous surveillance to maintain a normal physiological range, documented every 15 minutes.

Image Acquisition

RODENT After injection of a radiotracer bolus (669±15 μCi [^{11}C]Martinostat; 305±5 μCi [^{18}F]MGS1; 103±4 μCi [^{18}F]MGS2; 67±1 μCi [^{18}F]MGS3), a 120 min dynamic PET scan was acquired for each animal. For blocking experiments, an appropriate volume of a solution of 1 mg·mL^{-1} of blocking compound in 10% DMSO/10% Tween80/80% saline was injected to reach 1 mg·kg^{-1} animal weight, immediately prior to radiotracer injection. PET scans were performed on either a GammaMedica Triumph PET/CT/SPECT scanner or Siemens P4 PET scanner. PET data collected on the GammaMedica Triumph was corrected for attenuation with the corresponding CT image, which was acquired immediately following the PET scan. On the P4 scanner, a transmission scan with a Cobalt (^{57}Co) line source was acquired to generate an attenuation map, which was applied during image reconstruction. The dynamic PET data was binned into 38 or 44 timeframes (8 x 15 s, 8 x 1 min, 10 x 2 min, 18 x 5 min or 6 x 5 min and 6 x 10 min) and reconstruction of each frame via an iterative MLEM (maximum likelihood expectation maximization) algorithm, consisting of 16 iterations, afforded images with a resolution of approximately 2 mm FWHM (full width at half maximum).

NHP PET/MRI acquisition was performed on a 3T Siemens TIM-Trio with a Brain-PET insert (Siemens, Erlangen, Germany). A PET/MRI compatible eight-channel array coil customized for nonhuman primate brain imaging to increase image signal and quality was employed. After administration of one of the radiotracers (1.4 mCi MGS1; 1.8 mCi MGS2; 0.55 mCi MGS3) or [^{11}C]Martinostat (4.9 mCi), dynamic PET image acquisition was initiated. Dynamic PET data were collected and stored in list mode for 90 min in the case of [^{11}C]Martinostat and 120 min for [^{18}F]MGS1-3. Image reconstruction was performed using the 3D ordinary Poisson expectation maximization algorithm with detector efficiency, decay, dead time, attenuation, and scatter corrections. PET data were binned in 29 frames (6 x 10 s, 6 x 20 s, 2 x 30 s, 1 x 1 min, 5 x 5 min, 9 x 10 min for ^{18}F scans (6 x 10 min for [^{11}C]Martinostat)). Image volumes were eventually reconstructed into 76 slices with 128x128 pixels and a 2.5 mm isotropic voxel size. 30 minutes after scanner start, a high-resolution anatomical scan using multiecho MPRAGE sequence (TR = 2530 ms, TE1/TE2/TE3/TE4 = 1.64/3.5/5.36/7.22 ms, TI = 1200 ms, flip angle = 7°, and 1 mm isotropic) was acquired.

Image Analysis

RODENT The imaging software package PMOD 3.3 (PMOD Technologies, Zurich, Switzerland) was used for all image analysis. All PET imaging data acquired on the Triumph scanner were coregistered to the CT image acquired from the same animal. Siemens P4 data were aligned and coregistered to CT data derived from an age matched animal of similar size. For maximum consistency, the data were coregistered

to the Schiffer Px Rat [178] rat brain template and data was derived from a whole brain VOI for time activity curves.

NHP PET data were registered to the Black baboon brain atlas [172] using JIP tools optimized for nonhuman primate data processing (www.nitrc.org/projects/jip). The high-resolution T1-weighted anatomical MRI image was first registered to the baboon brain atlas using a mutual information approach and the transformation parameters were then applied to the simultaneously collected dynamic PET data. 38 common VOIs from the Black baboon atlas [172] were applied to all scans. TACs were extracted from the orbitofrontal cortex, dorsolateral prefontal cortex, anterior cingulate gyrus, posterior cingulate gyrus, amygdala, hippocampus, ventral caudate, caudate body, putamen, nucleus accumbens, medial and ventral posterolateral thalamus, habenula, cerebellar midline nuclei, whole cerebellum, genu and splenium of the corpus callosum, striate cortex, motor cortex, supplementary motor area and the centrum semiovale. Symmetrical structures were averaged before further analysis. For SUV calculations, time points between 30 and 60 min were averaged for each tracer and each VOI. Spearman correlation coefficients, R^2 values and P values were determined using linear regression within Microsoft Excel.

Regional SUV analysis in NHP brain

Regions specified in Table 3.2 are based on Black baboon atlas [172] and averaged if they appear bilaterally. Treatment of data as described in Marterials and Methods section. Graphic comparison of Martinostat with each ^{18}F-radiotracer is depicted in Figure 3.9

Table 3.2: SUV values for different brain regions in baboon brain for different radiotracers

Region	**[^{11}C]MStat**	**[^{18}F]MGS1**	**[^{18}F]MGS2**	**[^{18}F]MGS3**
Orbitofrontal Ctx	2.69	0.507	1.34	1.86
DLPFC	2.91	0.602	1.44	2.43
Cingulate-anterior	2.78	0.724	1.53	2.26
Cingulate-posterior	2.83	0.718	1.48	2.27
Amygdala	2.53	0.567	1.33	1.96
Hippocampus	2.67	0.758	1.42	1.95
ventral caudate	3.23	0.626	1.31	2.16
body caudate	2.97	0.543	1.46	2.22
Putamen	3.41	0.592	1.61	2.73
Accumbens	3.01	0.611	1.46	2.25
MD thalamus	3.26	0.794	1.75	2.65
VPL thalamus	2.92	0.617	1.59	2.19
Habenula lateral	3.09	0.842	1.78	2.04
Midline CB nuclei	3.89	0.939	1.79	2.75
Cerebellum	3.25	0.740	1.69	2.61
Corpus Callosum genu	2.38	0.624	1.34	1.73
striate cortex	3.28	0.842	1.45	2.51
motor upper extremity	2.60	0.469	1.41	2.10
motor face	2.92	0.493	1.66	2.36
SMA	2.72	0.786	1.62	2.47
Corpus callosum splenium	2.08	0.543	1.08	1.88
centrum semiovale	1.84	0.417	0.989	1.44

Chapter 4

Imaging HDAC6 with positron emission tomography

The contents of this chapter are currently prepared for submission. Wen Ning Zhao and Peter Chindavong prepared treated iPS cells, AJ Campbell and Florence Wagner conducted molecular modeling with HDAC6, Misha Riley assisted with autoradiography experiments. Tom Morin assisted with coregistration and blood data analysis for NHP imaging experiments. Yvonne Klingl carried out the syntheses of PEGylated hydroxamate probes and optimized pull-down experiments under my supervision. Monica Schenone and her team carried out mass spectrometry and data analysis at the Broad institute. Tonya Gilbert developed HDAC CETSA protocols and assisted me with data acquisition.

4.1 Development of an HDAC6 selective imaging agent

4.1.1 Inhibitor design

While we demonstrated in Chapter 2 and 3 how targets can motivate and accelerate method development, in this Chapter we will showcase how a versatile toolbox can increase the rate of tracer development. With Martinostat and MGS3 as the groundwork, we were interested in more selective imaging agents that would be able to discern the various HDAC subtypes and yield information about single relevant isoform distribution, such as HDAC6. As discussed earlier, a fair amount of medicinal chemistry has demonstrated strategies to engineer selectivity for HDAC6. However, simply selectivity is not sufficient to constitute a good PET radiotracer, particularly with neuroimaging applications in mind. Brain penetrance and non-specific binding are the most common reasons for tracer development failures with molecules that look very promising before the actual imaging experiment. While attempts have made, it is extremely difficult to predict the two parameters without radiolabeling the molecule and studying it in vivo. Since many molecules can be selective and look promising, frameworks have been developed to prioritize tracer candidates without experimental attempts to predict brain penetrance and non-specific binding. An example is the Multi Parameter Optimization score (MPO) developed by Pfizer [179]. Using a set of known compounds, calculated physical properties such as cLogP and TPSA can be weighted and combined into a single number that describes the likelihood of a molecule to perform well in a given task. The weight given to each parameter can vary based on the target application, and measures like a "CNS MPO" can be estab-

lished to predict the likelihood of success of a small molecule to perform well as a PET tracer in CNS imaging.

Along with other parameters, like predicted metabolic liability, passive diffusion rate and protein binding, a multidimensional analysis can be useful to prioritize candidate molecules for radiolabeling. We used a set of 6 molecules known in the literature or derivatives with minor modifications as a starting point for the development of an HDAC6 tracer. The molecules we chose all bear a handle that can be used for radiolabeling. (Figure 4.1).

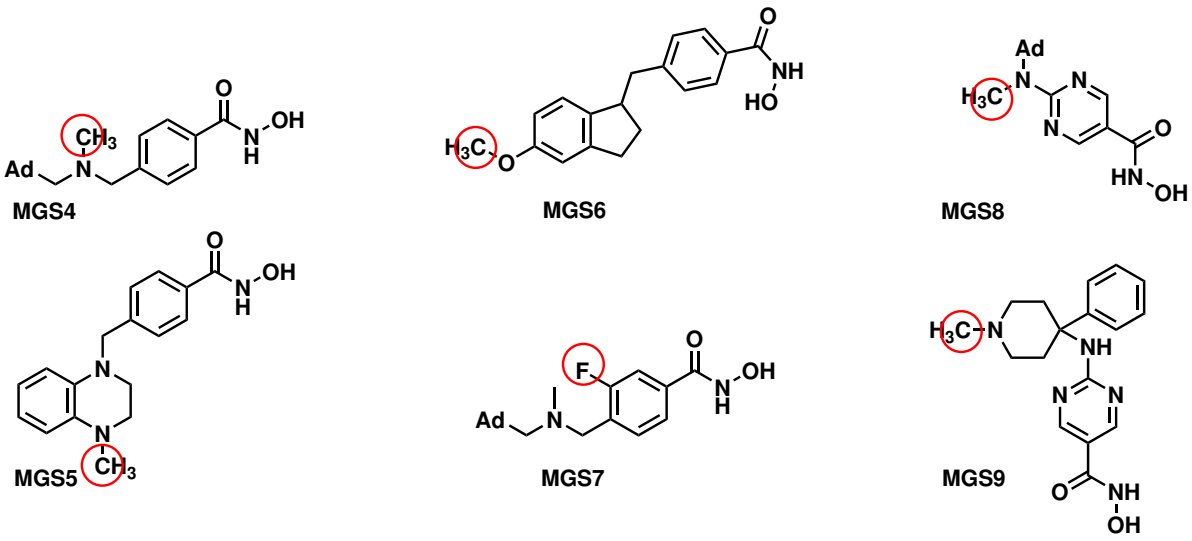

Figure 4.1: selected candidate molecules with predicted HDAC6 selectivity and a radiolabeling site marked with a red circle

The molecules were arranged according to their calculated MPOs and protein binding ratio in a 2D-grid. As a rule of thumb, Pfizer suggests that candidates in the upper right quadrant are promising candidates, whereas the lower left quadrant suggests a low chance of success. For comparison, molecules encountered in Chapter 3 were added to the grid. It quickly becomes apparent that for class-I HDAC imaging

agents, the strategy is predictive in retrospect: MGS3 and Martinostat rank in the top quadrant, MGS1 and 2 do not, but are not predicted to perform poorly either. As expected, an absolute comparison of respective performance is not reflected in the grid.

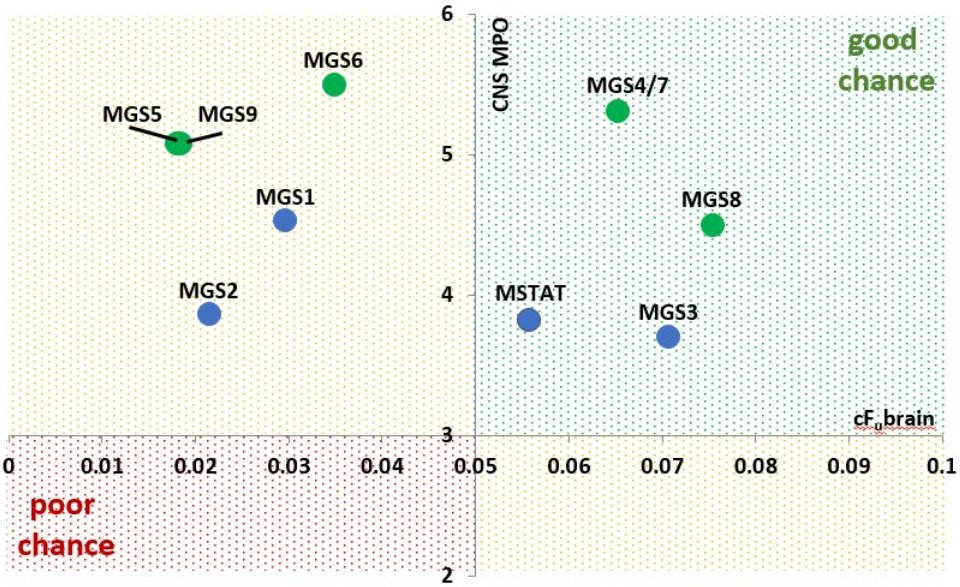

Figure 4.2: Predicting a tracer: two-dimensional representation of molecular property scores, y-axis represents the MPO score, the x-axis represents the predicted plasma protein binding fraction

Several strategies exist to achieve selectivity for HDAC6 over other HDAC isoforms with hydroxamate inhibitors. These include the use of 1) large polycyclic capping groups [109, 180, 181], 2) a substituted sp^2 hybridized α-carbon [110], 3) sterically demanding substitution close to the chelating group [107, 108]. Based on these strategies and combined with our experience in PET radiotracer design for HDACs [146, 149, 150, 182], we developed a small library of potential CNS-penetrant HDAC6 inhibitors. (Figure 4.1 Of these, MGS7, which we then renamed Bavarostat, emerged as unique. In Figure 4.3), the structure of Bavarostat is shown docked to the

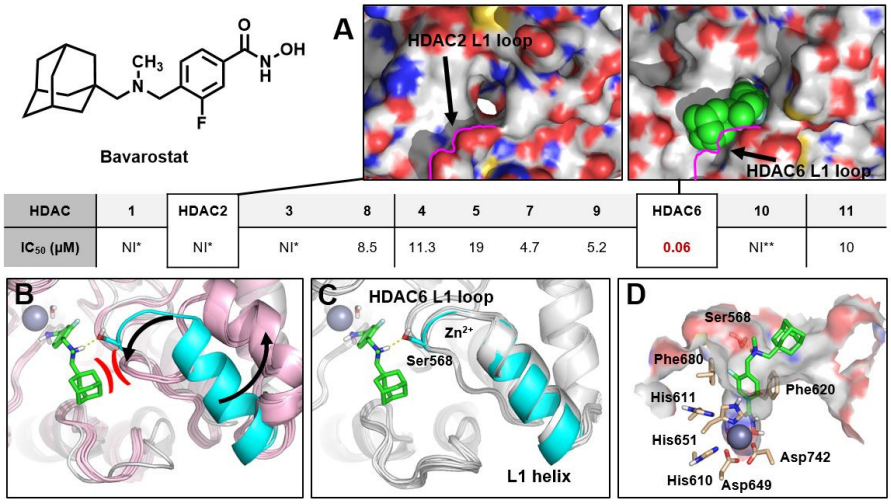

Figure 4.3: Selective inhibition of HDAC6 by Bavarostat, docking analysis and IC_{50} Recombinant enzyme inhibition assays were used to determine IC_{50} values for all Zn-dependent HDAC isoforms. A hHDAC6 CD2 surface view (left) and hHDAC2 surface view (right). Pink line represents the edge of the L1 loop segment of hHDAC2. B Bavarostat docked into HDAC6. C Alignment of hHDAC6 (white and cyan protein) with Bavarostat and zHDAC6 (white protein) showing similar L1 loop segment conformations. D Alignment of hHDAC6 (white and cyan) and hHDAC2.

CD2 catalytic domain of human HDAC6, exemplifying the contribution of structural elements to the selectivity over HDAC2.

While no polycyclic capping group in the traditional sense is present in Bavarostat, the adamantyl residue is predicted to fill a hydrophobic surface groove present in HDAC6. However, in HDAC2 as a representative for class-I HDACs, the groove in inaccessible due to the changed conformation of the rigid L1 loop segment and the neighboring α-helix (Figure 4.3A,B). Ser568 on the same loop forms a hydrogen bond with the tertiary amine of Bavarostat, which is disrupted as well by the different conformation (Figure 4.3C). The rigidity introduced by an sp^2-hybridized α-carbon atom in Bavarostat prevents an effective κ^2-binding mode of the hydroxamate. High-resolution crystallographic data shows that HDAC6 selective inhibitors bind to the Zn ion in the HDAC6 active center via an additional water molecule [111], which has not been observed in the binding of other HDAC isoforms with non-selective HDAC inhibitors. The presence of this water molecule greatly improved the fit of Bavarostat to the protein (Figure 4.3D), suggesting that the rigid phenylene-moiety is indeed conveying additional HDAC6 selectivity. Beyond the aspect of rigidity, π-stacking interactions occur with Phe620. Sterically demanding architecture has been employed as a source of selectivity. The width of access tunnels to the HDAC active center is significantly enlarged in HDAC6, so that sterically demanding molecules simply wouldn't fit other isoforms. With imaging applications in mind, an aryl fluoride was also added in a position previously determined to have minimal functional impact on similar inhibitors [182]. Interestingly, the fluoride substituent extends into a small nook within the entry tunnel, adding additional Van-der-Waals interaction.

In summary, the structure of Bavarostat confirms the validity of individual factors contributing to HDAC6 selectivity.

4.1.2 In vivo functional selectivity

HDAC6 is unique among other HDACs with respect to its exclusively cytosolic location and, as a result, its protein substrates [100,183,184]. Most prominently α-tubulin and HSP90 are deacetylated by HDAC6, while nuclear proteins such as histones 3 and 4 (H3, H4) remain unaltered [101, 183]. On a functional level, inhibition of HDAC6 should therefore increase the amount of acetylated α-tubulin while leaving histone acetylation unchanged. To confirm the high selectivity suggested by the IC_{50} values in Figure 4.3, we determined the acetylation levels of a known substrate and two non-substrates of HDAC6 in a human neuroprogenitor cell line, derived from iPSCs which were generated from a healthy fibroblast cell line (GM08330) [150]. Treatment with Bavarostat in comparison to other HDACi tool compounds at 10 μM for 6 h and quantification of the acetylation state of α-tubulin and histones (specifically H3K9 and H4K12) confirmed the selectivity for HDAC6 on a functional level. (Figure 4.4) Tubastatin A and ACY1215 have both been shown to inhibit HDAC6. Both compounds increase the amount of cellular acetyl-α-tubulin, while a class-I selective HDAC inhibitor, CI-994 does not increase tubulin acetylation. Bavarostat also increases the amount of cellular acetyl tubulin, supporting its engagement with HDAC6. Histone acetylation remains unaltered in cells treated with Bavarostat, as it does for the highly HDAC6 selective agent Tubastatin A. ACY1215 has poor selectivity for

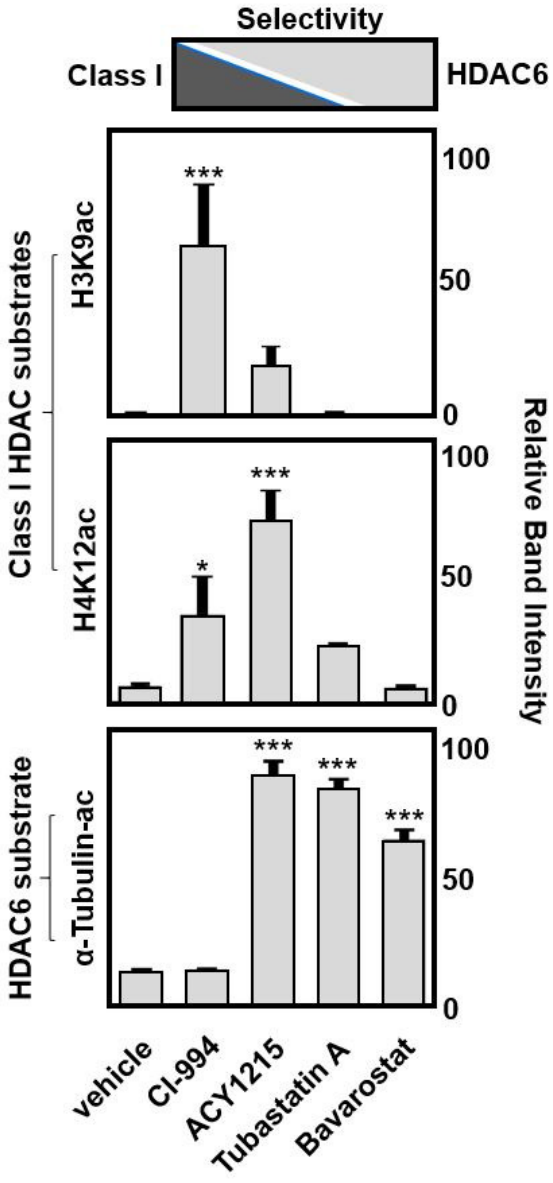

Figure 4.4: *In vivo* functional selectivity for HDAC6 Histone 3 (Lysine 9), Histone 4 (Lysine 12) and α-Tubulin protein acetylation levels in IPS neuroprogenitor cells after treatment with Bavarostat, a class-I HDAC inhibitor (CI-994), a HDAC6 selective inhibitor (Tubastatin A) and a mixed selectivity inhibitor (ACY1215), in comparison to untreated cells, indicating functional HDAC6-selectivity for Bavarostat

HDAC6, leading to significantly increased acetylation of H4K12 through inhibition of other HDAC isoforms. Histone acetylation on both H3K9 and H4K12 is significantly increased in cells treated with CI-994.

In conclusion, the changes in cellular protein acetylation in response to HDACi treatment confirm the functional selectivity of Bavarostat for HDAC6.

4.1.3 Evaluation of [^{18}F]Bavarostat as an HDAC6 radiotracer

Radiochemical synthesis

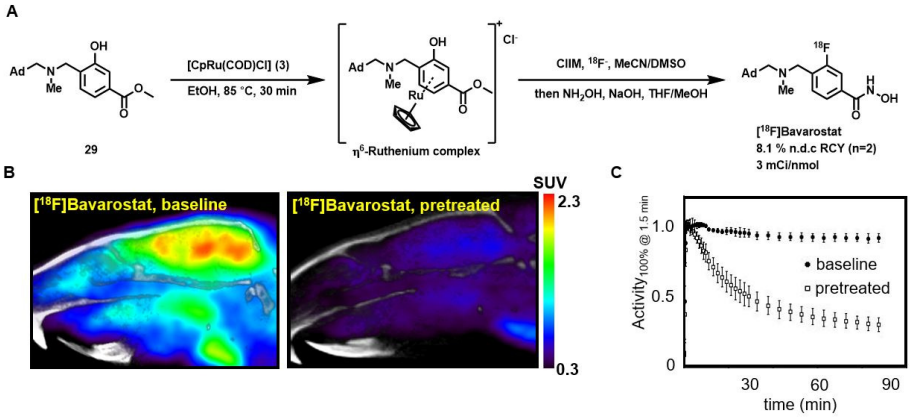

Figure 4.5: Rodent PET imaging with [^{18}F]Bavarostat a) Radiochemical synthesis of [^{18}F]Bavarostat via Ruthenium mediated deoxyfluorination, ClIM = *N,N*-bis(2,6-diisopropylphenyl)-1-chloroimidazolium chloride; b) averaged (n=3) time-activity curves of a whole-brain ROI of Sprague-Dawley rats injected with [^{18}F]Bavarostat. In the blocked animals, 1.0 mg·kg^{-1} of unlabeled Bavarostat was injected immediately prior to radiotracer administration, baseline animals treated with vehicle b) representative sagittal slices summed from 30-90 minutes

Radiolabeling of hydroxamic acids, particularly scaffolds like Bavarostat, has been difficult to achieve. Routes were lengthy, inefficient, low-yielding and notoriously difficult to automate [182]. Enabled by innovative ruthenium-mediated radiofluori-

nation described in Chapter 2 (Figure 4.5), a highly efficient radiosynthesis afforded [^{18}F]Bavarostat in high yield and high specific radioactivity (Figure 4.5). Using an air-stable Ruthenium-complex **1**, the labeling precursor **29** was converted into an η^6-coordinated Ruthenium phenol complex solution and served without further purification to elute [^{18}F]fluoride off an anion exchange cartridge with 83% elution efficiency. Within 30 minutes at 130 °C, the labeling proceeds with high conversion (> 70% radiochemical conversion). Subsequent transacylation in the same pot afforded [^{18}F]Bavarostat in 8.1% (n=2) overall non-decay corrected radiochemical yield and high specific activity (3 mCi·nmol^{-1} at end of synthesis) after HPLC purification and reformulation.

Rodent imaging

To evaluate the potential of [^{18}F]Bavarostat to serve as an HDAC6 radiotracer, PET imaging in rodents was performed. The compound was administered to Sprague-Dawley rats and the dynamic PET data was acquired. As shown in the time-activity curves in Figure 4.5, the compound exhibits excellent brain uptake and retention. Treatment of the animals with non-radioactive Bavarostat at 1 mg·kg^{-1} led to solid blocking of brain uptake, indicative of specific binding. Unfortunately, standardized uptake values (SUVs) were not stable across studies, while the general shape of the time activity curve was highly reproducible. The curves were therefore normalized to 100% at t = 2 min to compare the outcome of several replicates. More work to determine an appropriate input function will be needed to appropriately model the tracer kinetics for more in-depth analysis.

Autoradiography

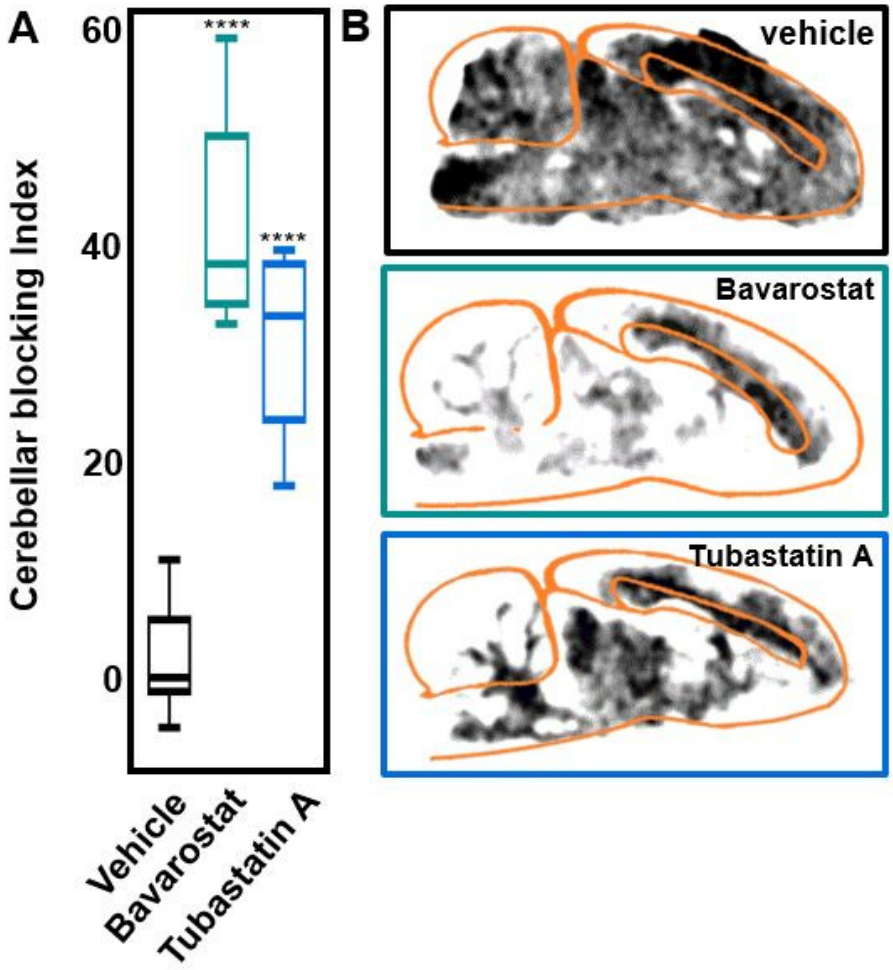

Figure 4.6: Autoradiography with [^{18}F]Bavarostat a) Signal intensity of cerebellum relative to corpus callosum at baseline and in sagittal slices of Sprague-Dawley rat brain pretreated with 10 μM Bavarostat or Tubastatin A respectively; Blocking index = 1 – $[(PT_{CB} \cdot PT_{CC}^{-1}) \cdot (BL_{CB} \cdot BLCC^{-1})^{-1}$, PT = pretreated, BL = vehicle treatment, CB = cerebellum, CC = corpus callosum. ****P<0.0001 b) Representative sagittal slices of Sprague-Dawley rat brains pretreated with vehicle, 10 μM Bavarostat or Tubastatin A respectively;

In vivo blocking studies were inconclusive due to the poor brain penetrance of known HDAC6 selective inhibitors. To circumvent the issue of blood brain barrier pene-

trance, selectivity of the probe in brain tissue was demonstrated using autoradiography. (Figure 4.6) Slices of rat brain tissue were exposed to [^{18}F]Bavarostat in the presence of [^{19}F]Bavarostat or Tubastatin A. At 10 μM [^{19}F]Bavarostat, binding was reduced by almost 40% in the cerebellum, relative to corpus callosum, a region of high non-specific binding. Tubastatin A, a highly HDAC6 selective compound, reduced the amount of bound radioactivity to a comparable level as Bavarostat. These data indicate that the binding to brain tissue occurs with selectivity for HDAC6.

NHP imaging

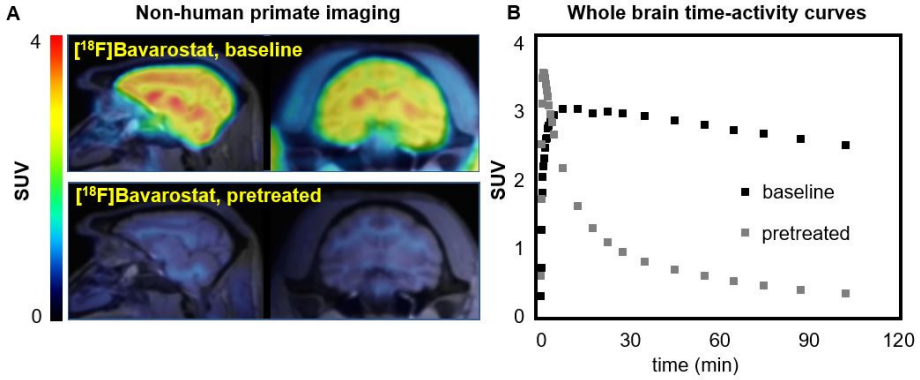

Figure 4.7: Non-human primate imaging with [^{18}F]Bavarostat a) sagittal and coronal slices of PET images acquired with [^{18}F]Bavarostat in the baboon brain, baseline and pretreated with 1.0 mg·kg^{-1} unlabeled Bavarostat (averaged 60-120 min); b) Whole-brain SUV time activity curves of [^{18}F]Bavarostat in baboon brain, baseline and pretreated with 1.0 mg·kg^{-1} unlabeled Bavarostat

To assess the translational potential of [^{18}F]Bavarostat for human imaging, the tracer properties were assessed in baboon (*Papio* anubis) through a series of preliminary experiments. (Figure 4.7) The molecule exhibits excellent brain uptake, with a whole-brain standard uptake value of 3 around 30 minutes after tracer injection and high

retention of signal over time. The uptake of [^{18}F]Bavarostat is particularly high in subcortical areas and low in white matter, distinct from other HDAC imaging agents assessed in NHPs [142,144,145,149–151,182] (Figure 4.8). Particularly noteworthy is

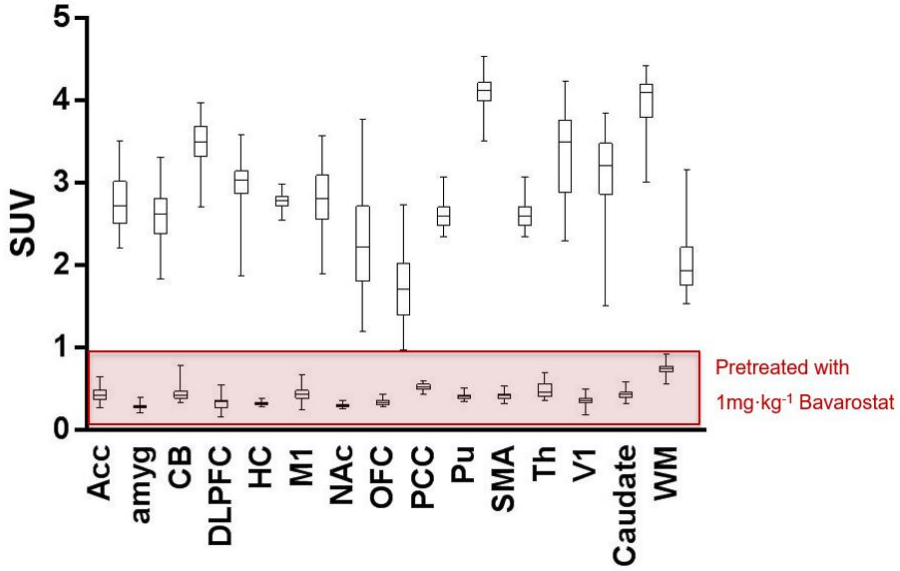

Figure 4.8: SUV analysis of voxel SUV distribution within ROIs Analysis of 15 regions within the baboon brain using the black baboon atlas, comparison of baseline and pretreated distribution. Each region of interest (ROI) is shown as a distribution of SUV values of each voxel within the ROI. ACC = Anterior cingulate cortex, amgyg = amygdala, CB = cerebellum, DLPFC = dorsolateral prefrontal cortex, HC = hippocampus, M1 = primary motor area, NAc = Nucleus accumbens, OFC = orbitofrontal cortex, PCC = posterior cingulate cortex, Pu = putamen, SMA = supplementary motor area, Th = Thalamus, V1 = primary visual cortex, WM = white matter

the low amount of non-specific binding observed after pre-treatment with 1mg·kg^{-1} nonlabelled Bavarostat, and the localization of the residual signal mostly to white matter, which is also observed in autoradiography (Figure 4.6). An investigation of *in vivo* metabolism and kinetic modeling of [^{18}F]Bavarostat binding is currently ongoing. In a preliminary analysis, a good correlation was obtained between standardized uptake values (SUVs) and distribution volume (V_T) derived by Logan plot from an

arterial plasma input function (Figure 4.9). In summary, the NHP imaging data are

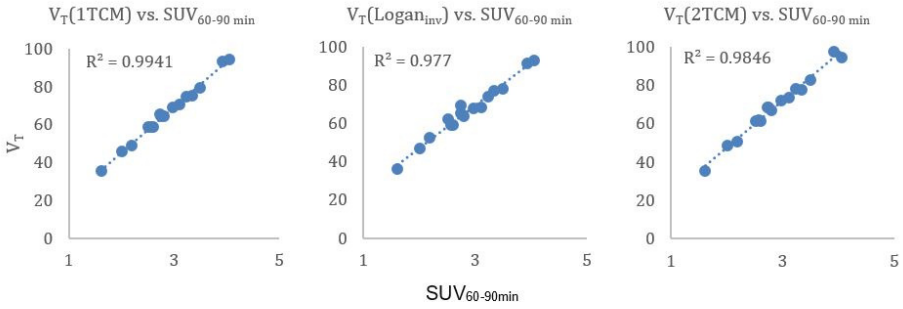

Figure 4.9: Correlation of $SUV_{60-90min}$ with V_T determined by 1- or 2-tissue compartment model or invasive Logan plot with an arterial plasma input function

promising and warrant translation of [^{18}F]Bavarostat to human HDAC6-imaging.

4.1.4 Conclusion

Bavarostat has been shown to selectively inhibit HDAC6 in recombinant and *in vivo* assays. Radiolabeling of [^{18}F]Bavarostat was possible with innovative radiofluorination, and in vivo imaging demonstrated the high brain uptake of the molecule. Its engagement of HDAC6 was confirmed by autoradiography. The molecule shows great promise as a radiotracer in rodent and non-human primate models and is expected to enable the study of HDAC6 in the living human brain.

4.2 Experimental

4.2.1 Chemical synthesis

Materials and methods

All air- and/or moisture-sensitive reactions were performed under an inert atmosphere of nitrogen or argon with standard Schlenk and glovebox techniques. Solvents Tetrahydrofuran was distilled from deep purple sodium benzophenone ketyl. Dry DMF and dry DMSO were purchased from Acros Organics. Other anhydrous solvents (acetonitrile, diethyl ether, dichloromethane, pentane, and toluene) were obtained by filtration through drying columns on an mBraun system. Chromatography Thin layer chromatography (TLC) was performed by EMD TLC plates pre-coated with 250 m thickness silica gel 60 F_{254} plates and visualized by fluorescence quenching under UV light and $KMnO_4$ stain. Flash chromatography was performed with silica gel (230-400 mesh) purchased from Silicycle Inc., or, where stated, with spherical silica gel cartridges (ZIP sphere) from Biotage with an Isolera purification system. Spectroscopy and Instruments NMR spectra were recorded on either a Varian Unity/Inova 600 spectrometer operating at 600 MHz for 1H acquisitions, a Bruker 500 spectrometer or a Varian Unity/Inova 500 spectrometer, both operating at 500 MHz, 471 MHz and 126 MHz for ^{1}H, ^{19}F and ^{13}C acquisitions, respectively, or a Varian Mercury 400 spectrometer operating at 375 MHz for ^{19}F acquisitions. Chemical shifts are reported in ppm with the solvent resonance as the internal standard (^{1}H: Chloroform-d, 7.26; DMSO-d_6, 2.50), (^{13}C: Chloroform-d, 77.16; DMSO-d_6, 39.52). Data is reported as follows: s = singlet, d = doublet, t = triplet, q = quartet, m = multiplet; coupling

constants in Hz; integration.

Methyl-3-hydroxy-4-(hydroxymethyl)benzoate (30)

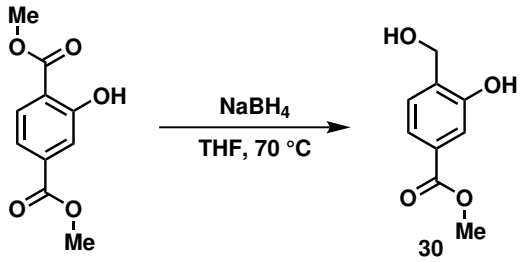

To a solution of dimethyl hydroxyterephthalate (500 mg, 2.38 mmol, 1.00 eq) in 5 mL THF was added sodium borohydride (180 mg, 4.76 mmol, 2.00 eq) and the suspension was heated at reflux (70 °C) for 2 h. The solvent was removed in vacuo and 5 mL of water were added to the residue. The solution was acidified with 1M HCl and stored at 0 °C until crystallization was observed. The solid was isolated by filtration. The product was purified by column chromatography. The product (368 mg, 2.02 mmol, 84.9 %) was obtained as a white solid.

$\mathbf{R}_f$ = 0.11 (EtOAc in hexanes = 25%).

NMR Spectroscopy:

^{1}**H NMR** (600 MHz, DMSO-d_6, δ) 9.83 (s, 1H), 7.42 (dt, J = 3.3, 1.9 Hz, 2H), 7.36 (q, J = 1.6 Hz, 1H), 5.16 (s, 1H), 4.51 (s, 2H), 3.81 (dd, J = 2.2, 1.1 Hz, 3H).

^{13}**C NMR** (600 MHz, DMSO-d_6, δ) 9.83 (s, 1H), 7.42 (dt, J = 3.3, 1.9 Hz, 2H), 7.36 (q, J = 1.6 Hz, 1H), 5.16 (s, 1H), 4.51 (s, 2H), 3.81 (dd, J = 2.2, 1.1 Hz, 3H).

HRMS(m/z) calc'd for $C_9H_{10}O_4$ $[M+Na]^+$, 205.0471; found, 205.0471.

Methyl-4-formyl-3-hydroxybenzoate (31)

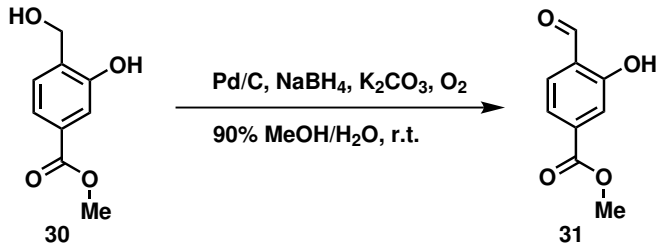

To a solution of **30** (250 mg, 1.37mmol, 1.00 eq) in 3 mL 10% aqueous methanol was added Pd/C (73 mg, 10% loading, 0.034 mmol, 2.5 mol%), potassium carbonate (567 mg, 4.11 mmol, 3.00 eq) and sodium borohydride (5.2 mg, 0.14 mmol, 0.10 eq) and the mixture was stirred under an atmosphere of oxygen over night. Then, the mixture was diluted with dichloromethane and filtered. The solution was concentrated in vacuo, partitioned between ethyl acetate and water, the aqueous layer extracted two more times with ethyl acetate and the combined organic phases were dried over sodium sulfate. The solvent was removed under reduced pressure and the product was purified by column chromatography. Aldehyde **31** (92 mg, 0.51 mmol, 37%) was obtained as a white solid

$\mathbf{R}_f$ = 0.50 (EtOAc in hexanes = 25%).

NMR Spectroscopy:

^{1}**H NMR** (600 MHz, Chloroform-d, δ) 10.94 (s, 1H), 9.98 (s, 1H), 7.69 – 7.63 (m, 3H), 3.94 (s, 3H).

^{13}**C NMR** (126 MHz, Chloroform-d, δ) 196.44, 165.67, 161.24, 137.30, 133.62, 122.86, 120.40, 119.12, 52.69.

HRMS(m/z) calc'd for $C_9H_8O_44$ $[M+H]^+$, 181.0495; found, 181.0494.

Secondary adamantylmethylamine 32

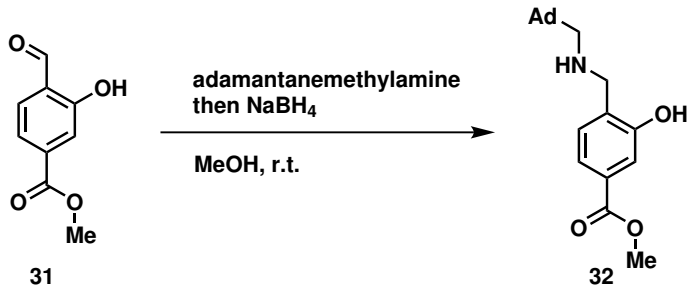

A solution of aldehyde **31** (100 mg, 556 μmol, 1.00 eq) and adamantanemethylamine (96.4 mg, 0.583 mmol, 1.05 eq) in 2 mL methanol was stirred for 30 min at room temperature. Then, 378 mg (10.0 mmol, 18.0 eq) sodium borohydride was added portionwise and the reaction was stirred until no starting material remained, approximately 3h. The mixture was concentrated in vacuo, partitioned between ethyl acetate and water, the aqueous layer extracted two more times with ethyl acetate and the combined organic phases were dried over sodium sulfate. The solvent was removed under reduced pressure and the product was purified by column chromatography. Secondary amine **32** (136 mg, 0.413 mmol, 74.3%) was obtained as a clear oil that solidified upon standing.

$\mathbf{R}_f$ = 0.46 (EtOAc in hexanes = 25%).

NMR Spectroscopy:

^{1}**H NMR** (600 MHz, Chloroform-d, δ) 7.52 – 7.37 (m, 1H), 7.01 (d, J = 7.8 Hz, 0H), 3.98 (s, 1H), 3.86 (s, 1H), 2.30 (s, 1H), 1.99 – 1.93 (m, 2H), 1.70 (d, J = 12.6 Hz, 1H), 1.62 (d, J = 12.3 Hz, 1H), 1.56 – 1.44 (m, 3H).

^{13}C NMR (600 MHz, DMSO-d_6, δ) 9.83 (s, 1H), 7.42 (dt, J = 3.3, 1.9 Hz, 2H), 7.36 (q, J = 1.6 Hz, 1H), 5.16 (s, 1H), 4.51 (s, 2H), 3.81 (dd, J = 2.2, 1.1 Hz, 3H). **HRMS(m/z)** calc'd for $C_{20}H_{27}NO_3$ $[M+H]^+$, 330.2064; found, 330.1910.

Labeling Precursor 29

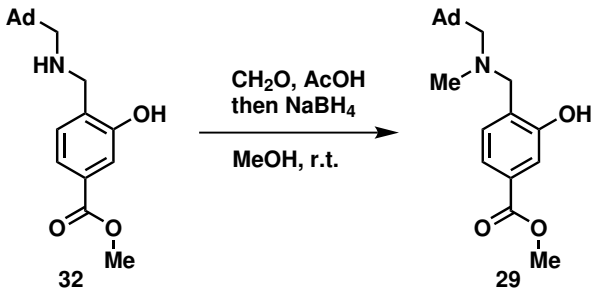

A solution of amine **32** (100 mg, 0.303 mmol, 1.00 eq) in 3 mL methanol, 0.5 mL formalin and a drop of acetic acid were stirred for 2h, then sodium borohydride (22.9 mg, 0.606 mmol, 2.00 eq) were added and the mixture stirred for another hour. The mixture was concentrated in vacuo, partitioned between ethyl acetate and water, the aqueous layer extracted two more times with ethyl acetate and the combined organic phases were dried over sodium sulfate. The solvent was removed under reduced pressure and the product was purified by column chromatography. The labeling precursor **29** (67.7 mg, 0.197 mmol, 65.0%) was obtained as a clear oil that solidified upon standing.

$\mathbf{R}_f$ = 0.64 (EtOAc in hexanes = 25%).

NMR Spectroscopy:

^{1}H NMR (600 MHz, Chloroform-d, δ) 7.46 (s, 1H), 7.43 (dd, J = 7.8, 1.7 Hz, 2H), 6.99 (d, J = 7.8 Hz, 2H), 3.87 (s, 7H), 3.76 (s, 4H), 2.26 (s, 7H), 2.23 (s, 4H), 1.76 – 1.68 (m, 6H), 1.69 – 1.60 (m, 7H), 1.56 (d, J = 3.0 Hz, 12H).

^{13}C NMR (600 MHz, DMSO-d_6, δ) 9.83 (s, 1H), 7.42 (dt, J = 3.3, 1.9 Hz, 2H), 7.36 (q, J = 1.6 Hz, 1H), 5.16 (s, 1H), 4.51 (s, 2H), 3.81 (dd, J = 2.2, 1.1 Hz, 3H).
HRMS(m/z) calc'd for $C_{21}H_{29}NO_3$ $[M+H]^+$, 344.2220; found, 344.2230.

Secondary Adamantylmethylamine 33

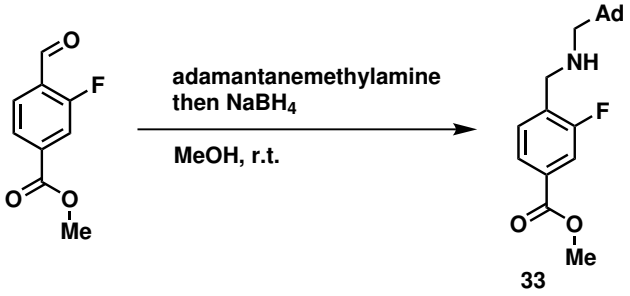

33

A solution of methyl 3-fluoro-4-formylbenzoate (250 mg, 1.37 mmol, 1.00 eq) and adamantanemethylamine (238 mg, 1.44 mmol, 1.05 eq) in 2 mL methanol was stirred for 30 min at room temperature. Then, sodium borohydride (104 mg, 2.74 mmol, 2.00 eq) was added and the reaction was stirred until no starting material remained, approximately 3 h. The mixture was concentrated in vacuo, partitioned between ethyl acetate and water, the aqueous layer extracted two more times with ethyl acetate and the combined organic phases were dried over sodium sulfate. The solvent was removed under reduced pressure and the product was purified by column chromatog-

raphy. The secondary amine **33** (372 mg, 1.12 mmol, 81.8%) was obtained as a clear oil that solidified upon standing.

$\mathbf{R}_f$ = 0.49 (EtOAc in hexanes = 25%).

NMR Spectroscopy:

^{1}**H NMR** (500 MHz, Chloroform-d, δ) 7.79 (dd, J = 7.9, 1.6 Hz, 1H), 7.66 (dd, J = 10.5, 1.6 Hz, 1H), 7.49 (t, J = 7.6 Hz, 1H), 3.90 (s, 3H), 3.88 (s, 2H), 2.22 (s, 2H), 1.94 (d, J = 3.1 Hz, 2H), 1.80 – 1.65 (m, 3H), 1.65 – 1.57 (m, 3H), 1.51 (d, J = 3.0 Hz, 6H).

^{13}**C NMR** (126 MHz, Chloroform-d, δ) 164.49, 160.85 (d, J= 247.4 Hz), 132.34, 131.35, 129.58 (d, J = 13.3 Hz), 122.45, 114.22 (d, J = 24.8 Hz), 70.83, 56.96, 45.36, 40.88, 37.10, 34.97, 28.42.

^{19}**F NMR** (471 MHz, Chloroform-d, δ) -118.66.

HRMS(m/z) calc'd for $C_{20}H_{26}FNO_2$ $[M+H]^+$, 332.2020; found, 332.2068.

Tertiary Adamantanemethylamine 34

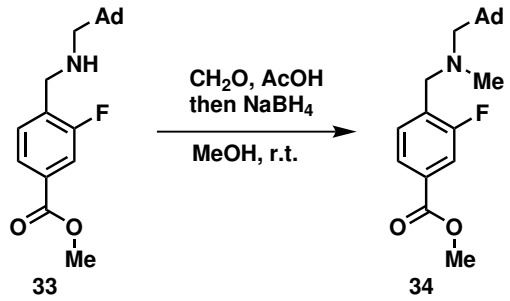

A solution of of amine **33** (350 mg, 1.06 mmol, 1.00 eq) in 3 mL methanol, 0.5 mL

formalin and a drop of acetic acid were stirred for 2h, then sodium borohydride (80.2 mg, 2.12 mmol, 2.00 eq) were added and the mixture stirred for another hour. The mixture was concentrated in vacuo, partitioned between ethyl acetate and water, the aqueous layer extracted two more times with ethyl acetate and the combined organic phases were dried over sodium sulfate. The solvent was removed under reduced pressure and the product was purified by column chromatography. The tertiary amine **34** (227 mg, 0.657 mmol, 62.0%) was obtained as a clear oil that solidified upon standing. $\mathbf{R}_f$ = 0.75 (EtOAc in hexanes = 25%).

NMR Spectroscopy:

^{1}**H NMR** (600 MHz, Chloroform-d, δ) 7.73 (dd, J = 7.9, 1.6 Hz, 1H), 7.64 – 7.44 (m, 2H), 3.83 (s, 3H), 3.56 (s, 2H), 2.16 (s, 3H), 2.06 (s, 2H), 1.90 – 1.80 (m, 3H), 1.63 (dd, J = 12.2, 3.3 Hz, 3H), 1.59 – 1.52 (m, 4H), 1.46 – 1.35 (m, 6H).

^{13}**C NMR** (126 MHz, Chloroform-d, δ) 165.75, 160.66 (d, J = 245.8 Hz), 132.49 (d, J = 14.3 Hz), 130.62, 130.26, 124.94, 116.06 (d, J = 24.0 Hz), 71.00, 57.15, 51.98, 45.52, 40.91, 37.12, 35.06, 28.42.

^{19}**F NMR** (471 MHz, Chloroform-d, δ) -117.42.

HRMS(m/z) calc'd for $C_{21}H_{28}FNO_2$ $[M+H]^+$, 346.2177; found, 346.2158.

Bavarostat (28)

To a solution of ester **34** (200 mg, 0.580 mmol, 1.00 eq) in 2mL 1:1 THF/MeOH at 0 °C was added 0.50 mL hydroxylamine (50% aq, 0.25g, 3.6 mmol, 6.2 eq) and aqueous NaOH (5.0 M, 0.10 mL, 0.50 mmol, 0.86 eq). The reaction mixture was stirred for 2h,

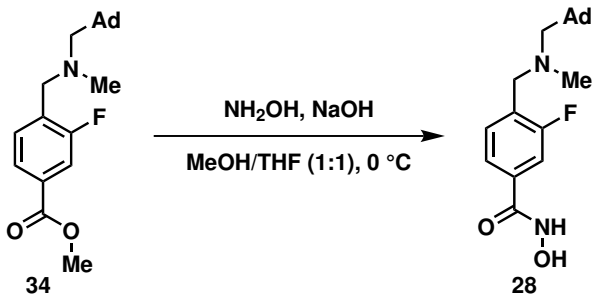

then partitioned between DCM and water. The aqueous layer was extracted another three times with DCM, the combined organic phases were dried over sodium sulfate and concentrated in vacuo. The product was purified by preparative HPLC with a gradient of water and acetonitrile buffered with formic acid. Upon drying in vacuo Bavarostat (123 mg, 0.355 mmol, 61.2 %) was obtained as a light orange, foamy solid.

NMR Spectroscopy:

^{1}**H NMR** (600 MHz, DMSO-d6, δ) 11.21 (s, 1H), 9.11 (s, 1H), 7.59 – 7.50 (m, 2H), 7.47 (dd, J = 10.9, 1.6 Hz, 1H), 3.56 (s, 2H), 2.16 (s, 3H), 2.08 (s, 2H), 1.88 (s, 3H), 1.63 (d, J = 12.3 Hz, 3H), 1.55 (d, J = 12.2 Hz, 3H), 1.43 (s, 6H).

^{13}**C NMR** (126 MHz, Chloroform-d, δ) 164.49, 160.85 (d, J = 247.4 Hz), 132.34, 131.35, 129.63, 122.45, 114.22 (d, J = 24.8 Hz), 70.83, 56.96, 45.36, 40.88, 37.10, 34.97, 28.42.

^{19}**F NMR** (471 MHz, Chloroform-d, δ) -116.71.

HRMS(m/z) calc'd for $C_{20}H_{27}FN_2O_2$ $[M+H]^+$, 347.2129; found: 347.2560.

4.2.2 Biochemistry

IC_{50}

IC_{50} measurements were conducted by BPS Biosciences with an established fluorescence assay.

In vivo protein acetylation levels

Human iPSC-derived neural progenitor cells from a healthy control subject fibroblast cell line GM08330 (Coriell Institute for Medical Research) were generated as described previously [152] and treated with DMSO or a solution of HDAC inhibitor (ACY1215, final concentration 5 μM; Bavarostat, CI-994, Tubastatin A, final concentration 10 μM) for 6 h at 37 °C. Lysis of cell pellets (n=3 per condition) was performed in radioimmunoprecipitation assay (RIPA) buffer (Boston BioProducts #BP-115) with EDTA-free protease inhibitors (Sigma #4693159001). The lysates were centrifuged at 18,000 rpm at 4 °C for 15 min, and the supernatants were collected. The protein concentration was determined by BCA assay (Thermo Scientific #23227). Western blot analysis was conducted on samples adjusted to 6 μg of total protein/replicate. (Figure 4.10)

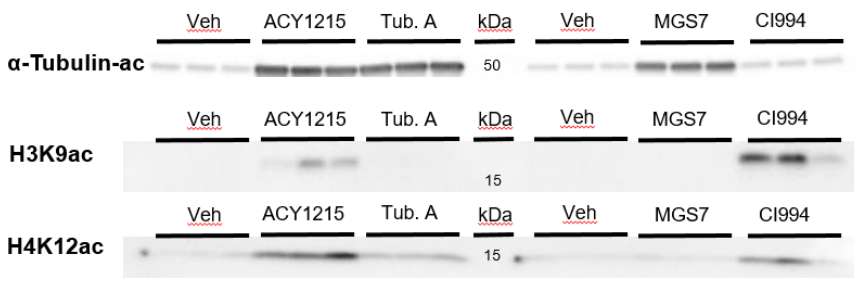

Figure 4.10: Western blots to determine HDAC substrate acetylation levels

4.2.3 Radiochemistry

Radiosynthesis of [^{18}F]Bavarostat

Aqueous [^{18}F]Fluoride obtained from a cyclotron was passed through a SPE Chromafix 30-PS-HCO_3 cartridge that had been previously conditioned with 5.0 mg·mL^{-1} aqueous potassium carbonate and then washed with 18 mL of Millipore Milli-Q water. The captured [^{18}F]fluoride was washed by passing 1 mL of ethanol through the cartridge. At the beginning of the synthesis, 657 mCi were measured on the cartridge. 5 mg of labeling precursor 29, 10 mg of [CpRu(cod)Cl] and 30 mg *N,N*-bis-(2,6-diisopropyl)phenyl-2-chloroimidazolium chloride were heated in 250 µL of ethanol at 85 °C for 30 minutes. The resulting solution was passed through the anion exchange cartridge and collected into a dram vial. The cartridge was flushed with 400 µL acetonitrile and 400 µL DMSO and collected into the same vial, which was subsequently sealed with a Teflon lined cap and heated to 130 °C for 30 minutes. Then, 1mL of THF/MeOH (1:1), 0.4 mL 50% aq. NH_2OH and 0.1 mL 5M NaOH were added at room temperature and the reaction was stirred for 5 minutes. The solution was diluted with water to 10 mL and loaded onto an OASIS MAX SPE cartridge (60 mg), washed with 5 mL of water and eluted with 2 mL ethanol/0.1M AcOH (1:1) and purified by semipreparative HPLC (Agilent Eclipse C-18, 9.4 x 250 mm, 5 µm; flow ramp 0.5 mL·min^{-1} to 5 mL·min^{-1} from 0-4 min, then 5 mL·min^{-1}; 5% ACN in 0.01 N NaOH from 0-4 min, then ramp to 70 % ACN in 0.01 NaOH at 45 min). The isolated fraction was reformulated on an OASIS MAX SPE cartridge (60 mg), washed with 5 mL of water and eluted with 2 mL ethanol/0.1M AcOH (1:1), diluted with 8 mL 0.9 % saline and neutralized with 0.1 N NaOH to pH 5. Overall, 53.3 mCi

were isolated (8.1 % non-decay-corrected radiochemical yield) within 94 min. For analytical data, refer to supporting information.

Semipreparative HPLC for [^{18}F]Bavarostat purification

Agilent Eclipse C-18, 9.4 x 250 mm, 5 μm;

flow ramp 0.5 mL·min^{-1} to 5 mL·min^{-1} from 0-4 min, then 5 mL·min^{-1}, 5% MeCN in 0.01 N NaOH from 0-4 min, then ramp to 70 % MeCN in 0.01 NaOH at 45 min.

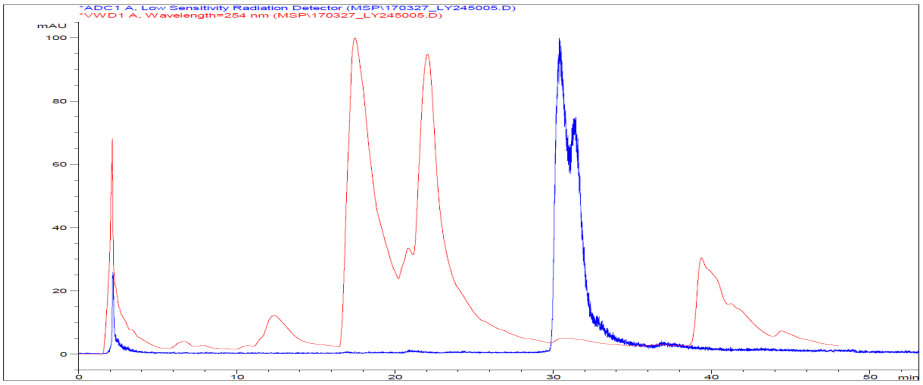

Figure 4.11: Semipreparative HPLC of injected dose UV(254nm) shown in red, low-sensitivity γ-trace shown in blue.

Analytical HPLC of injected [^{18}F]Bavarostat dose

Agilent Eclipse C-18, 4.6 x 10 mm, 5 μm;

flow 2 mL·min^{-1}, gradient from 5% ACN/H_2O, 0.1% TFA at 0 min to 95% MeCN/H_2O, 0.1% TFA at 10 min.

4.2.4 Autoradiography

Sagittal slices of Sprague-Dawley rat brains were sectioned (10 µm) with a cryostat (Thermo Scientific HM550) and mounted onto ColorFrost Plus microscope slides

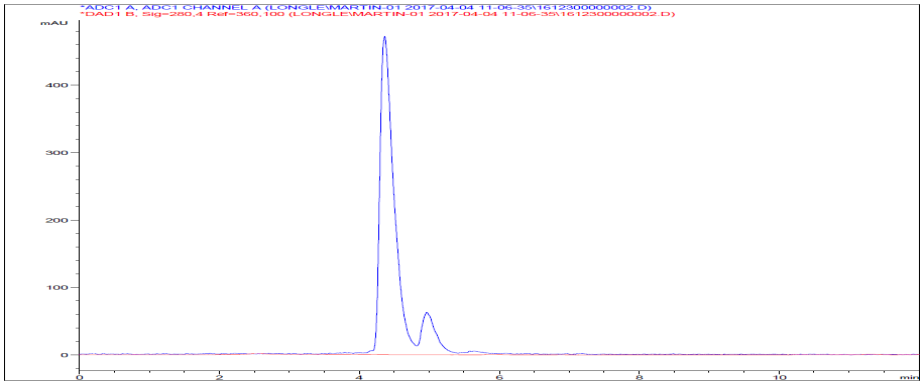

Figure 4.12: Analytical HPLC of injected dose UV(280nm) shown in red, γ-trace shown in blue

(Fisher Scientific 12-550-18) and stored at -20 °C. The slides were submerged in baths of 50 mL of buffer (100 mM Tris, 50 mM NaCl, pH 7.5, 1% BSA) at room temperature and equilibrated for 15 min. The slides were then transferred into baths (50 mL buffer) containing either 50 µL of DMSO or a solution of blocking compound in DMSO (Bavarostat at a final concentration of 100 nM, 1 µM and 10 µM and Tubastatin A at a final concentration of 100 µM). After 15 min, 50 µCi of [^{18}F]Bavarostat were added to each bath. After 15 minutes, all slides were washed by dipping 10 x into buffer and subsequently submerged in 50 mL baths of buffer at 4 °C for 3 minutes. The slides were washed by dipping 10 x into wash buffer (100 mM Tris, 50 mM NaCl, pH 7.5) were dried at 35 °C in a vacuum chamber. A phosphorus screen (Perkin Elmer 7001723) was exposed with the slides for 45 minutes and subsequently imaged with a Cyclone Plus Storage Phosphor (Perkin Elmer) detector. ImageJ was used to apply a Gaussian blur (3.0 radius) smoothing and a lookup table (Royal) with equivalent thresholds for brightness was applied. Raw intensity values from gray and white matter were quantified with the ImageJ measurement tool.

4.2.5 Imaging

Animal Preparation

RODENT 6 male Sprague-Dawley rats (Charles River Laboratories) were used for PET imaging. According to institutional policy, animals were pair-housed until a weight of 500 g, and a 12 h/12 h light/dark cycle was applied. All treatment and imaging experiments were performed in accordance with procedures approved by the Institutional Animal Care and Use Committee at the Massachusetts General Hospital. Anesthesia was achieved with isoflurane in medical oxygen carrier (3% for induction, 2% for maintenance). For intravenous administration, a catheter with an extension line was placed in a lateral tail vein. Each animal received a bolus injection of either vehicle (1:1:8 DMSO/Tween80/saline) or blocking agent in solution (1 $mg{\cdot}kg^{-1}$, 1 $mg{\cdot}mL^{-1}$ in 1:1:8 DMSO/Tween80/saline) immediately prior to injection of the radiotracer.

NHP Two PET/MR studies (baseline/pretreatment) were carried out with one baboon (female, 16 kg, Papio Anubis) as approved by the Institutional Animal Care and Use Committee at the Massachusetts General Hospital. Nil Per Os was instructed 12 h prior to the study. Anesthesia was induced with intramuscular (i.m.) ketamine (10 $mg{\cdot}kg^{-1}$) and xylazine (0.5 $mg{\cdot}kg^{-1}$). Anesthesia was continued during the study with 1-1.5% isoflurane in oxygen carrier and ketamine/xylazine effects were reverted with yobine (0.11 $mg{\cdot}kg^{-1}$, i.m.) prior to the scan. Pretreatment (1 $mg{\cdot}kg^{-1}$ Bavarostat, 5 $mg{\cdot}ml^{-1}$ in 10% DMSO, 10% Tween 80, 80% saline) was administered in one of the scans 5 min prior to radiotracer injection through a catheter in the saphenous vein. Radiotracer injection was performed through the same catheter. Vital signs

(end-tidal CO_2, oxygen saturation, heart rate, and respiration rate) were under continuous surveillance to maintain a normal physiological range, documented every 15 minutes.

PET/CT Image Acquisition

Rodent: After injection of a radiotracer bolus (ca. 700μCi [^{18}F]Bavarostat) a 90 min dynamic PET scan was acquired in pairs for all animals. PET scans were performed on a GammaMedica Triumph PET/CT/SPECT scanner, corrected for attenuation with a µ-map derived from the corresponding CT image, which was acquired immediately following the PET scan. The dynamic PET data was binned into 38 timeframes (8 × 15 s, 8 × 1 min, 10 × 2 min, 12 × 5) and reconstructed individually via an iterative MLEM (maximum likelihood expectation maximization) algorithm in 16 iterations.

textbfNHP: PET/MRI acquisition was performed on a 3T Siemens TIM-Trio with a BrainPET insert (Siemens, Erlangen, Germany). A PET/MRI compatible eight-channel array coil customized for nonhuman primate brain imaging to increase image signal and quality was employed. After administration of the radiotracer (5.2 mCi baseline, 2.9 mCi block), dynamic PET image acquisition was initiated. Dynamic PET data were collected and stored in list mode for 120 min. Image reconstruction was performed using the 3D ordinary Poisson expectation maximization algorithm with detector efficiency, decay, dead time, attenuation, and scatter corrections. PET data were binned in 29 frames (6×10 s, 6×20 s, 2×30 s, 1×1 min, 5×5 min, 9x10 min). Image volumes were eventually reconstructed into 76 slices with 128x128 pixels and a

2.5 mm isotropic voxel size. 30 minutes after scanner start, a high-resolution anatomical scan using multiecho MPRAGE sequence (TR = 2530 ms, TE1/TE2/TE3/TE4 = 1.64/3.5/5.36/7.22 ms, TI = 1200 ms, flip angle = 7°, and 1 mm isotropic) was acquired.

Image Analysis

Rodent: PET images were coregistered to the CT image acquired from the same animal using AMIDE Data sets were cropped and all further image analysis was conducted using PMOD 3.3 (PMOD Technologies, Zurich, Switzerland). For maximum consistency, the data were manually coregistered to the Schiffer Px Rat rat brain template [178] and data was derived from a whole brain VOI (volume of interest) for time activity curves.

NHP: Using the Martinos jip analysis toolkit (www.nitrc.org/projects/jip), MPRAGE data was coregistered to the black baboon atlas [172], and the transformation matrix applied to the dynamic PET data. Using PMOD 3.3, time-activity curves for VOIs were extracted, and time-averaged SUV values were obtained. Kinetic modeling was performed with a metabolite corrected arterial plasma input function in PMOD (Table 4.1).

Table 4.1: SUV and V_T comparison: V_T was derived from a metabolite corrected arterial plasma input function (Feng interpolation) and calculated with a 1-tissue compartment, 2-tissue compartment model or an invasive Logan plot. ACC: anterior cingulate cortex; amyg: amygdala; CB: cerebellum; HC: hippocampus; DLPFC: dorsolateral prefrontal cortex; M1: primary motor area; Nac: nucleus accumbens; OFC: orbitofrontal cortex; PCC: posterior cingulate cortex; pu: putamen; SMA: supplementary motor area; V1: primary visual cortex; WM: white matter; WB: whole brain

Region	**ACC**	**amyg**	**CB**	**DLPFC**	**HC**	**M1**	**NAc**	**OFC**	**PCC**	**pu**	**SMA**	**Th**	**V1**	**caudate**	**WM**
2TCM	68.7	61.4	82.8	72.1	68.3	67.07	50.53	35.51	61.8	94.4	78.5	77.7	73.9	97.6	48.73
%SE	8.28	7.25	7.9	5.46	9.35	8.09	12.14	17.27	8.27	8.06	7.29	7.14	5.72	6.26	14.56
1TCM	65.5	58.76	79.8	69.1	64.5	64.5	48.8	35.48	58.9	94.3	75	75.6	71	93.5	45.8
%SE	11.59	8.26	8.72	9.64	12.86	7.71	10.47	10.05	9.27	7.68	8.43	7.55	7.43	7.65	7.46
Logan$_{inv}$	65.4	62	78.02	68	69.1	63.7	52.3	36.3	59.2	93	74.1	77.1	68.2	91.5	47
%SE	2.39	1.14	0.8	1	2.6	1.29	1.91	1.47	1.65	1.32	1.22	1.62	0.6	1.58	1.7

Bibliography

[1] Bailey, D. L., Townsend, D. W. P. E. V. & Maisey, M. N. *Positron Emission Tomography: Basic Sciences* (Springer-Verlag London, 2005).

[2] Hoh, C. K. Clinical use of FDG PET. *Nuclear Medicine and Biology* **34**, 737 – 742 (2007).

[3] Warburg, O. On the origin of cancer cells. *Science* **123**, 309 – 314 (1956).

[4] Ben-Haim, S. & Ell, P. ^{18}F FDG PET and PET/CT in the evaluation of cancer treatment response. *Journal of Nuclear Medicine* **50**, 88 – 99 (2009).

[5] Newberg, A., Alavi, A. & Reivich, M. Determination of regional cerebral function with FDG-PET imaging in neuropsychiatric disorders. *Seminars in Nuclear Medicine* **32**, 13 – 34 (2002).

[6] Love, C., Tomas, M. B., Tronco, G. G. & Palestro, C. J. FDG PET of infection and inflammation. *RadioGraphics* **25**, 1357 – 1368 (2005).

[7] Lucignani, G., Paganelli, G. & Bombardieri, E. The use of standardized uptake values for assessing FDG uptake with PET in oncology: a clinical perspective. *Nuclear Medicine Communications* **25**, 651 – 656 (2004).

[8] Fowler, J. S. & Ido, T. Initial and subsequent approach for the synthesis of ^{18}FDG. *Seminars in Nuclear Medicine* **32**, 6 – 12 (2002).

[9] Anand, K. & Sabbagh, M. Amyloid imaging: Poised for integration into medical practice. *Neurotherapeutics* **14**, 54 – 61 (2017).

[10] Ametamey, S. M., Honer, M. & Schubiger, P. A. Molecular imaging with PET. *Chemical Reviews* **108**, 1501 – 1516 (2008).

[11] Van de Bittner, G. C., Ricq, E. L. & Hooker, J. M. A philosophy for CNS radiotracer design. *Accounts of Chemical Research* **47**, 3127–3134 (2014).

[12] Campbell, M. G. *et al.* Bridging the gaps in ^{18}F PET tracer development. *Nature Chemistry* **9**, 1 – 3 (2017).

[13] Shen, S. *et al.* Bicyclic-capped histone deacetylase 6 inhibitors with improved activity in a model of axonal Charcot-Marie-Tooth disease. *ACS Chemical Neuroscience* **7**, 240 – 258 (2016).

[14] Goracci, L. *et al.* A rational approach for the identification of non-hydroxamate HDAC6-selective inhibitors. *Scientific reports* 29086 (2016).

[15] Huiban, M. *et al.* A broadly applicable [^{18}F]trifluoromethylation of aryl and heteroaryl iodides for pet imaging. *Nature Chemistry* **5**, 941 – 944 (2013).

[16] Neumann, C. N., Hooker, J. M. & Ritter, T. Concerted nucleophilic aromatic substitution with $^{19}F^-$ and $^{18}F^-$. *Nature* **534**, 369 – 373 (2016).

[17] Bergman, J. & Solin, O. Fluorine-18-labeled fluorine gas for synthesis of tracer molecules. *Nuclear Medicine and Biology* **24**, 677 – 683 (1997).

[18] Teare, H. *et al.* Radiosynthesis and evaluation of [^{18}F]selectfluor bis(triflate). *Angewandte Chemie International Edition* **49**, 6821 – 6824 (2010).

[19] Liu, Z. *et al.* Dual mode fluorescent ^{18}F-pet tracers: Efficient modular synthesis of rhodamine-[cRGD]-2-[^{18}F]-organotrifluoroborate, rapid, and high yielding one-step ^{18}F-labeling at high specific activity, and correlated in vivo PET imaging and ex vivo fluorescence. *Bioconjugate Chemistry* **25**, 1951 – 1962 (2014).

[20] Hoigebazar, L. *et al.* Syntheses of 2-nitroimidazole derivatives conjugated with 1,4,7-triazacyclononane-N,N′-diacetic acid labeled with F-18 using an aluminum complex method for hypoxia imaging. *Journal of Medicinal Chemistry* **55**, 3155 – 3162 (2012).

[21] Hooker, J. M. *et al.* Imaging cardiac SCN5A using the novel F-18 radiotracer radiocaine. *Scientific Reports* **7**, 42136 (2017).

[22] Jackson, A. *et al.* The development of potential new fluorine-18 labelled radiotracers for imaging the GABAA receptor. *Bioorganic and Medicinal Chemistry Letters* **23**, 821 – 826 (2013).

[23] Moon, B. S. *et al.* Facile aromatic radiofluorination of [^{18}F]flumazenil from diaryliodonium salts with evaluation of their stability and selectivity. *Organic and Biomolecular Chemistry* **9**, 8346 – 8355 (2011).

[24] Apana, S. M. *et al.* Synthesis of [^{18}F]anginex with high specific activity [^{18}F]fluorobenzaldehyde for targeting angiogenic activity in solid tumors. *Journal of Labelled Compounds and Radiopharmaceuticals* **54**, 708 – 713 (2011).

[25] Carroll, M. A., Nairne, J., Smith, G. & Widdowson, D. A. Radical scavengers: A practical solution to the reproducibility issue in the fluoridation of diaryliodonium salts. *Journal of Fluorine Chemistry* **128**, 127 – 132 (2007).

[26] Shen, B. *et al.* Effect of aldehyde and methoxy substituents on nucleophilic aromatic substitution by [^{18}F]fluoride. *Journal of Fluorine Chemistry* **128**, 1461 – 1468 (2007).

[27] Li, X. *et al.* Site-specific labeling of annexin v with f-18 for apoptosis imaging. *Bioconjugate Chemistry* **19**, 1684 – 1688 (2008).

[28] Kniess, T., Laube, M., Brust, P. & Steinbach, J. 2-[^{18}F]fluoroethyl tosylate - a versatile tool for building ^{18}F-based radiotracers for positron emission tomography. *Medicinal Chemistry Communications* **6**, 1714 – 1754 (2015).

[29] Schirrmacher, R. *et al.* ^{18}F-labeling of peptides by means of an organosilicon-based fluoride acceptor. *Angewandte Chemie International Edition* **45**, 6047 – 6050 (2006).

[30] Niedermoser, S. *et al.* In vivo evaluation of ^{18}F-SiFAlin modified TATE: A potential challenge for ^{68}Ga-DOTATATE, the clinical gold standard for somatostatin receptor imaging with positron emission tomography (PET). *Journal of Nuclear Medicine* **56**, 1100 – 1105 (2015).

[31] Perrin, D. M. [^{18}F]-organotrifluoroborates as radioprosthetic groups for PET imaging: From design principles to preclinical applications. *Accounts of Chemical Research* **49**, 1333 – 1343 (2016).

[32] Liu, Z. *et al.* Preclinical evaluation of a high-affinity ^{18}F-trifluoroborate octreotate derivative for somatostatin receptor imaging. *Journal of Nuclear Medicine* **55**, 1499 – 1505 (2014).

[33] Ting, R. *et al.* Toward [^{18}F]-labeled aryltrifluoroborate radiotracers: In vivo positron emission tomography imaging of stable aryltrifluoroborate clearance in mice. *Journal of the American Chemical Society* **130**, 12045 – 12055 (2008).

[34] Liu, Z., Li, Y., Ting, R. & Perrin, D. M. Designing kinetically stable aryltrifluoroborates as ^{18}F-capture agents for PET imaging. *Journal of Physical Organic Chemistry* **28**, 210 – 214 (2015).

[35] Ting, R. *et al.* Substituent effects on aryltrifluoroborate solvolysis in water: implications for suzuki-miyaura coupling and the design of stable ^{18}F-labeled aryltrifluoroborates for use in PET imaging. *The Journal of Organic Chemistry* **73**, 4662 – 4670 (2008).

[36] Liu, Z. *et al.* A new ^{18}F-heteroaryltrifluoroborate radio-prosthetic with greatly enhanced stability that is labelled by ^{18}F-^{19}F-isotope exchange in good yield at high specific activity. *Medicinal Chemistry Communications* **5**, 171 – 179 (2014).

[37] Liu, Z. *et al.* Stoichiometric leverage: Rapid ^{18}F-aryltrifluoroborate radiosynthesis at high specific activity for click conjugation. *Angewandte Chemie International Edition* **52**, 2303 – 2307 (2013).

[38] Ting, R., Adam, M. J., Ruth, T. J. & Perrin, D. M. Arylfluoroborates and alkylfluorosilicates as potential PET imaging agents: high-yielding aqueous biomolecular ^{18}F-labeling. *Journal of the American Chemical Society* **127**, 13094 – 13095 (2005).

[39] Li, Z. *et al.* Harvesting ^{18}F-fluoride ions in water via direct ^{18}F-^{19}F isotopic exchange: radiofluorination of zwitterionic aryltrifluoroborates and in vivo stability studies. *Medicinal Chemistry Communications* **3**, 1305 – 1308 (2012).

[40] Liu, Z. *et al.* Rapid, one-step, high yielding ^{18}F-labeling of an aryltrifluoroborate bioconjugate by isotope exchange at very high specific activity. *Journal of Labelled Compounds and Radiopharmaceuticals* **55**, 491 – 496 (2012).

[41] Liu, Z. *et al.* One-step ^{18}F labeling of biomolecules using organotrifluoroborates. *Nature Protocols* **10**, 1423 – 1432 (2015).

[42] Pourghiasian, M. *et al.* ^{18}F-AmBF3-MJ9: A novel radiofluorinated bombesin derivative for prostate cancer imaging. *Bioorganic and Medicinal Chemistry* **23**, 1500 – 1506 (2015).

[43] Liu, Z. *et al.* ^{18}F-trifluoroborate derivatives of [Des-Arg10]Kallidin for imaging bradykinin B1 receptor expression with positron emission tomography. *Molecular Pharmaceutics* **12**, 974 – 982 (2015).

[44] Chansaenpak, K. *et al.* [^{18}F]-NHC-BF_3 adducts as water stable radio-prosthetic groups for PET imaging. *Chemical Communications* **51**, 12439 – 12442 (2015).

[45] McBride, W. J. *et al.* Improved ^{18}F labeling of peptides with a fluoride-aluminum-chelate complex. *Bioconjugate Chemistry* **21**, 1331 – 1340 (2010).

[46] McBride, W. J., Sharkey, R. M. & Goldenberg, D. M. Radiofluorination using aluminum-fluoride (Al^{18}F). *EJNMMI Research* **3**, 36 (2013).

[47] Liu, Q. *et al.* Development of a novel PET tracer [^{18}F]AlF-NOTA-C6 targeting MMP2 for tumor imaging. *PLOS ONE* **10**, 1 – 15 (2015).

[48] Huang, S. *et al.* A novel [f-18] aluminum-fluoride labeled PSMA tracer with minimal background uptake. *Journal of Nuclear Medicine* **55**, 499 (2014).

[49] Chen, K., Ma, W., Huang, R. & Conti, P. Combining aluminum [^{18}F]fluoride radiolabeling and catalyst-free click chemistry to rapidly prepare ^{18}F-labeled PET probes. *Journal of Nuclear Medicine* **56**, 219 (2015).

[50] McBride, W. J. *et al.* A novel method of ^{18}F radiolabeling for PET. *Journal of Nuclear Medicine* **50**, 991 – 998 (2009).

[51] Tredwell, M. & Gouverneur, V. ^{18}F labeling of arenes. *Angewandte Chemie International Edition* **51**, 11426 – 11437 (2012).

[52] Preshlock, S., Tredwell, M. & Gouverneur, V. ^{18}F-labeling of arenes and heteroarenes for applications in positron emission tomography. *Chemical Reviews* **116**, 719 – 766 (2016).

[53] Horn, E., Fairway, S., Mantzilas, D. & Powell, N. Purification method (2012). EP Patent App. EP20,100,766,453.

[54] Kilbourn, M. R. *et al.* Carrier-added and no-carrier-added syntheses of [^{18}F]spiroperidol and [^{18}F]haloperidol. *The International Journal of Applied Radiation and Isotopes* **35**, 591 – 598 (1984).

[55] Lee, E. *et al.* A fluoride-derived electrophilic late-stage fluorination reagent for PET imaging. *Science* **334**, 639 – 642 (2011).

[56] Brandt, J. R., Lee, E., Boursalian, G. B. & Ritter, T. Mechanism of electrophilic fluorination with Pd(IV): fluoride capture and subsequent oxidative fluoride transfer. *Chemical Science* **5**, 169 – 179 (2014).

[57] Kamlet, A. S. *et al.* Application of palladium-mediated ^{18}F-fluorination to PET radiotracer development: Overcoming hurdles to translation. *PLOS ONE* **8**, 1 – 10 (2013).

[58] Lee, E., Hooker, J. M. & Ritter, T. Nickel-mediated oxidative fluorination for PET with aqueous [^{18}F] fluoride. *Journal of the American Chemical Society* **134**, 17456 – 17458 (2012).

[59] Ren, H. *et al.* Synthesis and imaging validation of [^{18}F]MDL100907 enabled by Ni-mediated fluorination. *ACS Chemical Neuroscience* **5**, 611 – 615 (2014).

[60] Hoover, A. J. *et al.* A transmetalation reaction enables the synthesis of [^{18}F]5-fluorouracil from [^{18}F]fluoride for human PET imaging. *Organometallics* **35**, 1008 – 1014 (2016).

[61] Tredwell, M. *et al.* A general copper-mediated nucleophilic ^{18}F fluorination of arenes. *Angewandte Chemie International Edition* **53**, 7751 – 7755 (2014).

[62] Preshlock, S. *et al.* Enhanced copper-mediated ^{18}F-fluorination of aryl boronic esters provides eight radiotracers for PET applications. *Chemical Communications* **52**, 8361 – 8364 (2016).

[63] Sergeev, M. E., Morgia, F., Lazari, M., Wang, C. & van Dam, R. M. Titania-catalyzed radiofluorination of tosylated precursors in highly aqueous medium. *Journal of the American Chemical Society* **137**, 5686 – 5694 (2015).

[64] Mossine, A. V. *et al.* Synthesis of [^{18}F]arenes via the copper-mediated [^{18}F]fluorination of boronic acids. *Organic Letters* **17**, 5780 – 5783 (2015).

[65] Stephenson, N. A. *et al.* Iodonium ylide-mediated radiofluorination of ^{18}F-FPEB and validation for human use. *Journal of Nuclear Medicine* **56**, 489 – 492 (2015).

[66] Rotstein, B. H. *et al.* Mechanistic studies and radiofluorination of structurally diverse pharmaceuticals with spirocyclic iodonium(III) ylides. *Chemical Science* **7**, 4407 – 4417 (2016).

[67] Jaenisch, R. & Bird, A. Epigenetic regulation of gene expression: how the genome integrates intrinsic and environmental signals. *Nature Genetics* **33**, 245 – 254 (2005).

[68] Holliday, R. & Pugh, J. DNA modification mechanisms and gene activity during development. *Science* **187**, 226 – 232 (1975).

[69] Riggs, A. D. inactivation, differentiation, and DNA methylation. *Cytogenetics and Cell Genetics* **14**, 9 – 25 (1975).

[70] Wirén, M. *et al.* Genome wide analysis of nucleosome density histone acetylation and HDAC function in fission yeast. *The EMBO Journal* **24**, 2906 – 2918 (2005).

[71] Roth, S. Y., Denu, J. M. & Allis, C. D. Histone acetyltransferases. *Annual review of biochemistry* **70**, 81 – 120 (2001).

[72] Taunton, J., Hassig, C. A. & Schreiber, S. L. A mammalian histone deacetylase related to the yeast transcriptional regulator Rpd3p. *Science* **272**, 408 – 411 (1996).

[73] Brownell, J. E. & Allis, C. D. An activity gel assay detects a single, catalytically active histone acetyltransferase subunit in tetrahymena macronuclei. *Proceedings of the National Academy of Sciences* **92**, 6364 – 6368 (1995).

[74] Zhao, S. *et al.* Regulation of cellular metabolism by protein lysine acetylation. *Science* **327**, 1000 – 1004 (2010).

[75] Choudhary, C. *et al.* Lysine acetylation targets protein complexes and co-regulates major cellular functions. *Science* **325**, 834 – 840 (2009).

[76] Kouzarides, T. Acetylation: a regulatory modification to rival phosphorylation? *The EMBO Journal* **19**, 1176 – 1179 (2000).

[77] Mottamal, M., Zheng, S., Huang, T. & Wang, G. Histone deacetylase inhibitors in clinical studies as templates for new anticancer agents. *Molecules* **20**, 3898 – 3941 (2015).

[78] Dokmanovic, M., Clarke, C. & Marks, P. A. Histone deacetylase inhibitors: Overview and perspectives. *Molecular Cancer Research* **5**, 981 – 989 (2007).

[79] Ruijter, A. J. d., Gennip, A. H. v., Caron, H. N., Kemp, S. & Kuilenburg, A. B. v. Histone deacetylases (HDACs): characterization of the classical HDAC family. *Biochemical Journal* **370**, 737 – 749 (2003).

[80] d'Ydewalle, C., Bogaert, E. & Van Den Bosch, L. HDAC6 at the intersection of neuroprotection and neurodegeneration. *Traffic* **13**, 771 – 779 (2012).

[81] Halili, M. A., Andrews, M. R., Sweet, M. J. & Fairlie, D. P. Histone deacetylase inhibitors in inflammatory disease. *Current Topics in Medicinal Chemistry* **9**, 309 – 319 (2009).

[82] Grayson, D. R., Kundakovic, M. & Sharma, R. P. Is there a future for histone deacetylase inhibitors in the pharmacotherapy of psychiatric disorders? *Molecular Pharmacology* **77**, 126 – 135 (2010).

[83] Abel, T. & Zukin, R. S. Epigenetic targets of HDAC inhibition in neurodegenerative and psychiatric disorders. *Current Opinion in Pharmacology* **8**, 57 – 64 (2008).

[84] Graff, J. *et al.* An epigenetic blockade of cognitive functions in the neurodegenerating brain. *Nature* **483**, 222 – 226 (2012).

[85] Covington, H. E. *et al.* Antidepressant actions of histone deacetylase inhibitors. *Journal of Neuroscience* **29**, 11451 – 11460 (2009).

[86] Sharma, R. P., Grayson, D. R. & Gavin, D. P. Histone deactylase 1 expression is increased in the prefrontal cortex of schizophrenia subjects: Analysis of the national brain databank microarray collection. *Schizophrenia Research* **98**, 111 – 117 (2008).

[87] Benes, F. M. *et al.* Regulation of the GABA cell phenotype in hippocampus of schizophrenics and bipolars. *Proceedings of the National Academy of Sciences* **104**, 10164 – 10169 (2007).

[88] Guan, J.-S. *et al.* HDAC2 negatively regulates memory formation and synaptic plasticity. *Nature* **459**, 55 – 60 (2009).

[89] Sugars, K. L. & Rubinsztein, D. C. Transcriptional abnormalities in huntington disease. *Trends in Genetics* **19**, 233 – 238 (2003).

[90] Okazawa, H. Polyglutamine diseases: a transcription disorder? *Cellular and Molecular Life Sciences CMLS* **60**, 1427 – 1439 (2003).

[91] Schroeder, F. A. *et al.* Expression of HDAC2 but not HDAC1 transcript is reduced in dorsolateral prefrontal cortex of patients with schizophrenia. *ACS Chemical Neuroscience* **8**, 662 – 668 (2017).

[92] Hayakawa, T. & Nakayama, J.-i. Physiological roles of class I HDAC complex and histone demethylase. *Journal of Biomedicine and Biotechnology* **2011**, 129383 (2011).

[93] Zhang, Y. *et al.* Analysis of the NuRD subunits reveals a histone deacetylase core complex and a connection with dna methylation. *Genes & Development* **13**, 1924 – 1935 (1999).

[94] Zhang, Y., LeRoy, G., Seelig, H.-P., Lane, W. S. & Reinberg, D. The dermatomyositis-specific autoantigen Mi2 is a component of a complex containing histone deacetylase and nucleosome remodeling activities. *Cell* **95**, 279 – 289 (1998).

[95] Andrés, M. E. *et al.* CoREST: A functional corepressor required for regulation of neural-specific gene expression. *Proceedings of the National Academy of Sciences* **96**, 9873 – 9878 (1999).

[96] Horlein, A. J. *et al.* Ligand-independent repression by the thyroid hormone receptor mediated by a nuclear receptor co-repressor. *Nature* **377**, 397 – 404 (1995).

[97] Wang, J., Hoshino, T., Redner, R. L., Kajigaya, S. & Liu, J. M. Eto, fusion partner in t(8 21) acute myeloid leukemia, represses transcription by interaction with the human N-CoR/mSin3/HDAC1 complex. *Proceedings of the National Academy of Sciences* **95**, 10860 – 10865 (1998).

[98] Bantscheff, M. *et al.* Chemoproteomics profiling of hdac inhibitors reveals selective targeting of hdac complexes. *Nature Biotechnology* **29**, 255 – 265 (2011).

[99] Becher, I. *et al.* Chemoproteomics reveals time-dependent binding of histone deacetylase inhibitors to endogenous repressor complexes. *ACS Chemical Biology* **9**, 1736 – 1746 (2014).

[100] Li, L. & Yang, X.-J. Tubulin acetylation: responsible enzymes, biological functions and human diseases. *Cellular and Molecular Life Science* **72**, 4237 – 4255 (2015).

[101] Santo, L. *et al.* Preclinical activity, pharmacodynamic, and pharmacokinetic properties of a selective HDAC6 inhibitor, ACY-1215, in combination with bortezomib in multiple myeloma. *Blood* **119**, 2579 – 2589 (2012).

[102] Malvaez, M. *et al.* HDAC3-selective inhibitor enhances extinction of cocaine-seeking behavior in a persistent manner. *Proceedings of the National Academy of Sciences* **110**, 2647 – 2652 (2013).

[103] Suzuki, T. *et al.* Identification of highly selective and potent histone deacetylase 3 inhibitors using click chemistry-based combinatorial fragment assembly. *PLOS ONE* **8**, 1 – 12 (2013).

[104] Choi, C.-J. *et al.* Discovery of a novel HDAC3 selective inhibitor and its evaluation in lymphoma model. *Bulletin of the Korean Chemical Society* **37**, 42 – 47 (2016).

[105] KrennHrubec, K., Marshall, B. L., Hedglin, M., Verdin, E. & Ulrich, S. M. Design and evaluation of 'linkerless' hydroxamic acids as selective HDAC8 inhibitors. *Bioorganic & Medicinal Chemistry Letters* **17**, 2874 – 2878 (2007).

[106] Song, S. *et al.* The inhibition of histone deacetylase 8 suppresses proliferation and inhibits apoptosis in gastric adenocarcinoma. *International Journal of Oncology* **47**, 1819 – 1828 (2015).

[107] Butler, K. V. *et al.* Rational design and simple chemistry yield a superior, neuroprotective HDAC6 inhibitor, tubastatin a. *Journal of the American Chemical Society* **132**, 10842 – 10846 (2010).

[108] Xu, X., Kozikowski, A. & Pozzo-Miller, L. A selective histone deacetylase-6 inhibitor improves BDNF trafficking in hippocampal neurons from MeCP2 knockout mice: implications for Rett syndrome. *Frontiers in Cellular Neuroscience* **8**, 68 (2014).

[109] Haggarty, S. J., Koeller, K. M., Wong, J. C., Grozinger, C. M. & Schreiber, S. L. Domain-selective small-molecule inhibitor of histone deacetylase 6 (HDAC6)-mediated tubulin deacetylation. *Proceedings of the National Academy of Sciences* **100**, 4389 – 4394 (2003).

[110] Wagner, F. F. *et al.* Potent and selective inhibition of histone deacetylase 6 (HDAC6) does not require a surface-binding motif. *Journal of Medicinal Chemistry* **56**, 1772 – 1776 (2013).

[111] Hai, Y. & Christianson, D. W. Histone deacetylase 6 structure and molecular basis of catalysis and inhibition. *Nature chemical Biology* **12**, 741 – 747 (2016).

[112] Miyake, Y. *et al.* Structural insights into HDAC6 tubulin deacetylation and its selective inhibition. *Nature Chemical Biology* **12**, 748 – 754 (2016).

[113] Su, M. *et al.* HDAC6 regulates aggresome-autophagy degradation pathway of α-synuclein in response to MPP^+-induced stress. *Journal of Neurochemistry* **117**, 112 – 120 (2011).

[114] Ouyang, H. *et al.* Protein aggregates are recruited to aggresome by histone deacetylase 6 via unanchored ubiquitin C termini. *Journal of Biological Chemistry* **287**, 2317 – 2327 (2012).

[115] Kawaguchi, Y. *et al.* The deacetylase HDAC6 regulates aggresome formation and cell viability in response to misfolded protein stress. *Cell* **115**, 727 – 738 (2003).

[116] Miki, Y. *et al.* Accumulation of histone deacetylase 6, an aggresome-related protein, is specific to Lewy bodies and glial cytoplasmic inclusions. *Neuropathology* **31**, 561 – 568 (2011).

[117] Kwon, S., Zhang, Y. & Matthias, P. The deacetylase HDAC6 is a novel critical component of stress granules involved in the stress response. *Genes & Development* **21**, 3381 – 3394 (2007).

[118] Aoyagi, S. & Archer, T. K. Modulating molecular chaperone Hsp90 functions through reversible acetylation. *Trends in Cell Biology* **15**, 565 – 567 (2005).

[119] Scroggins, B. T. *et al.* An acetylation site in the middle domain of Hsp90 regulates chaperone function. *Molecular Cell* **25**, 151 – 159 (2007).

[120] Bali, P. *et al.* Inhibition of histone deacetylase 6 acetylates and disrupts the chaperone function of heat shock protein 90: A novel basis for antileukemia activity of histone deacetylase inhibitors. *Journal of Biological Chemistry* **280**, 26729 – 26734 (2005).

[121] Li, S., Liu, X., Chen, X., Zhang, L. & Wang, X. Histone deacetylase 6 promotes growth of glioblastoma through inhibition of SMAD2 signaling. *Tumor Biology* **36**, 9661 – 9665 (2015).

[122] Wang, Z. *et al.* HDAC6 promotes cell proliferation and confers resistance to temozolomide in glioblastoma. *Cancer Letters* **379**, 134 – 142 (2016).

[123] Lucio-Eterovic, A. K. *et al.* Differential expression of 12 histone deacetylase (HDAC) genes in astrocytomas and normal brain tissue: class II and IV are hypoexpressed in glioblastomas. *BMC Cancer* **8**, 243 (2008).

[124] Delépine, C. *et al.* Altered microtubule dynamics and vesicular transport in mouse and human MeCP2-deficient astrocytes. *Human Molecular Genetics* **25**, 146 (2016).

[125] Gold, W. A., Lacina, T. A., Cantrill, L. C. & Christodoulou, J. MeCP2 deficiency is associated with reduced levels of tubulin acetylation and can be restored using HDAC6 inhibitors. *Journal of Molecular Medicine* **93**, 63 – 72 (2015).

[126] Anderson, K. W. *et al.* Quantification of histone deacetylase isoforms in human frontal cortex, human retina, and mouse brain. *PLOS ONE* **10**, 1 – 16 (2015).

[127] Cuadrado-Tejedor, M. *et al.* A first-in-class small-molecule that acts as a dual inhibitor of hdac and pde5 and that rescues hippocampal synaptic impairment in Alzheimer′s disease mice. *Neuropsychopharmacology* **42**, 524 – 539 (2017).

[128] Du, Y. *et al.* Histone deacetylase 6 regulates cytotoxic α-synuclein accumulation through induction of the heat shock response. *Neurobiology of Aging* **35**, 2316 – 2328 (2014).

[129] Fukada, M. *et al.* Loss of deacetylation activity of HDAC6 affects emotional behavior in mice. *PLOS ONE* **7**, 1 – 8 (2012).

[130] Espallergues, J. *et al.* HDAC6 regulates glucocorticoid receptor signaling in serotonin pathways with critical impact on stress resilience. *Journal of Neuroscience* **32**, 4400 – 4416 (2012).

[131] Jochems, J. *et al.* Antidepressant-like properties of novel HDAC6-selective inhibitors with improved brain bioavailability. *Neuropsychopharmacology* **39**, 389 – 400 (2014).

[132] Jochems, J. *et al.* Enhancement of stress resilience through histone deacetylase 6–mediated regulation of glucocorticoid receptor chaperone dynamics. *Biological Psychiatry* **77**, 345 – 355 (2015).

[133] Martin, V. *et al.* Effect of agomelatine on memory deficits and hippocampal gene expression induced by chronic social defeat stress in mice. *Scientific Reports* **7**, 45907 (2017).

[134] Jianhua, F., Wei, W., Xiaomei, L. & Shao-Hui, W. Chronic social defeat stress leads to changes of behaviour and memory-associated proteins of young mice. *Behavioural Brain Research* **316**, 136 – 144 (2017).

[135] Hobara, T. *et al.* Altered gene expression of histone deacetylases in mood disorder patients. *Journal of Psychiatric Research* **44**, 263 – 270 (2010).

[136] Fukada, M., Nakayama, A., Mamiya, T., Yao, T.-P. & Kawaguchi, Y. Dopaminergic abnormalities in HDAC6-deficient mice. *Neuropharmacology* **110, Part A**, 470 – 479 (2016).

[137] Bonomi, R. *et al.* Novel histone deacetylase class IIa selective substrate radiotracers for PET imaging of epigenetic regulation in the brain. *PLOS ONE* **10**, 1 – 19 (2015).

[138] Jones, P. *et al.* Probing the elusive catalytic activity of vertebrate class IIa histone deacetylases. *Bioorganic & Medicinal Chemistry Letters* **18**, 1814 – 1819 (2008).

[139] Mukhopadhyay, U., Tong, W. P., Gelovani, J. G. & Alauddin, M. M. Radiosynthesis of 6-([^{18}F]fluoroacetamido)-1-hexanoicanilide ([^{18}F]FAHA) for PET imaging of histone deacetylase (HDAC). *Journal of Labelled Compounds and Radiopharmaceuticals* **49**, 997 – 1006 (2006).

[140] Nishii, R. *et al.* PET imaging of histone deacetylase activity in a rat brain using 6-([^{18}F]-fluoroacetamide)-1-hexanoicanilide ([^{18}F]-faha). *Journal of Nuclear Medicine Meeting Abstracts* **48**, 336P–a (2007).

[141] Sanabria, S. M. *et al.* Quantification of HDAC inhibition by F-SAHA in rhesus monkey brain using the PET tracer [^{18}F]FAHA. *NeuroImage* **41, Supplement 2**, T15 (2008). Neuroreceptor Mapping 2008, The Seventh International Symposium on Functional Neuroreceptor Mapping of Living Brain.

[142] Yeh, H.-H. *et al.* Imaging epigenetic regulation by histone deacetylases in the brain using PET/MRI with ^{18}F-FAHA. *NeuroImage* **64**, 630 – 639 (2013).

[143] Tang, W. *et al.* ^{18}F-FAHA PET for imaging histone deacetylase in lung cancer. *Journal of Nuclear Medicine* **52**, 411 (2011).

[144] Reid, A. E. *et al.* Evaluation of 6-([^{18}F]fluoroacetamido)-1-hexanoicanilide for PET imaging of histone deacetylase in the baboon brain. *Nuclear Medicine and Biology* **36**, 247 – 258 (2009).

[145] Seo, Y. J. *et al.* Radionuclide labeling and evaluation of candidate radioligands for PET imaging of histone deacetylase in the brain. *Bioorganic & Medicinal Chemistry Letters* **23**, 6700 – 6705 (2013).

[146] Seo, Y. J. *et al.* Image-guided synthesis reveals potent blood-brain barrier permeable histone deacetylase inhibitors. *ACS Chemical Neuroscience* **5**, 588 – 596 (2014).

[147] Kim, S. W. *et al.* Whole-body pharmacokinetics of HDAC inhibitor drugs, butyric acid, valproic acid and 4-phenylbutyric acid measured with carbon-11 labeled analogs by PET. *Nuclear Medicine and Biology* **40**, 912 – 918 (2013).

[148] Hooker, J. M. *et al.* Histone deacetylase inhibitor MS-275 exhibits poor brain penetration: Pharmacokinetic studies of [^{11}C]MS-275 using positron emission tomography. *ACS Chemical Neuroscience* **1**, 65 – 73 (2010).

[149] Wang, C. *et al.* Design, synthesis, and evaluation of hydroxamic acid-based molecular probes for in vivo imaging of histone deacetylase (HDAC) in brain. *American Journal of Nuclear Medicine and Molecular Imaging* **4**, 29 – 38 (2013).

[150] Wang, C. *et al.* In vivo imaging of histone deacetylases (HDACs) in the central nervous system and major peripheral organs. *Journal of Medicinal Chemistry* **57**, 7999 – 8009 (2014).

[151] Wey, H.-Y. *et al.* Kinetic analysis and quantification of [^{11}C]martinostat for in vivo hdac imaging of the brain. *ACS Chemical Neuroscience* **6**, 708 – 715 (2015).

[152] Wey, H.-Y. *et al.* Insights into neuroepigenetics through human histone deacetylase PET imaging. *Science Translational Medicine* **8**, 351ra106 (2016).

[153] Fujimoto, T., Becker, F. & Ritter, T. Phenofluor: Practical synthesis, new formulation, and deoxyfluorination of heteroaromatics. *Organic Process Research & Development* **18**, 1041 – 1044 (2014).

[154] Tang, P., Wang, W. & Ritter, T. Deoxyfluorination of phenols. *Journal of the American Chemical Society* **133**, 11482 – 11484 (2011).

[155] Fujimoto, T. & Ritter, T. Phenofluormix: Practical chemoselective deoxyfluorination of phenols. *Organic Letters* **17**, 544 – 547 (2015).

[156] Kane-Maguire, L. A. P., Honig, E. D. & Sweigart, D. A. Nucleophilic addition to coordinated cyclic π-hydrocarbons: mechanistic and synthetic studies. *Chemical Reviews* **84**, 525 – 543 (1984).

[157] Rose-Munch, F., Gagliardini, V., Renard, C. & Rose, E. (η^6-arene)tricarbonylchromium and (η^5-cyclohexadienyl) tricarbonylmanganese complexes: indirect nucleophilic substitutions. *Coordination Chemistry Reviews* **178–180, Part 1**, 249 – 268 (1998).

[158] Pike, R. D. & Sweigart, D. A. Electrophilic reactivity of coordinated cyclic π-hydrocarbons. *Coordination Chemistry Reviews* **187**, 183 – 222 (1999).

[159] Pape, A. R., Kaliappan, K. P. & Kündig, E. P. Transition-metal-mediated dearomatization reactions. *Chemical Reviews* **100**, 2917 – 2940 (2000).

[160] Semmelhack, M. F. & Chlenov, A. *(Arene)Cr(CO)3 Complexes: Aromatic Nucleophilic Substitution*, 43 – 69 (Springer Berlin Heidelberg, Berlin, Heidelberg, 2004).

[161] Walton, J. W. & Williams, J. M. J. Catalytic S_NAr of unactivated aryl chlorides. *Chemical Communications* **51**, 2786 – 2789 (2015).

[162] Konovalov, A., Gorbacheva, E., Miloserdov, F. & Grushin, V. Ruthenium-catalyzed nucleophilic fluorination of halobenzenes. *Chemical Communications* **51**, 13527 – 13530 (2015).

[163] Muetterties, E. L., Bleeke, J. R., Wucherer, E. J. & Albright, T. Structural, stereochemical, and electronic features of arene-metal complexes. *Chemical Reviews* **82**, 499 – 525 (1982).

[164] Semmelhack, M. F., Chlenov, A. & Ho, D. M. Accelerated arene ligand exchange in the (arene)$cr(co)_2$L series. *Journal of the American Chemical Society* **127**, 7759 – 7773 (2005).

[165] Otsuka, M., Yokoyama, K., H.and Endo & Shibata, T. Facile catalytic S_NAr reaction of nonactivated fluoroarenes with amines using η^6-benzene ruthenium(II) complex. *Synlett* **2010**, 2601 – 2606 (2010).

[166] Okazaki, M., Yamahira, N., Minglana, J. J. G. & Tobita, H. Ru(xantsil)(CO)(PCy_3): Facile generation of a coordinatively unsaturated ruthenium(II) complex bearing 14 valence electrons [xantsil = (9,9-dimethylxanthene-4,5-diyl)bis(dimethylsilyl)]. *Organometallics* **23**, 4531 – 4533 (2004).

[167] Molinspiration Property Calculation Services, www.molinspiration.com, 2002.

[168] Tetko, I. V. *et al.* Virtual computational chemistry laboratory - design and description. *Journal of Computer-Aided Molecular Design* **19**, 453 – 463 (2005).

[169] VCCLAB, Virtual Computational Chemistry Laboratory, www.vcclab.org, 2005.

[170] Liu, J., Obando, D., Liao, V., Lifa, T. & Codd, R. The many faces of the adamantyl group in drug design. *European Journal of Medicinal Chemistry* **46**, 1949 – 1963 (2011).

[171] Bordwell, F. G. Equilibrium acidities in dimethyl sulfoxide solution. *Accounts of Chemical Research* **21**, 456 – 463 (1988).

[172] Black, K. J., Snyder, A. Z., Koller, J. M., Gado, M. H. & Perlmutter, J. S. Template images for nonhuman primate neuroimaging: 1. baboon. *NeuroImage* **14**, 736 – 743 (2001).

[173] Song, M., Wu, S., Lu, P.-b., Qiao, Y.-n. & Hang, T.-j. A selective and sensitive pre-column derivatization HPLC method for the trace analysis of genotoxic impurity hydroxylamine in active pharmaceutical ingredients. *Analytical Methods* **8**, 8352–8361 (2016).

[174] Huang, J. Tracking drugs. *New England Journal of Medicine* **369**, 1168 – 1169 (2013).

[175] Aebersold, R. & Mann, M. Mass spectrometry-based proteomics. *Nature* **422**, 198 – 207 (2003).

[176] Oda, Y., Huang, K., Cross, F. R., Cowburn, D. & Chait, B. T. Accurate quantitation of protein expression and site-specific phosphorylation. *Proceedings of the National Academy of Sciences* **96**, 6591–6596 (1999).

[177] Werner, T. *et al.* Ion coalescence of neutron encoded TMT 10-plex reporter ions. *Analytical Chemistry* **86**, 3594 – 3601 (2014).

[178] Schiffer, W. K. *et al.* Serial microPET measures of the metabolic reaction to a microdialysis probe implant. *Journal of Neuroscience Methods* **155**, 272 – 284 (2006).

[179] Wager, T. T., Hou, X., Verhoest, P. R. & Villalobos, A. Moving beyond rules: The development of a central nervous system multiparameter optimization (CNS MPO) approach to enable alignment of druglike properties. *ACS Chemical Neuroscience* **1**, 435–449 (2010).

[180] Estiu, G. *et al.* Structural origin of selectivity in class II-selective histone deacetylase inhibitors. *Journal of Medicinal Chemistry* **51**, 2898–2906 (2008).

[181] Schäfer, S. *et al.* Pyridylalanine-containing hydroxamic acids as selective hdac6 inhibitors. *ChemMedChem* **4**, 283 – 290 (2009).

[182] Strebl, M. G. *et al.* Development of a fluorinated class-i HDAC radiotracer reveals key chemical determinants of brain penetrance. *ACS Chemical Neuroscience* **7**, 528 – 533 (2016).

[183] Spange, S., Wagner, T., Heinzel, T. & Krämer, O. H. Acetylation of non-histone proteins modulates cellular signalling at multiple levels. *The International Journal of Biochemistry & Cell Biology* **41**, 185 – 198 (2009).

[184] Valenzuela-Fernández, A., Cabrero, J. R., Serrador, J. M. & Sánchez-Madrid, F. HDAC6: a key regulator of cytoskeleton, cell migration and cell-cell interactions. *Trends in Cell Biology* **18**, 291 – 297 (2008).